# From Q-space to R-space: Introduction to PDF-analysis

***Henry E. Fischer***

Institut Laue-Langevin, Grenoble

DIF group Cookies & Science seminar, ILL,
15h00 Tuesday 4 and Thursday 6 October 2016

# Diffraction Basics

# Schematic of a diffraction measurement (mono-λ)

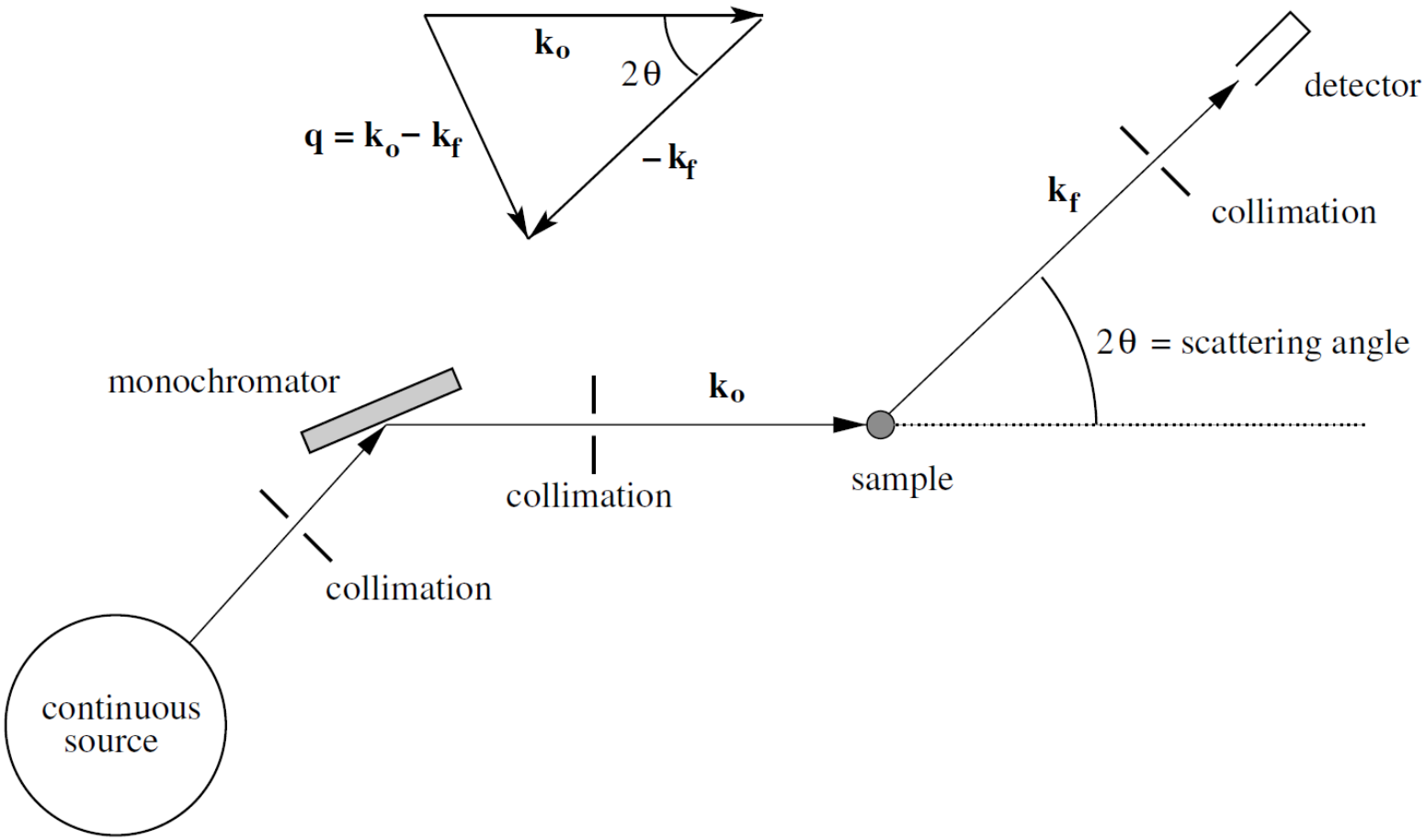


Quanta (*e.g.* x-rays or neutrons) of incident wavevector $\mathbf{k}_o$ and incident energy $E_o$ are scattered by a sample through a scattering angle $2\theta$ thus losing kinetic energy $\hbar\omega = E_o - E_f$ and momentum $\hbar\mathbf{q}$ where $\mathbf{q} = \mathbf{k}_o - \mathbf{k}_f$ is the wavevector transfer or scattering vector.

# Schematic of a diffraction measurement (mono-λ)

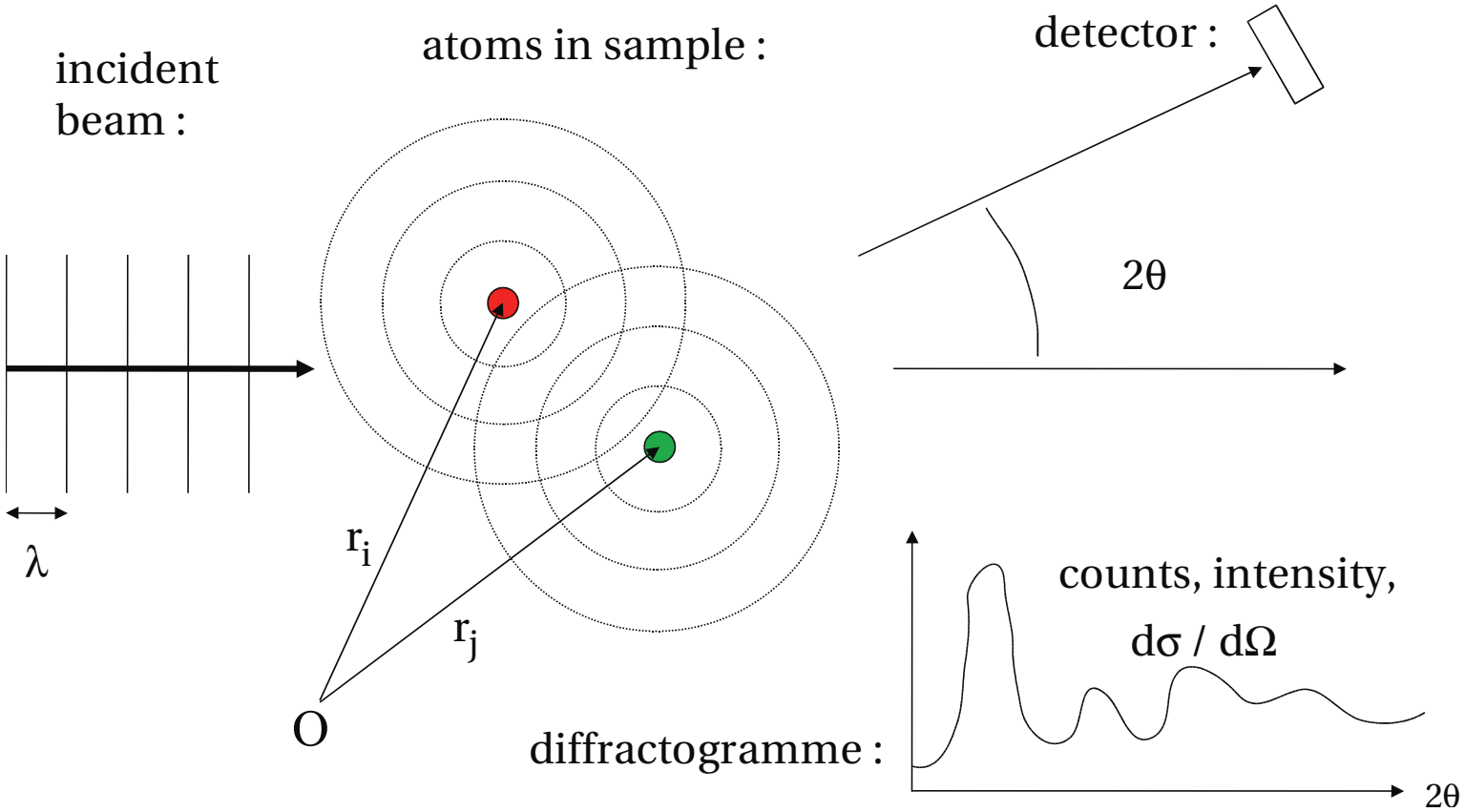


The spherical waves of scattering amplitude from all the atoms in a given quantum's coherence volume ($\phi \sim 100$ Å) interfere with each other at the detector, producing a diffraction pattern as a function of the scattering angle $2\theta$ or the scalar $q = (4\pi/\lambda)\ \sin(\theta)$.

# Coherence volume of a neutron wavepacket

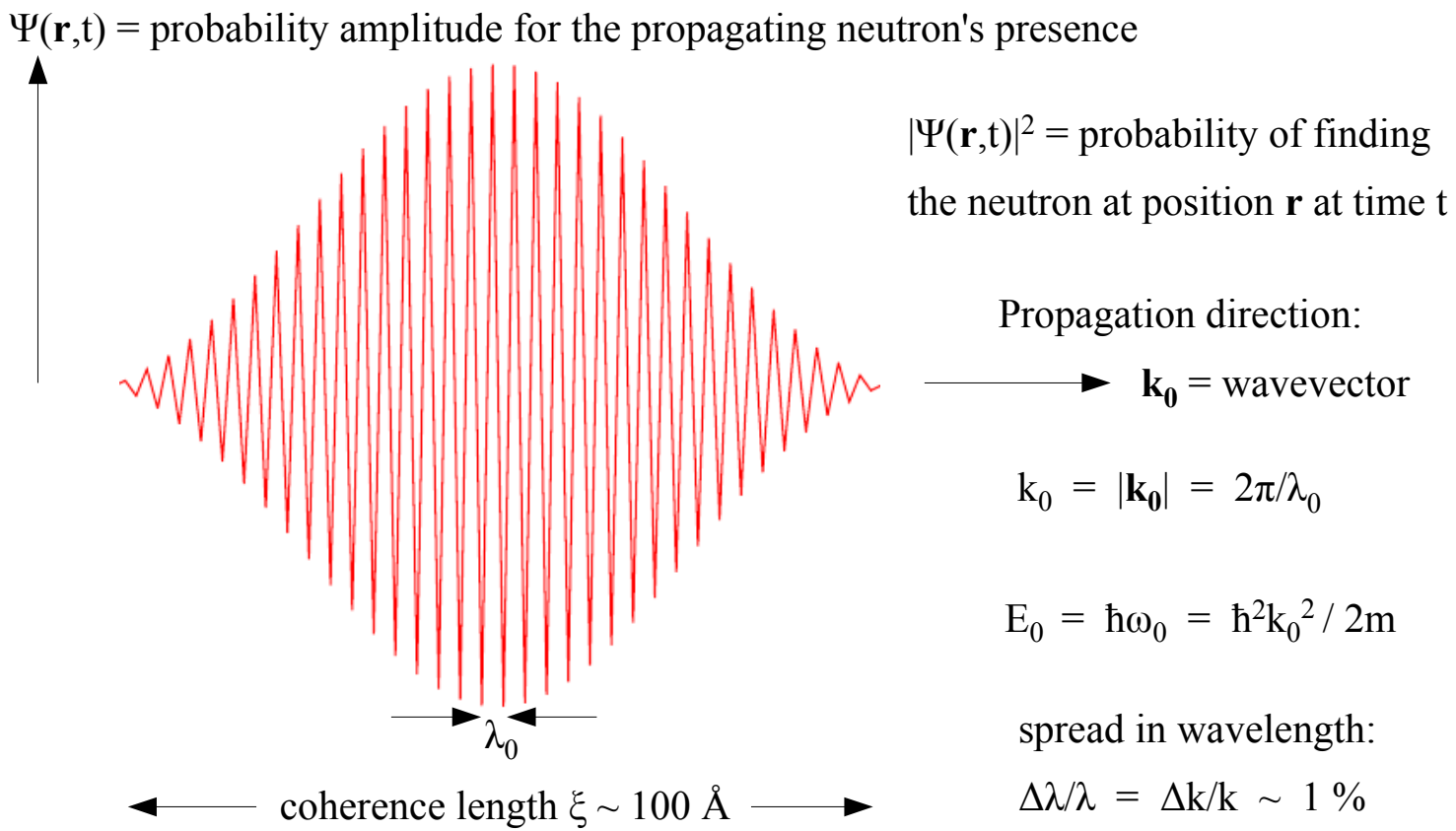


A Gaussian wavepacket of energy $\hbar\omega_0$ is localized in position and wavevector for each dimension as *e.g.* $\Delta x\, \Delta k_x = \hbar/2$ and propagates with group velocity $v_g = \mathrm{d}\omega/\mathrm{d}k$. The diffracting neutron has "seen" only the 100,000 or so atoms that "felt" its wavefunction $\Psi(\mathbf{r}, t)$ within the coherence volume $V_{\mathrm{coh}} \sim \xi^3$ of the diffraction event.

# Interference from 2 diffracting atoms

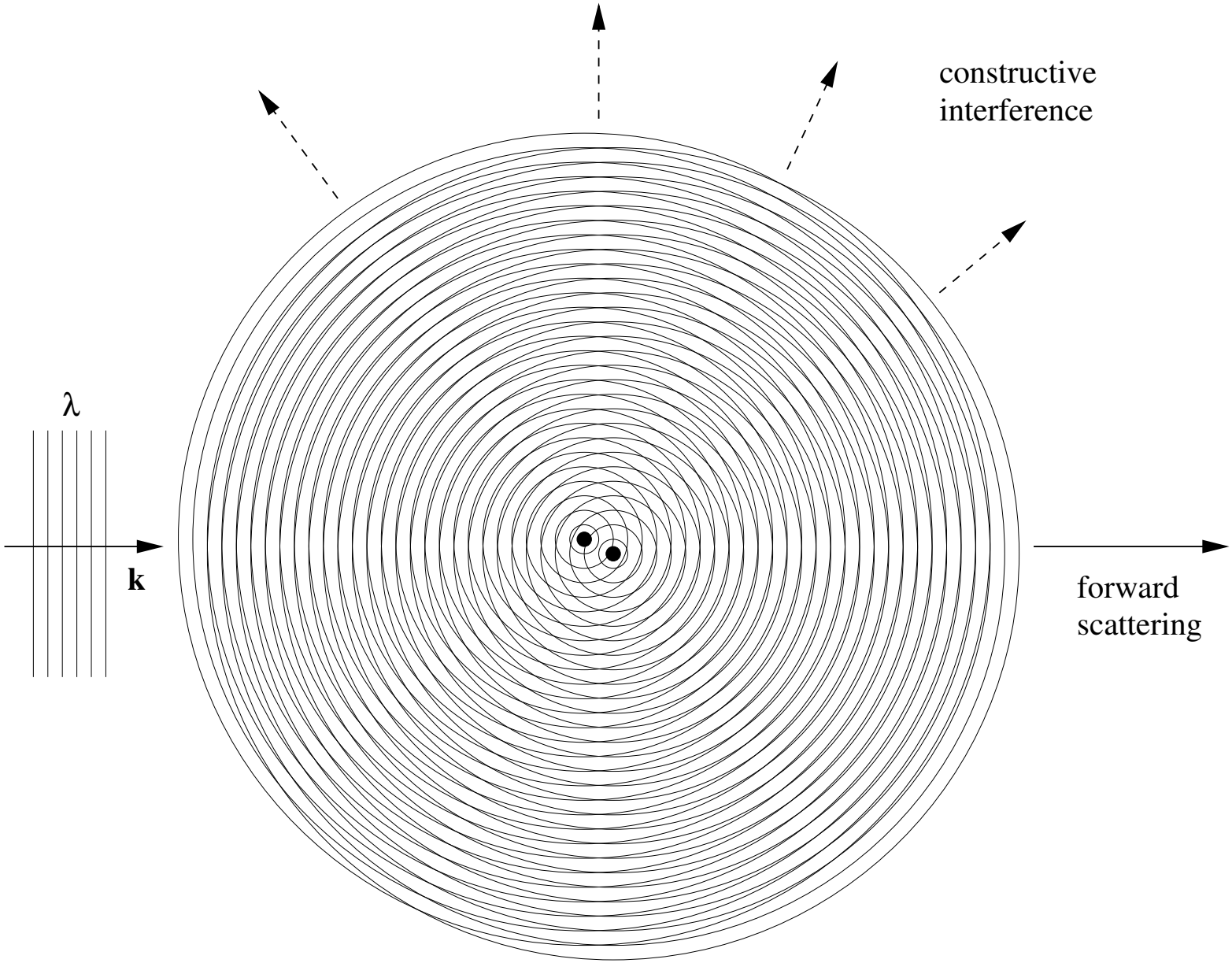

# Interference from an ordered array of 9 atoms

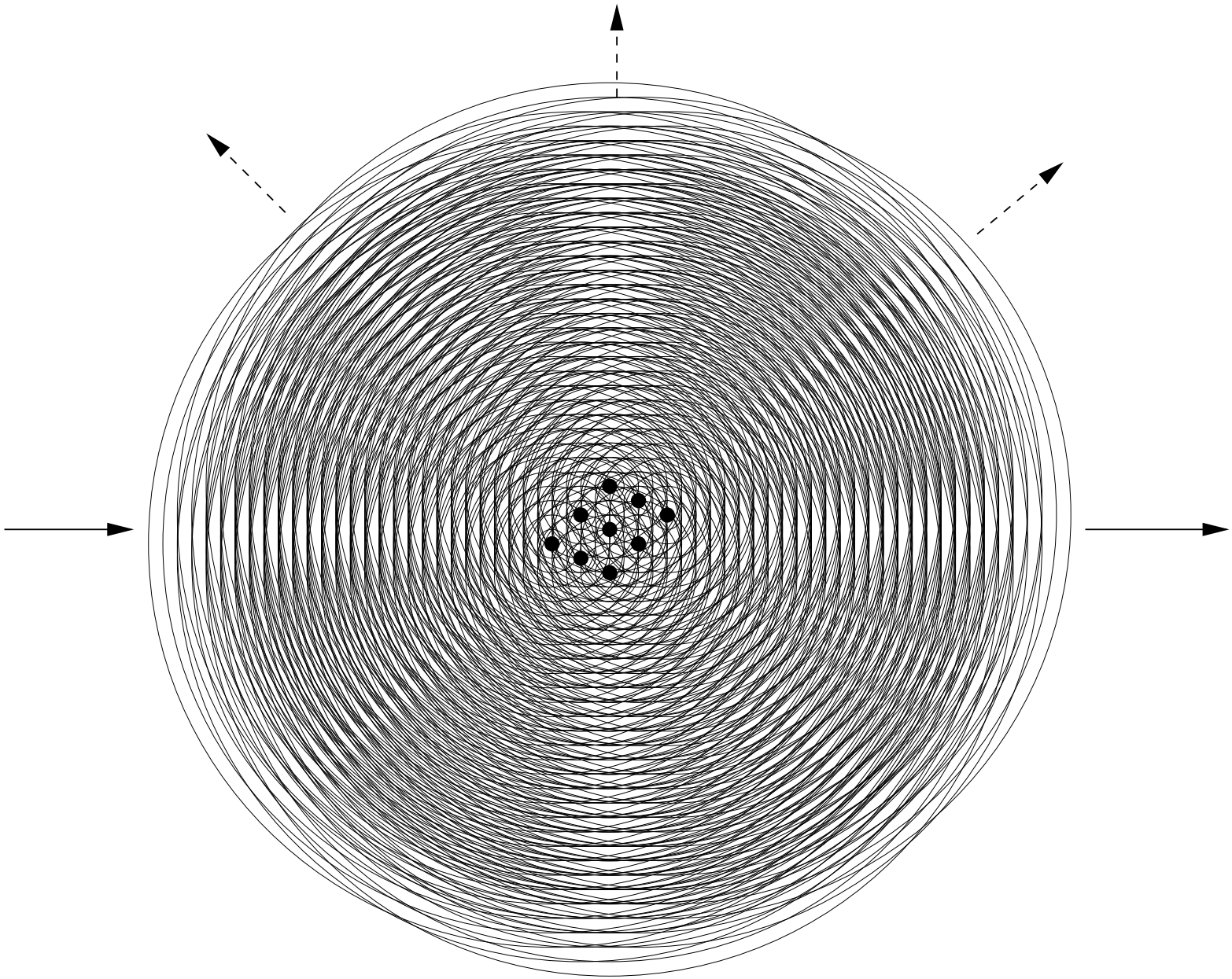

# Interference from an ordered array of 9 atoms

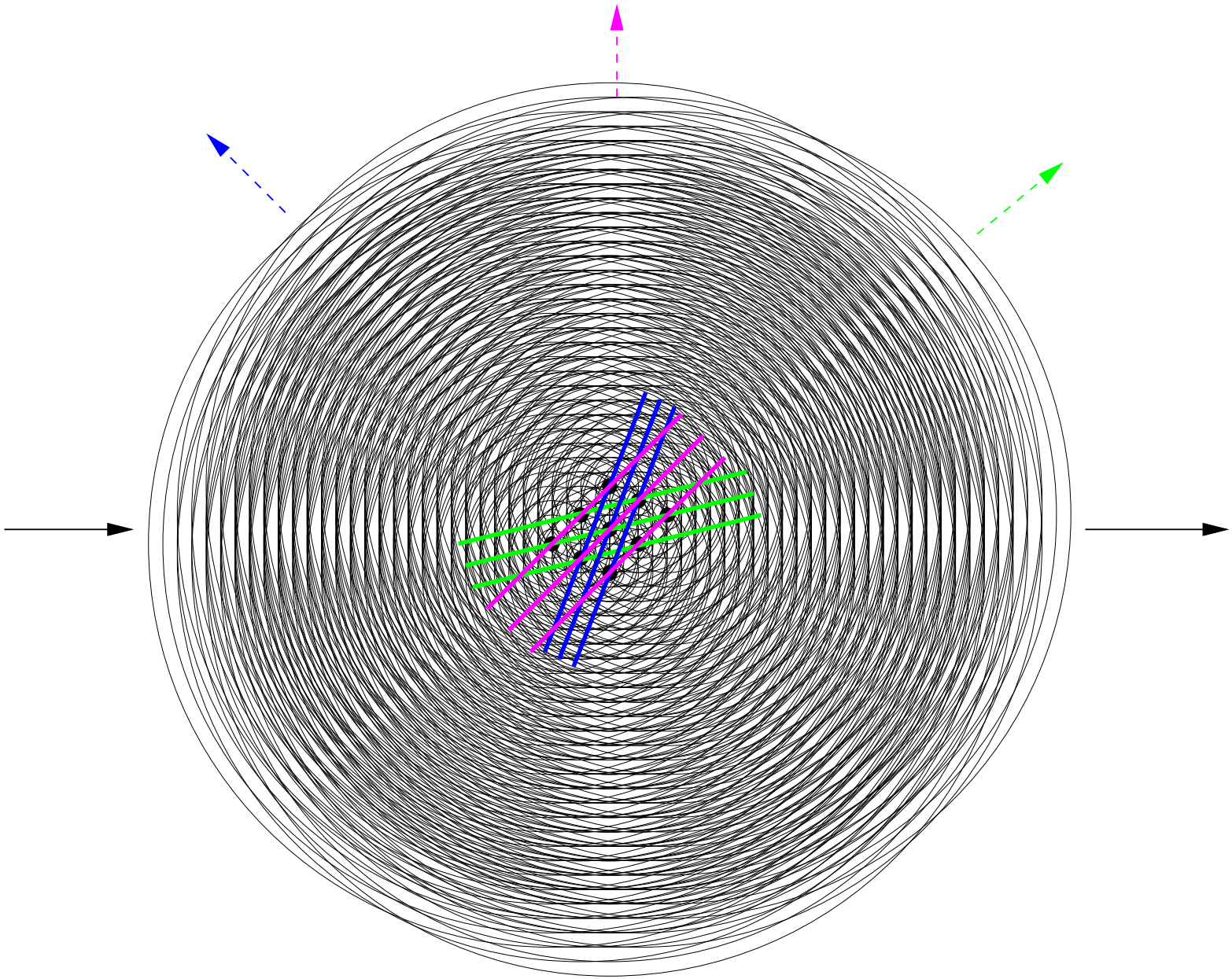

# Interference from a disordered array of 9 atoms

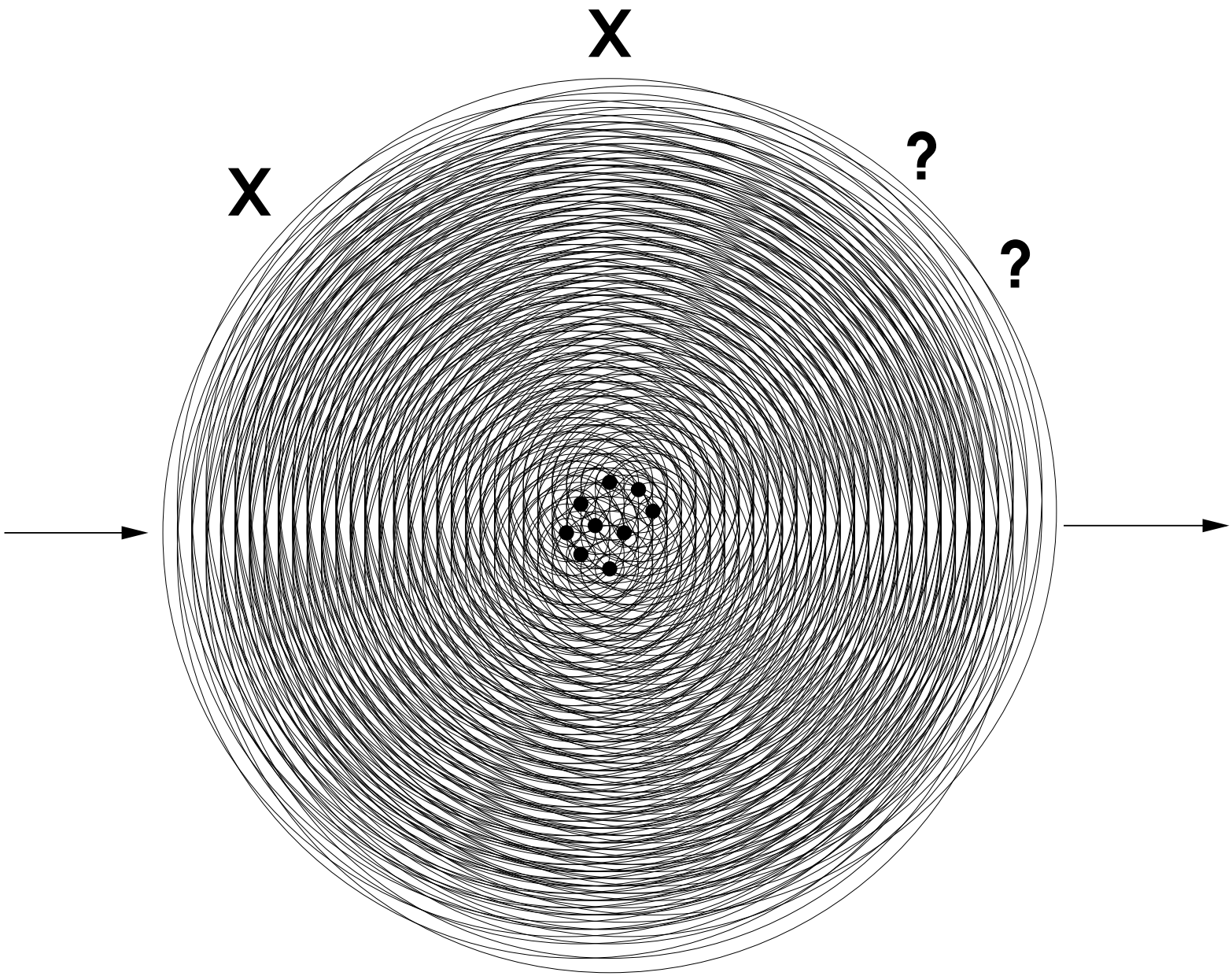

# Diffracted intensity from an ensemble of atoms

Constructive interference at the detector results when the path lengths followed by a neutron wave, as scattered by two different atoms, differ by a multiple of $\lambda$. This also holds for "reflection" from parallel atomic planes of period $d$ as shown by Bragg's law: $n\,\lambda = 2d\,\sin(\theta)$.

A pathlength difference of $n \cdot \lambda$ means a phase difference of $n \cdot 2\pi$. So, we can sum up all the scattered amplitudes $b_i$ and phases from all the diffracting atoms (*i.e.* within $V_{\rm coh}$) at positions $\mathbf{r}_i$ and write the total scattered amplitude propagating along $\mathbf{k}_{\rm f}$ towards the detector:

$$A_{\rm diff}(\mathbf{q}) \;=\; \sum_i^N b_i\, e^{i\mathbf{q}\cdot\mathbf{r}_i} \qquad\qquad b_i = \text{"scattering length"}$$

where $\mathbf{q} = \mathbf{k}_{\rm o} - \mathbf{k}_{\rm f}$ as before, and $|\mathbf{k}_{\rm f}| = |\mathbf{k}_0| = k \Rightarrow$ elastic. The diffracted intensity or counting rate recorded by the detector is then:

$$I(\mathbf{q}) \;\propto\; |A_{\rm diff}(\mathbf{q})|^2 = \left|\sum_i^N b_i\, e^{i\mathbf{q}\cdot\mathbf{r}_i}\right|^2 = \sum_{i,j}^N b_i b_j^*\, e^{i\mathbf{q}\cdot\mathbf{r}_{ij}}\ ,$$

where $\mathbf{r}_{ij} = \mathbf{r}_i - \mathbf{r}_j$ is the relative position of atom $i$ with respect to atom $j$, and $^*$ denotes the complex conjugate.

# Diffracted intensity from a periodic structure

The atoms of a crystal are arranged periodically within an ordered array or lattice of unit cells each having dimensions defined by the vectors **a**, **b** and **c**. The identical arrangement of atoms within each unit cell is called the basis or motif. The integer coefficients $u, v, w$ thus specify the position of a unit cell within the lattice $\mathbf{r}_{uvw} = u\mathbf{a} + v\mathbf{b} + w\mathbf{c}$, and the fractional coefficients $x_m, y_m, z_m$ specify the $m^{\text{th}}$ atom's position $\mathbf{r}_m = x_m\mathbf{a} + y_m\mathbf{b} + z_m\mathbf{c}$ within the motif:

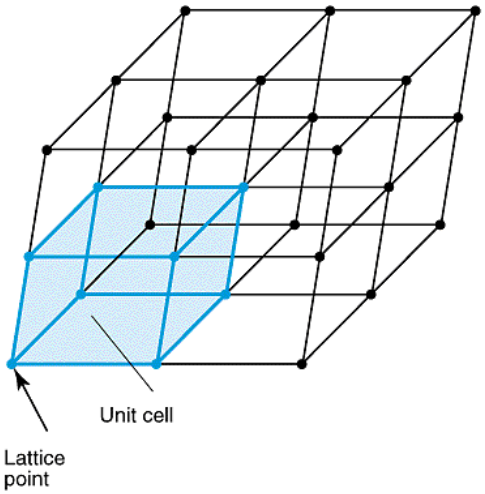


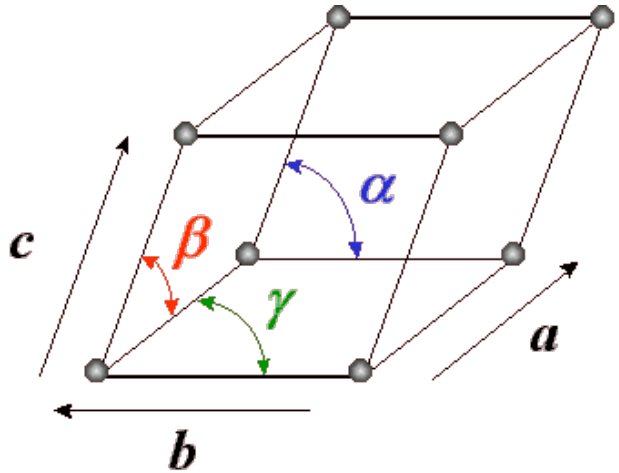


An atom's position in the crystal can then be written as:

$$\mathbf{r}_i = \mathbf{r}_{uvw} + \mathbf{r}_m = (u + x_m)\mathbf{a} + (v + y_m)\mathbf{b} + (w + z_m)\mathbf{c} \ .$$

# Diffracted intensity from a periodic structure

We can thus rewrite the sum of scattered amplitudes and phases as:

$$A_{\rm diff}(\mathbf{q}) \;=\; \sum_{i}^{N} b_i\, e^{i\mathbf{q}\cdot\mathbf{r}_i} \;=\; \sum_{u,v,w}^{\textbf{lattice}} \;\sum_{m}^{\textbf{motif}} b_{{\rm coh},m}\, e^{i\mathbf{q}\cdot(\mathbf{r}_{uvw}+\mathbf{r}_m)}$$

$$= \left[\sum_{u,v,w}^{\textbf{lattice}} e^{i\mathbf{q}\cdot\mathbf{r}_{uvw}}\right]\cdot\left[\sum_{m}^{\textbf{motif}} b_{{\rm coh},m}\, e^{i\mathbf{q}\cdot\mathbf{r}_m}\right] \;=\; L(\mathbf{q})\,M(\mathbf{q})\;,$$

where $b_{{\rm coh},m} = \overline{b_i}$ is the scattering length at site $m$ in the motif as averaged over the entire crystal. The complex function $L(\mathbf{q})$ is the form factor of the lattice that gives rise to Bragg peaks as a function of the lattice symmetry, and $M(\mathbf{q})$ is the structure factor of the motif (or basis) that modulates the intensity of the Bragg peaks:

$$I(\mathbf{q}) \;\propto\; |A_{\rm diff}(\mathbf{q})|^2 \;=\; |L(\mathbf{q})|^2\,|M(\mathbf{q})|^2$$

$$= \left[\sum_{u,v,w,u',v',w'}^{\textbf{lattice}} e^{i\mathbf{q}\cdot(\mathbf{r}_{uvw}-\mathbf{r}_{u'v'w'})}\right]\cdot\left[\sum_{m,m'}^{\textbf{motif}} b_{{\rm coh},m} b^{*}_{{\rm coh},m'}\, e^{i\mathbf{q}\cdot(\mathbf{r}_m-\mathbf{r}_{m'})}\right].$$

# Diffracted intensity from a periodic structure

Note that when we consider all lattice positions $\mathbf{r}_{uvw}$ and $\mathbf{r}_{u'v'w'}$ lying within a single plane, then the dot product $\mathbf{q} \cdot (\mathbf{r}_{uvw} - \mathbf{r}_{u'v'w'}) = 0$ implies that $\mathbf{q}$ is $\perp$ to that plane, consistent with the Bragg condition! *Hmmm*. In fact, it turns out that $\mathbf{q}$ satisfies the Bragg condition if and only if

$$\mathbf{q} \cdot \mathbf{r}_{uvw} = n2\pi \qquad n \in \mathbb{Z}, \quad \forall\, u, v, w \in \mathbb{Z}\ .$$

The set of all such $\mathbf{q}$ form a lattice of reciprocal-space vectors:

$$\mathbf{Q}_{hkl} = h\mathbf{a}^\star + k\mathbf{b}^\star + l\mathbf{c}^\star \qquad h, k, l \in \mathbb{Z}\ ,$$

where the reciprocal lattice basis vectors are given by:

$$\mathbf{a}^\star = \frac{2\pi}{V_{\rm cell}}\mathbf{b} \times \mathbf{c}\ , \qquad \mathbf{b}^\star = \frac{2\pi}{V_{\rm cell}}\mathbf{c} \times \mathbf{a}\ , \qquad \mathbf{c}^\star = \frac{2\pi}{V_{\rm cell}}\mathbf{a} \times \mathbf{b}\ ,$$

and where $V_{\rm cell}$ is the volume of the real-space unit cell. Note that $\mathbf{a} \cdot \mathbf{a}^\star = 2\pi$ but $\mathbf{b} \cdot \mathbf{a}^\star = \mathbf{c} \cdot \mathbf{a}^\star = 0$ and likewise for $\mathbf{b}^\star$ and $\mathbf{c}^\star$. Thus:

$$|L(\mathbf{Q}_{hkl})|^2 = \left| \sum_{u,v,w}^{\textbf{lattice}} e^{i\mathbf{Q}_{hkl} \cdot \mathbf{r}_{uvw}} \right|^2 = \left| \sum_{u,v,w}^{\textbf{lattice}} e^{i2\pi(hu+kv+lw)} \right|^2 = P^2$$

where $P$ is the total number of lattice points, whence a Bragg peak.

# Laue function for diffraction from *M* atomic planes

The diffraction peaks get sharper and sharper in angle as the number *M* of parallel diffracting crystal planes increases:

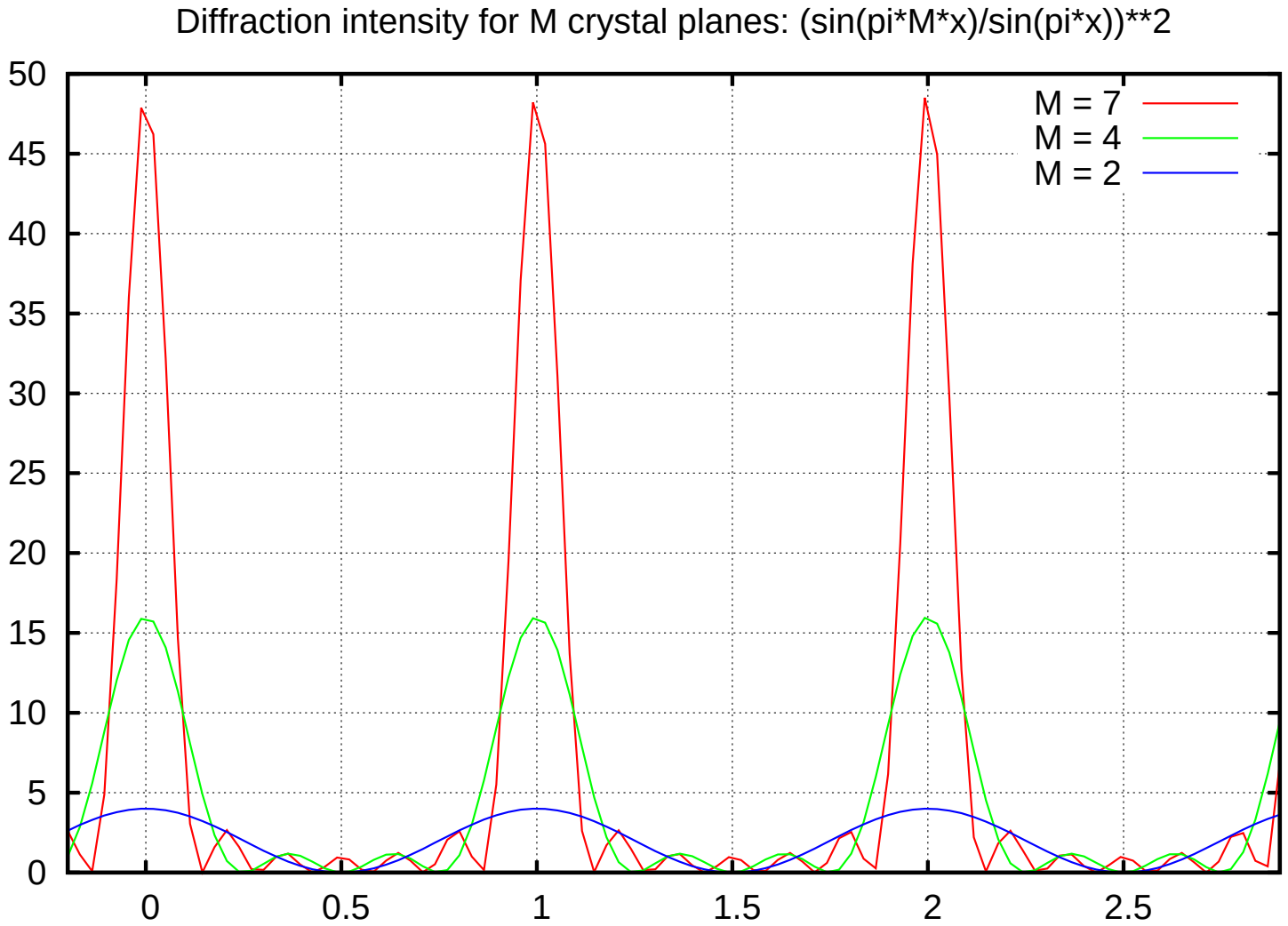

# The Patterson function as prelude to PDF($r$)

If the phases $\phi(hkl)$ of the structure factors $F(hkl)$ were known, one could calculate the scattering length density function $\rho(xyz)$:

$$\rho(xyz) = \frac{1}{V} \sum_{\substack{hkl \\ -\infty}}^{+\infty} |F(hkl)| \, . \, e^{-2\pi i[hx+ky+lz-\phi(hkl)]}$$

and thereby deduce the atomic positions $x, y, z$ within the unit cell. By using instead the measured intensity $I(hkl) \propto |F(hkl)|^2$ in the Fourier series, we eliminate $\phi(hkl)$ and obtain the Patterson function $P(uvw)$ of all *interatomic distances* ($u = x_i - x_j$, $v = y_i - y_j$, $w = z_i - z_j$) rather than of all absolute atomic positions in the unit cell:

$$P(uvw) = \frac{1}{V} \sum_{\substack{hkl \\ -\infty}}^{+\infty} |F(hkl)|^2 \, . \cos 2\pi \, [hu + kv + lw]$$

A radial average of $P(uvw)$ produces a 1-D pair-distribution function $P(r)$ based solely on elastic Bragg peak intensities, thus representing the sample's structure as averaged over space and time.

# The Patterson function as prelude to PDF($r$)

Although $P(uvw)$ has the same unit cell as the crystal's, it contains a high density of peaks and is by definition centrosymmetric. In 2-D:

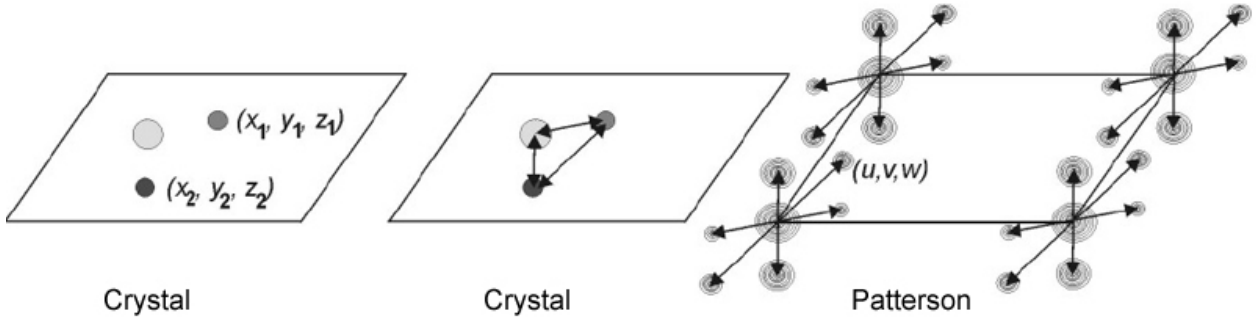


$P(uvw)$ is proportional to the product of the scattering lengths of the pair (or pairs!) of atoms separated by $u, v, w$, helping to determine their chemical identities. An "average atom" sits at $(uvw) = (000)$:

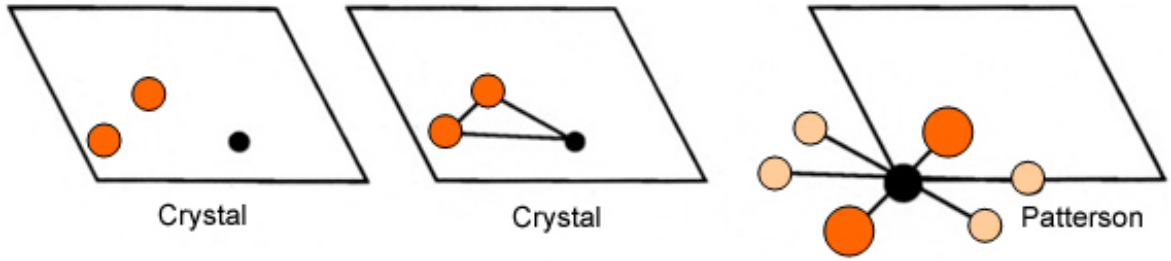


The higher symmetry of $P(uvw)$ is obtained from the crystal symmetry by setting the translational part of all symmetry operators to zero and assuring that each has a center of symmetry. Consequently, there are only 24 Patterson space groups.

# Debye-Waller factor and Thermal Diffuse Scattering

Increased amplitudes of atomic vibration **u** at higher $T$ lead to broader time-averaged "thermal clouds" of atomic positions that reduce Bragg peak intensities via the Debye-Waller factor: $\exp[-\langle(\mathbf{Q}_{hkl}\cdot\mathbf{u})^2\rangle/2]$:

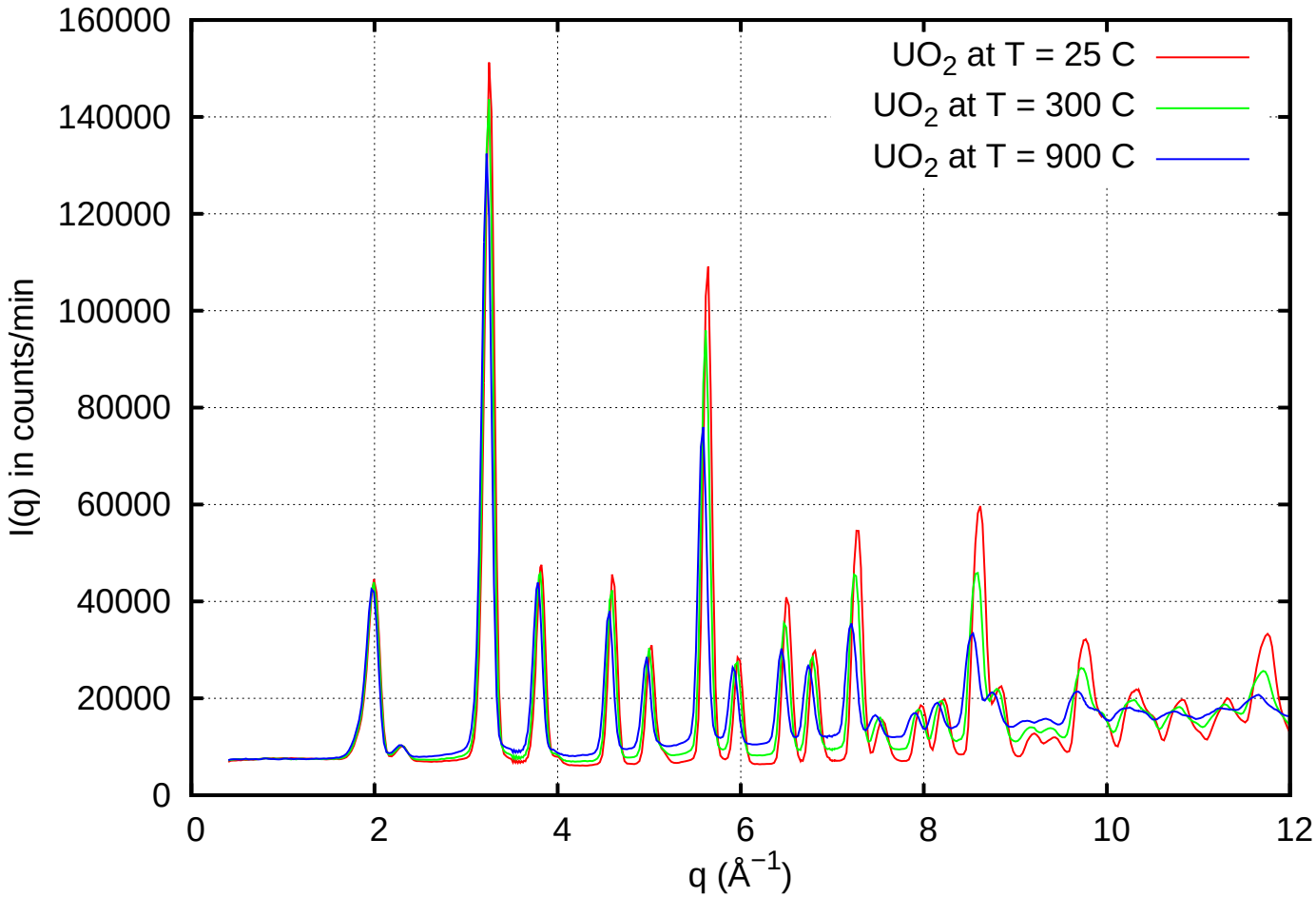


The lost intensity becomes Thermal Diffuse Scattering (TDS) at the base of the Bragg peaks.

# Debye-Waller factor and Thermal Diffuse Scattering

The D-W factor (*i.e.* a modulation) reduces the amplitude of a Bragg peak without affecting its width, thus reducing its integrated intensity.

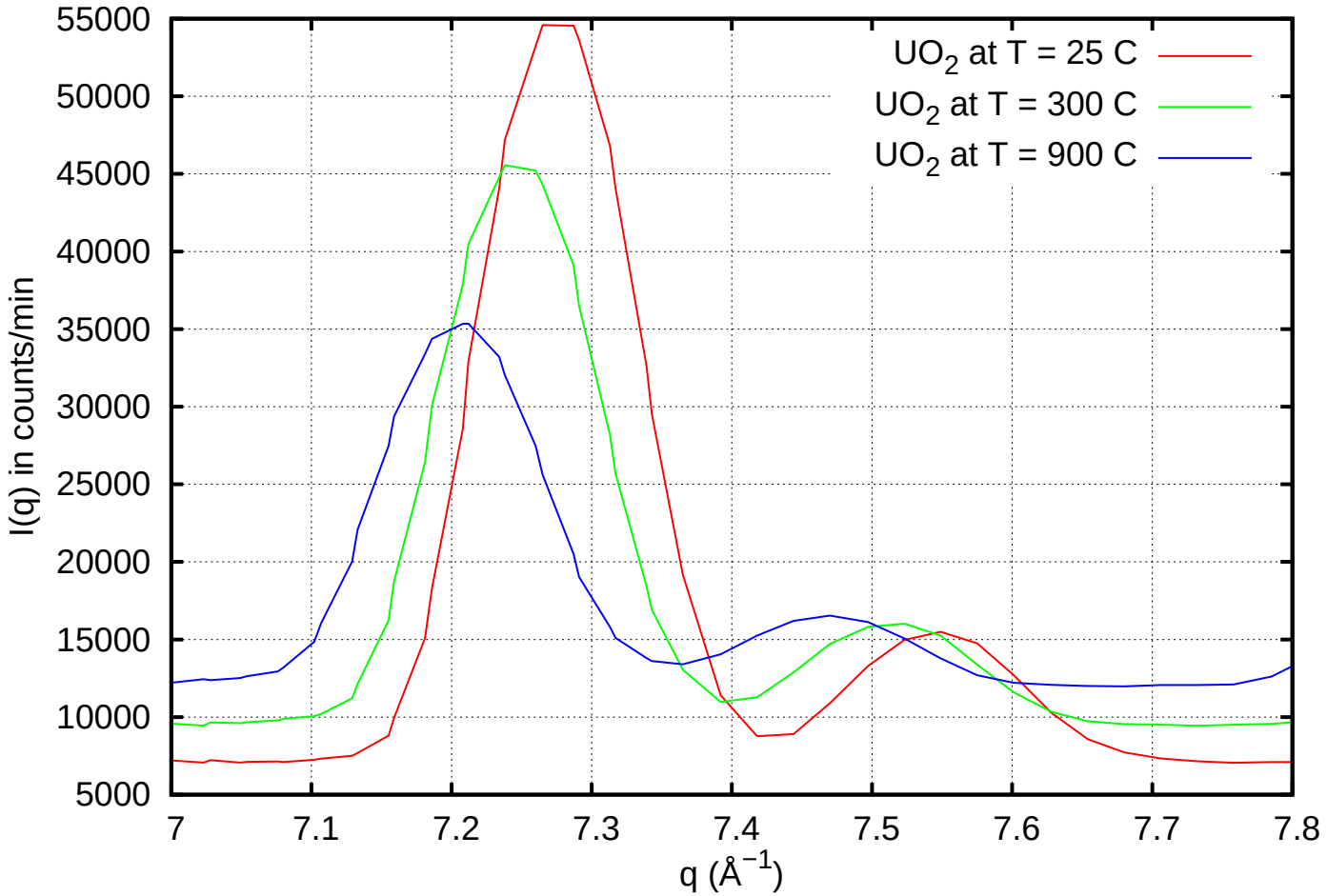


The Bragg peak positions naturally shift to lower *q* as the lattice expands at higher temperature.

# PDF-analysis

# PDF-analysis: FT of a powder diffraction pattern

***Basic idea:*** Disordered, nano-structured or reduced-dimensional crystals often lack sufficient long-range order to produce sharp diffraction peaks. It can then be advantageous to sacrifice $q$-space resolution by using short wavelengths to provide a high $q_{\max}$ and thus better $r$-space resolution $\Delta r = 3.79/q_{\max}$ after Fourier Transform (FT) of the diffraction pattern $S(q)$ or $F(q)$.

The resulting Pair-Distribution Function PDF($r$) is the distribution of relative interatomic distances with respect to an average atom at the origin (*i.e.* an ensemble of quasi-instantaneous local structures $\neq$ the time+space averaged structure from Rietveld).

$q$-space resolution $\Delta q$ leads to an envelope that modulates and limits the spatial extent of the PDF($r$) via $r_{\max} = (5.55/2)/\Delta q$.

**NB:** The PDF($r$) is not the output of structural refinement, and is therefore a *model-independent* result that can of course then be used as input for structural modelling/simulation in $r$-space.

# Total scattering and $S(\mathbf{q},\omega)$

So far we have been considering only elastically scattered neutrons, for which $|\mathbf{k}_f| = |\mathbf{k}_0| = k$ and therefore zero energy $\hbar\omega$ is exchanged with the sample. Furthermore, Bragg reflections are specular and therefore do not consider diffuse scattering from structural disorder. In reality, neutrons are also scattered inelastically and/or diffusely from the sample according to its (measurable) dynamic structure factor $S(\mathbf{q},\omega)$:

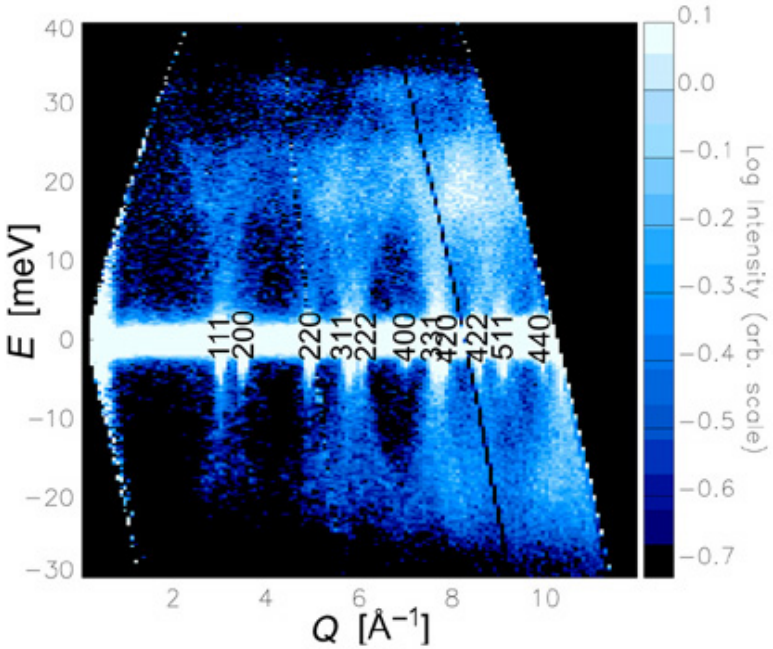


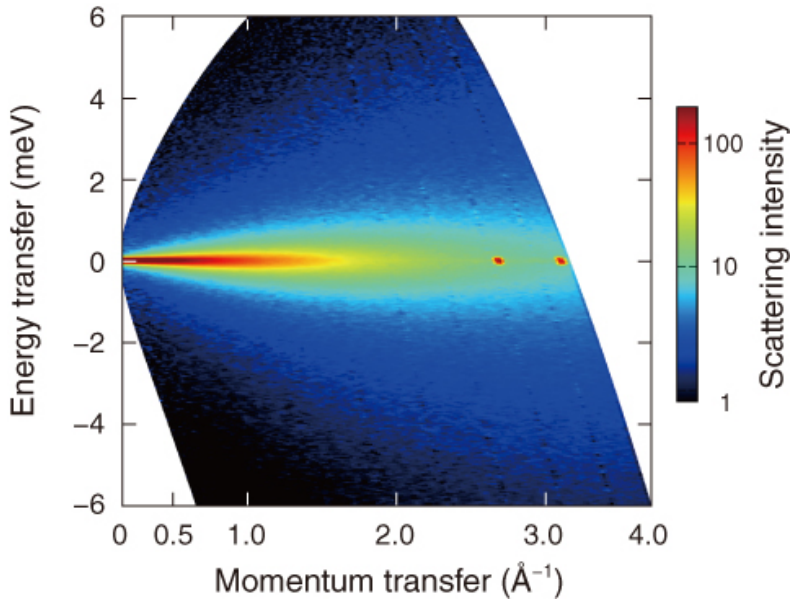


where the horizontal line near the center is the “elastic ridge” and corresponds to $S(\mathbf{q},\omega = 0)$, containing all Bragg reflections and also elastic diffuse scattering between and “underneath” the Bragg peaks.

# Total scattering and $S(\mathbf{q},\omega)$

Elastic scattering probes only the time-averaged structure of the sample, including therefore any static disorder (*e.g.* stacking faults, dislocations, interstitial atoms) giving rise to the diffuse scattering near and between the Bragg peaks in the $\omega = 0$ slice of $S(\mathbf{q},\omega)$ at left:

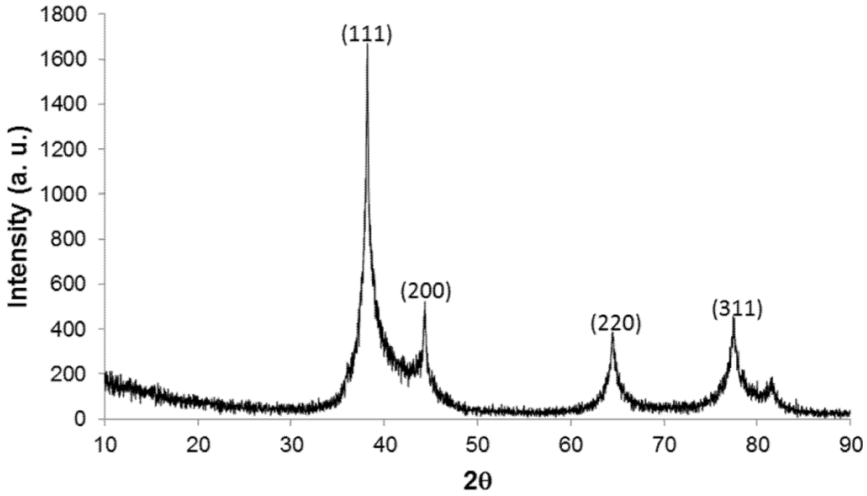


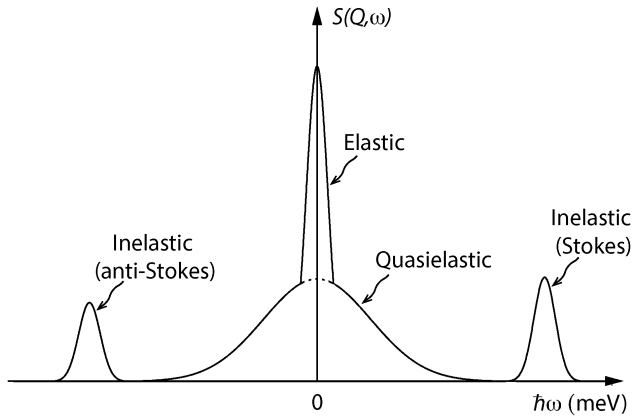


A constant-*q* slice of $S(\mathbf{q},\omega)$ (right) shows near the central elastic line (limited by instrumental energy resolution) some quasielastic scattering (from *e.g.* atomic diffusion) as well as inelastic peaks from coherent excitations (*e.g.* phonons) that exchanged well-defined energies $\hbar\omega$ with the scattered neutron. Thermal diffuse scattering TDS from atomic vibrations is both diffuse and inelastic. All diffuse/inelastic scattering reduces the elastic Bragg peak intensities analysed by *e.g.* Rietveld.

# General expression for diffraction

For a monochromatic-ish incident beam of energy $E_o$, a diffraction measurement simply integrates the double differential scattering cross-section over all possible energy exchanges $\hbar\omega = E_o - E_f$ between the neutron (or x-ray) and the $N$ atoms of the sample, in general at constant scattering angle $2\theta$ rather than at constant $q$:

$$\left.\frac{d\sigma}{d\Omega}\right|_{meas} = \int_{-\infty}^{E_o} d(\hbar\omega)\,\frac{d^2\sigma}{d\Omega\; dE_f}\,\varepsilon(E_f)\;,$$

$$\text{where} \qquad \frac{d^2\sigma}{d\Omega\; dE_f} = \frac{\sigma}{4\pi}\,\frac{k_f}{k_o}\,N\,S(\mathbf{q},\omega)$$

can refer to either the coherent or incoherent scattering case, for which $\mathbf{q} = \mathbf{k}_o - \mathbf{k}_f$ is the wavevector transfer, and $\varepsilon(E_f)$ is the detector efficiency. The finite incident energy $E_o$ leads to a non-zero "snapshot time" $\tau_{snapshot} \sim \hbar/E_o$ during which a neutron (or x-ray) probes the sample's structure within its coherence volume. Note that $\tau_{snapshot}$ is much smaller than the coherence time of the incident beam $\tau_{coh} = \xi_l/v = 0.07(m/\hbar)\,\lambda^3/\Delta\lambda \sim \hbar/\delta E_o$ where $m$ is the neutron's mass, $v$ its incident speed, and $\delta E_o$ the standard deviation of $E_o$.

# Static approximation

When the incident energy $E_o$ exceeds the maximum possible energy transfer $\hbar\omega_{max}$ between the scattered quantum and the excitations in the sample, and for $\varepsilon(E_f) = 1$, it is perfectly valid to use the *static approximation* to derive the *differential scattering cross-section* for diffraction as a function of **q** only:

$$\frac{d\sigma}{d\Omega}(\mathbf{q}) = \overline{\left\langle \left| \sum_i^N b_i \, e^{i\mathbf{q}\cdot\mathbf{r}_i} \right|^2 \right\rangle} = \left\langle \sum_{i,j}^N \overline{b_i b_j^*} \, e^{i\mathbf{q}\cdot\mathbf{r}_{ij}} \right\rangle ,$$

where $b_i$ is the scattering length of the $i^{th}$ atom at position $\mathbf{r}_i$, and $\mathbf{r}_{ij} = \mathbf{r}_i - \mathbf{r}_j$. The $<>$ represent a thermal average and the horizontal bars an ensemble average over the different possible coherence volumes within the sample, each having a particular assignment of scattering lengths in the case of neutron diffraction. Note that scattering lengths are *q*-dependent in the case of x-ray diffraction (XRD).

When $E_o < \hbar\omega_{max}$, as is often the case for neutron diffraction (ND), the non-satisfaction of the static approximation requires inelasticity corrections to be made to the measured diffraction patterns.

# Case of a monoatomic sample (only one $Z$)

$\Rightarrow (d\sigma/d\Omega)(\mathbf{q})$ measures an *ensemble average* of quasi-instantaneous snapshots of local structures (*i.e.* within the neutron coherence volume) throughout the sample volume over the duration of the experiment.

In neutron scattering, a monoatomic sample can have a distribution of scattering lengths $b_i$, but there is no correlation between $b_i$ and the structural environment of $\mathbf{r}_i$. The ensemble average over coherence volumes then leads to an expression involving a $\mathbf{q}$-dependent coherent term and an isotropic incoherent term:

$$\frac{1}{N}\left[\frac{d\sigma}{d\Omega}(\mathbf{q})\right] = \overline{b}^2 S(\mathbf{q}) + (\overline{b^2} - \overline{b}^2)$$

where the sample's average scattering length $\overline{b} = b_{\rm coh}$, and where $(\overline{b^2} - \overline{b}^2) = var(b)$ is simply the variance of scattering lengths throughout the sample. The alternative expression:

$$\frac{1}{N}\left[\frac{d\sigma}{d\Omega}(\mathbf{q})\right] = \overline{b}^2 \left[S(\mathbf{q}) - 1\right] + \overline{b^2}$$

comprises a "distinct" term (interference between different atoms) and a "self" term (self-interference from individual atoms).

# Case of a monoatomic sample (cont'd)

The *static structure factor* (dimensionless) is then given by

$$S(\mathbf{q}) = \frac{1}{N}\left\langle \sum_{i,j}^{N} e^{i\mathbf{q}\cdot\mathbf{r}_{ij}} \right\rangle$$

and reduces to

$$S(q) = \frac{1}{N}\left\langle \sum_{i,j}^{N} \frac{\sin(qr_{ij})}{(qr_{ij})} \right\rangle$$

in the case of conical Debye-Scherrer diffraction from an isotropic sample (*e.g.* powder, polycrystal, liquid, glass) for which

$$q = |\mathbf{q}| = (4\pi/\lambda)\ \sin(\theta)$$

and $2\theta$ is the diffraction angle with respect to to the incident beam. Finally, for an incident flux $\Phi$ and a detector cell of solid angle $d\Omega$, the measured intensity (counts/s) from an isotropic sample is given by

$$I(q) = \Phi\ \frac{d\sigma}{d\Omega}(q)\ d\Omega$$

which, notably, is a function of $q$ *only*.

# $S(q)$ for a monoatomic glass/liquid

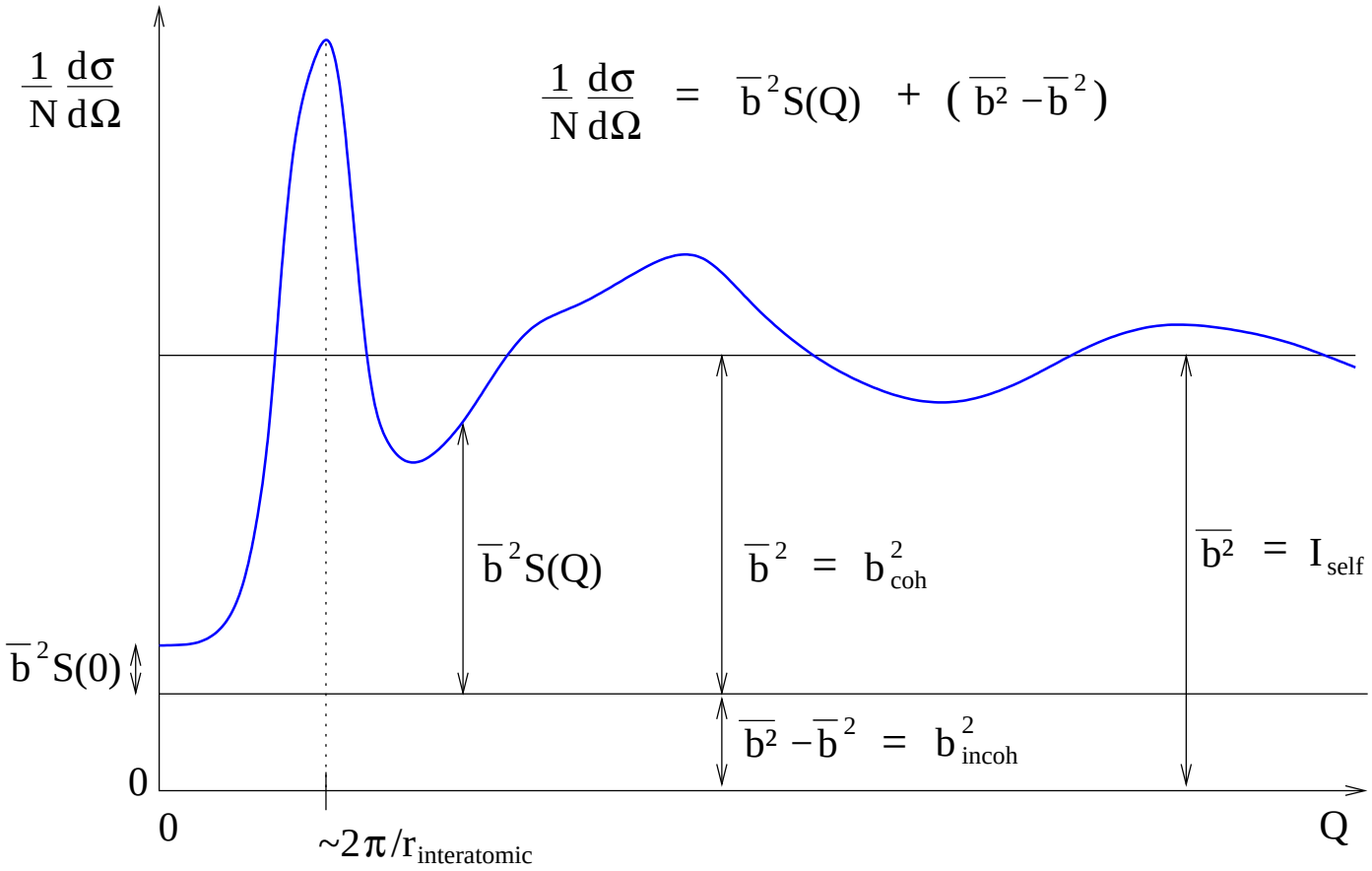


Absence of long-range order leads to broad peaks in the diffraction pattern of a glass/liquid, and in the case of an ergodic system such as a liquid or gas, there also exists a useful thermodynamic limit: $S(q \to 0) = \rho_0 \chi_T k_B T$ where $\rho_0$ is the total atomic number density and $\chi_T$ is the isothermal compressibility.

# Real-space functions (monoatomic case)

Fourier transform gives the *pair-distribution function* $g(r)$ which is proportional to the probability of finding an atom at a distance $r$ from an average atom taken as the origin:

$$g(r) - 1 = \frac{1}{2\pi^2 r \rho_o} \int_0^\infty q\,[S(q) - 1] \sin(qr)\, dq$$

in addition to the density function $D(r)$ (also called $G(r)$) used for "PDF-analysis":

$$\mathrm{PDF}(r) = G(r) = D(r) = 4\pi r \rho_o\,[g(r) - 1]$$

$$= \frac{2}{\pi} \int_0^\infty q\,[S(q) - 1] \sin(qr)\, dq$$

as well as the radial distribution function:

$$\mathrm{RDF}(r) = 4\pi r^2 \rho_o\, g(r)$$

whose integration across peaks yields atomic coordination numbers.

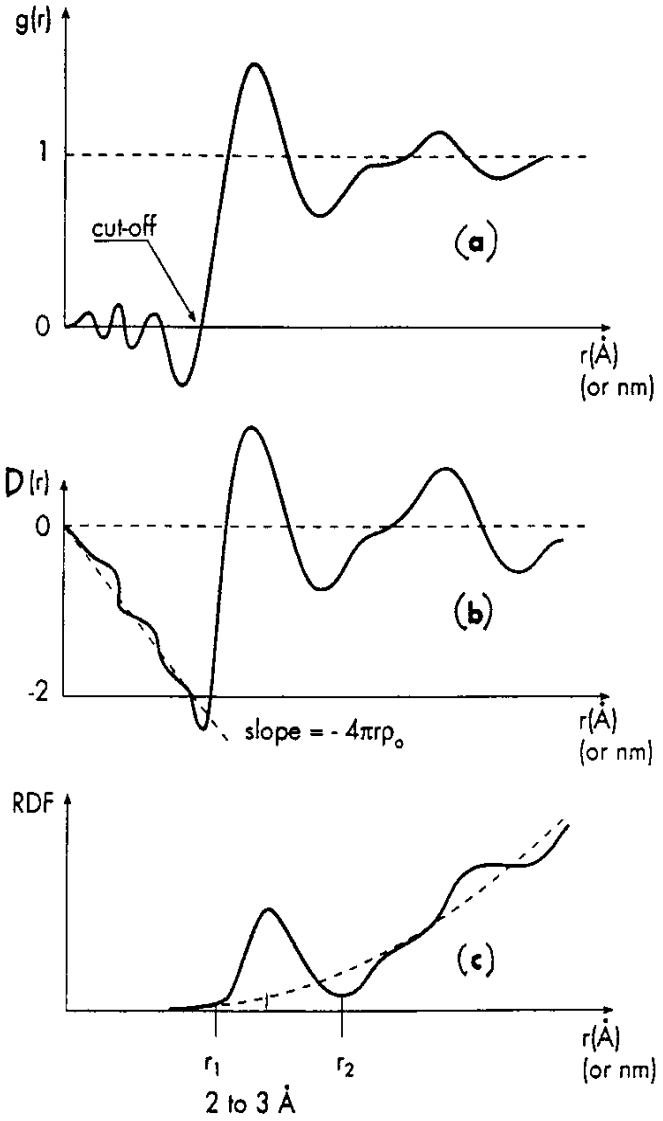

# Disorder can mean more information, not less

For a monoatomic fluid at temperature $T$ in the low-density limit, a *classical* mean-field theory relates $g(r)$, obtainable from diffraction, to the interatomic pair potential:

$$u(r) = -k_B T \ln[g(r)],$$

from which follows the interatomic force $\mathbf{F}(r) = -\vec{\mathrm{grad}}[u(r)]$, and thereby $v_{\mathrm{sound}}$, etc. For realistic densities, an iterative procedure leads to an effective pair potential $u_{\mathrm{eff}}(r)$ (*e.g.* EPSR analysis).

In effect, the distribution of interatomic distances given by $g(r)$ in a liquid or glass "probes" the shape of $u(r)$, since energetically unfavorable distances will be more rare than favorable ones. By contrast, diffraction measurements on a crystalline sample cannot give information about $u(r)$ without recourse to modelling.

Note that the above expression also implies that $g(r)$, the structure measured via diffraction, is independent of atomic mass in a classical picture. Any observed differences in structure, *e.g.* between the $(d\sigma/d\Omega)(\mathbf{q})$ of $H_2O$ vs $D_2O$ as measured by x-ray diffraction, are necessarily due to QM effects.

# Case of a polyatomic sample (several $Z$)

In a polyatomic system, the chemical affinities of $n$ different atomic species $Z_\alpha$ necessarily leads to a correlation at atomic sites $\mathbf{r}_i$ between the structural environment and the average scattering length $\overline{b}_\alpha$. This correlation prevents a proper definition of a dimensionless $S(q)$, but the scattered intensity can still be expressed as the sum of a distinct term (the interference function $F(q)$) and a total self-scattering term:

$$\frac{1}{N}\left[\frac{d\sigma}{d\Omega}(q)\right] = \sum_{\alpha,\beta}^{n} c_\alpha c_\beta \overline{b}_\alpha \overline{b}^*_\beta \left[S_{\alpha\beta}(q) - 1\right] + \sum_{\alpha}^{n} c_\alpha \overline{b^2}_\alpha \ ,$$

where $c_\alpha$ is the fraction or concentration of atomic species $Z_\alpha$, and the *partial* structure factor (PSF) $S_{\alpha\beta}(q)$ is the Fourier transform of the *partial* pair-distribution function (PPDF) $g_{\alpha\beta}(r)$, which is in turn proportional to the probability of finding an atom of type $Z_\beta$ at a distance $r$ from an atom of type $Z_\alpha$ taken as the origin:

$$g_{\alpha\beta}(r) - 1 = \frac{1}{2\pi^2 r \rho_o} \int_0^\infty q \left[S_{\alpha\beta}(q) - 1\right] \sin(qr)\, dq \ .$$

# Atomic distributions in glass/liquid versus crystal

Liquid/Glass :

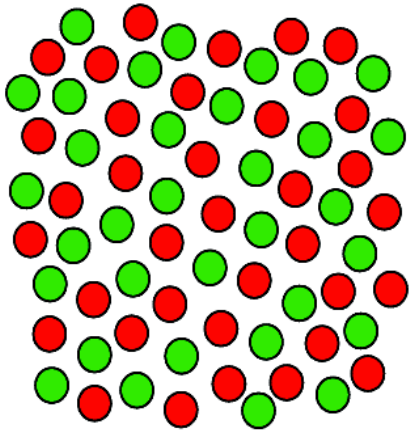

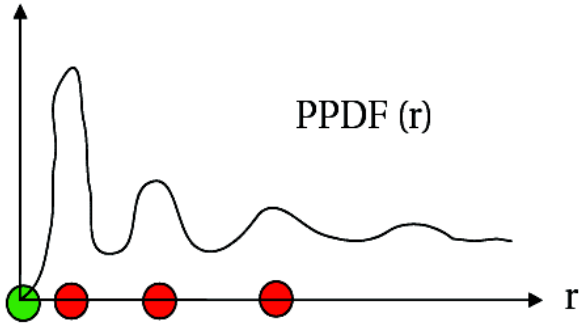


Crystal :

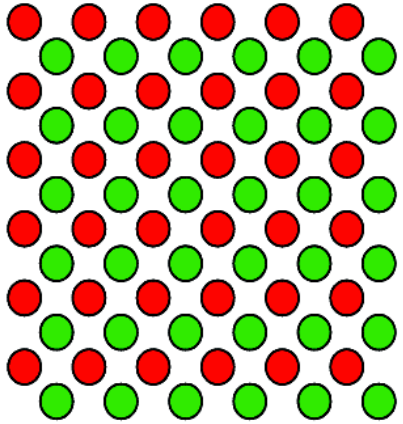

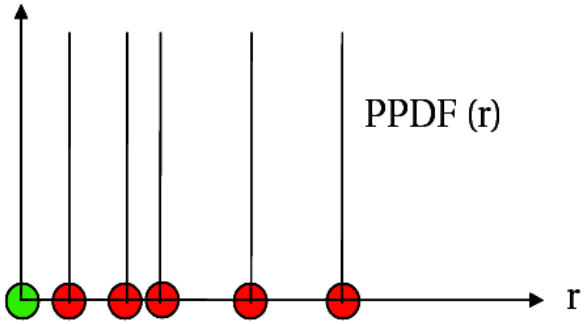


These *partial* PDFs or PPDFs (*e.g.* from NDIS) represent an ensemble of quasi-instantaneous spatial correlations between red and green atoms: more specifically $g_{GR}(r)$ which is proportional to the average probability of finding a Red atom at a distance $r$ from a Green atom.

# The Convolution Theorem

The *convolution* of two functions $f(q)$ and $g(q)$ is given by:

$$f(q) \otimes g(q) = (f \otimes g)(q) = \int_{-\infty}^{\infty} f(q')\, g(q - q')\, dq'$$

where $q'$ is the (dummy) variable of integration.

The *convolution theorem* states that the Fourier Transform (FT) of a convolution is the simply the product of the Fourier Transforms:

$$\mathrm{FT}[f(q) \otimes g(q)] = \mathrm{FT}(f(q))\,\mathrm{FT}(g(q)) = F(r)\; G(r)$$

so that a convolution in $q$-space gives a modulation in $r$-space, and vice-versa of course. Therefore deconvolution in $q$-space should be as simple as FT-ing to $r$-space, dividing two functions, and then FT-ing back to $q$-space. For example, if the measured diffraction pattern is $I(q) = f(q) \otimes g(q)$, where $g(q)$ is the real diffraction pattern and $f(q)$ is the known resolution function, then:

$$g(q) = \mathrm{FT}[\,\mathrm{FT}(I(q)) \,/\, \mathrm{FT}(f(q))\,] \quad .$$

# Convolution versus modulation of diffraction data

Consider the (unreal) case of diffraction data having a $q$-independent resolution function of $\mathrm{FWHM_q}$. The FT of a Gaussian with standard deviation $\sigma_q$ is also a Gaussian but with $\sigma_r = 1/\sigma_q$. And since:

$$\mathrm{HWHM}_q = \mathrm{FWHM_q}/2 = \sqrt{\ln(4)}\,\sigma_q = 1.18\,\sigma_q$$

then the FT of a Gaussian of width $\mathrm{FWHM}_q$ is a Gaussian of width

$$\mathrm{FWHM}_r = 4\ln(4)/\mathrm{FWHM}_q = 5.55/\mathrm{FWHM}_q$$

and therefore *not* $2\pi/\mathrm{FWHM}_q$. A sharp resolution function of small $\mathrm{FWHM}_q$ for the diffraction data will therefore lead to a broad or gentle modulation of large $\mathrm{FWHM}_r$ for the $\mathrm{PDF}(r)$, and vice-versa.

Note that diffraction data of finite $q_{\max}$ can be considered to be data of infinite $q_{\max}$ but modulated by a Heaviside step function whose FT is

$$\mathrm{sinc}(r) = \sin(r)/r \quad \text{having} \quad \mathrm{FWHM}_r = 3.79/q_{\max}$$

so that the theoretical $\mathrm{PDF}(r)$ should be convolved with $\mathrm{sinc}(r)$ before comparison to data. This is the source of the "low-$r$ wiggles" in the FTs of diffraction data, which in fact exist around all sharp peaks in $\mathrm{PDF}(r)$.

# Coherence volume for a scattered quantum

For each particle/wave emitted by an incoherent source of transverse FWHM size $H$ by $V$, scattered by a sample at a distance $L$ and then detected, purely geometric considerations impose a limit to the size of the scattering region within the sample over which a given quantum's scattered (from different atoms) amplitudes can be added coherently.

Assuming for convenience a Gaussian wavepacket for the incident quantum (*e.g.* x-ray or neutron), the Uncertainty Principle can be used to relate the standard deviations of its position and wavenumber:

$$\delta x_j \, \delta k_j \; = \; 1/2 \qquad \text{since} \qquad \delta x_j \, \delta p_j \; = \; \hbar/2$$

where the dimensions $j = h, v$ are transverse to the incident beam while $j = l$ is parallel (*i.e.* longitudinal). In terms of FWHM for the wavepacket:

$$\xi_j \, \Delta k_j \; = \; \frac{4\ln(4)}{2} \qquad \Rightarrow \qquad \xi_j \; = \; \frac{5.55}{2 \, \Delta k_j}$$

where the mutually orthogonal *coherence lengths* $\xi_j$ are the FWHM dimensions of the (roughly ellipsoidal) *coherence volume* $V_{\rm coh} = \xi_h \xi_v \xi_l$ from which the quantum scattered somewhere in the sample.

# Coherence volume for a scattered quantum (cont'd)

The $\Delta k_j$ are given by the collimation FWHM's (small angle approx.) and by the monochromaticity (FWHM $\Delta\lambda$) of the incident beam:

$$\Delta k_{h,v} = \frac{2\pi}{\lambda}\frac{H,V}{L} \quad \text{and} \quad \Delta k_l = \frac{2\pi}{\lambda}\frac{\Delta\lambda}{\lambda}$$

and thus the 3 coherence lengths:

$$\xi_{h,v} = \lambda\frac{\ln(4)}{\pi}\frac{L}{H,V} = 0.44\,\lambda\frac{L}{H,V} \quad \text{and} \quad \xi_l = 0.44\,\lambda\frac{\lambda}{\Delta\lambda}$$

increase as the collimation and monochromaticity improve.

NB: In general, the sample-to-detector optics (*e.g.* $\alpha_3$ collimation) also contribute to the instrumental resolution function of the diffraction pattern. In spite of occuring after the scattering event, such a *post-selection* of the scattered quanta leads to additional and complementary expressions in the above formulæ for $\xi_j$.

In the simplistic case of a constant-ish FWHM resolution of $\Delta q$ for the final diffraction pattern, the FWHM coherence length in the diffraction plane of the scattering vector $\mathbf{q}$ is simply $\xi_q = 5.55/\Delta q$.

# *q*-space versus *r*-space representations of data

Diffraction data at high $q_{max}$ show decreasing Bragg-peak intensities due to the Debye-Waller effect (thermal averaging of atomic positions), from static disorder, and also because of limited *q*-space resolution:

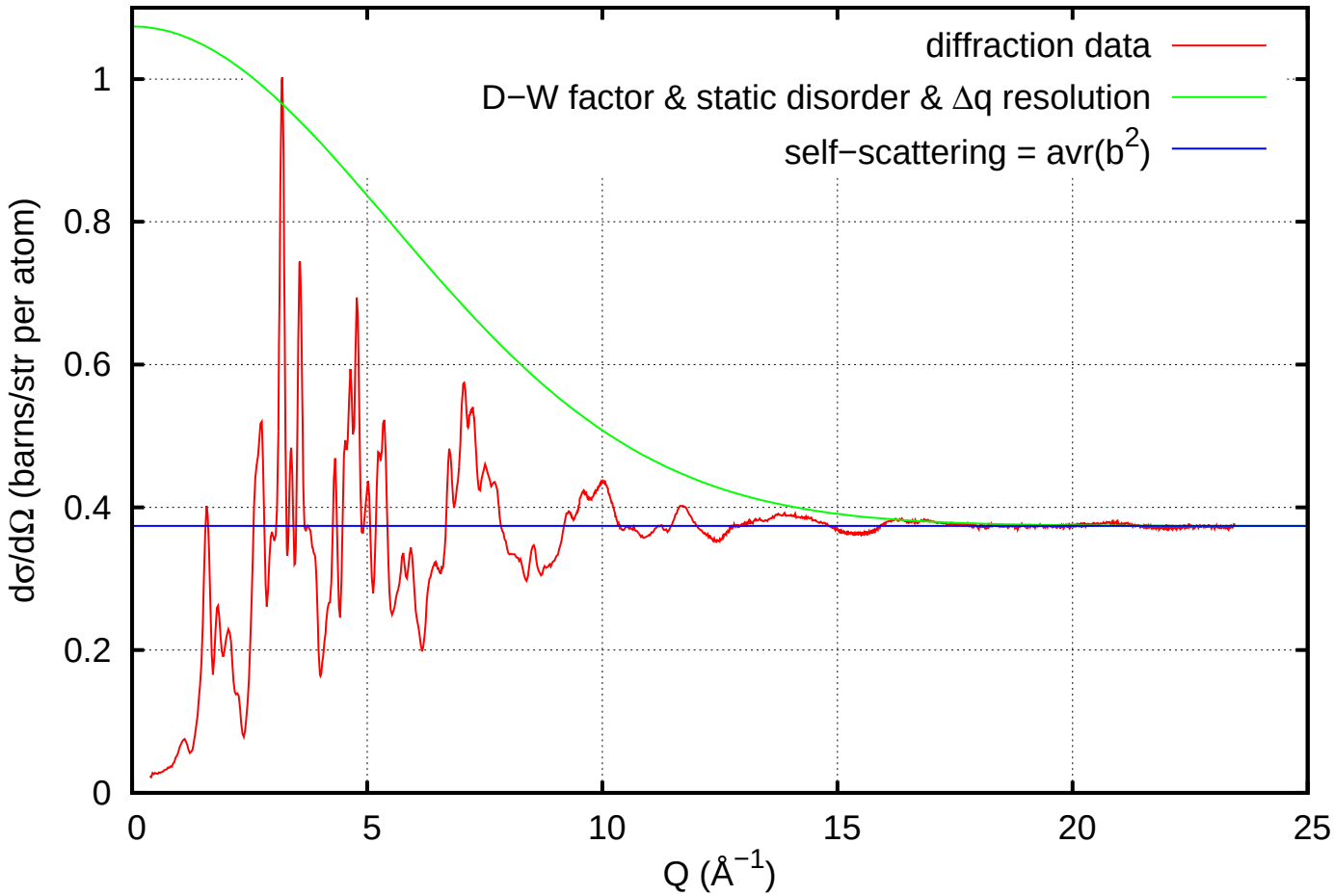


The diffraction intensity ultimately converges to the self-scattering limit $I_{self} = \overline{b^2}$ when $q_{max}$ is high enough.

# *q*-space versus *r*-space representations of data

The diffuse scattering "underneath" the Bragg peaks, subtracted away as "background" by Rietveld refinement, contains information about dynamic disorder (*e.g.* Thermal Diffuse Scattering = TDS) and static disorder (*e.g.* lattice-constant fluctuations $\Delta a/a$). The Bragg peak widths are generally limited by the instrumental resolution $\Delta q$:

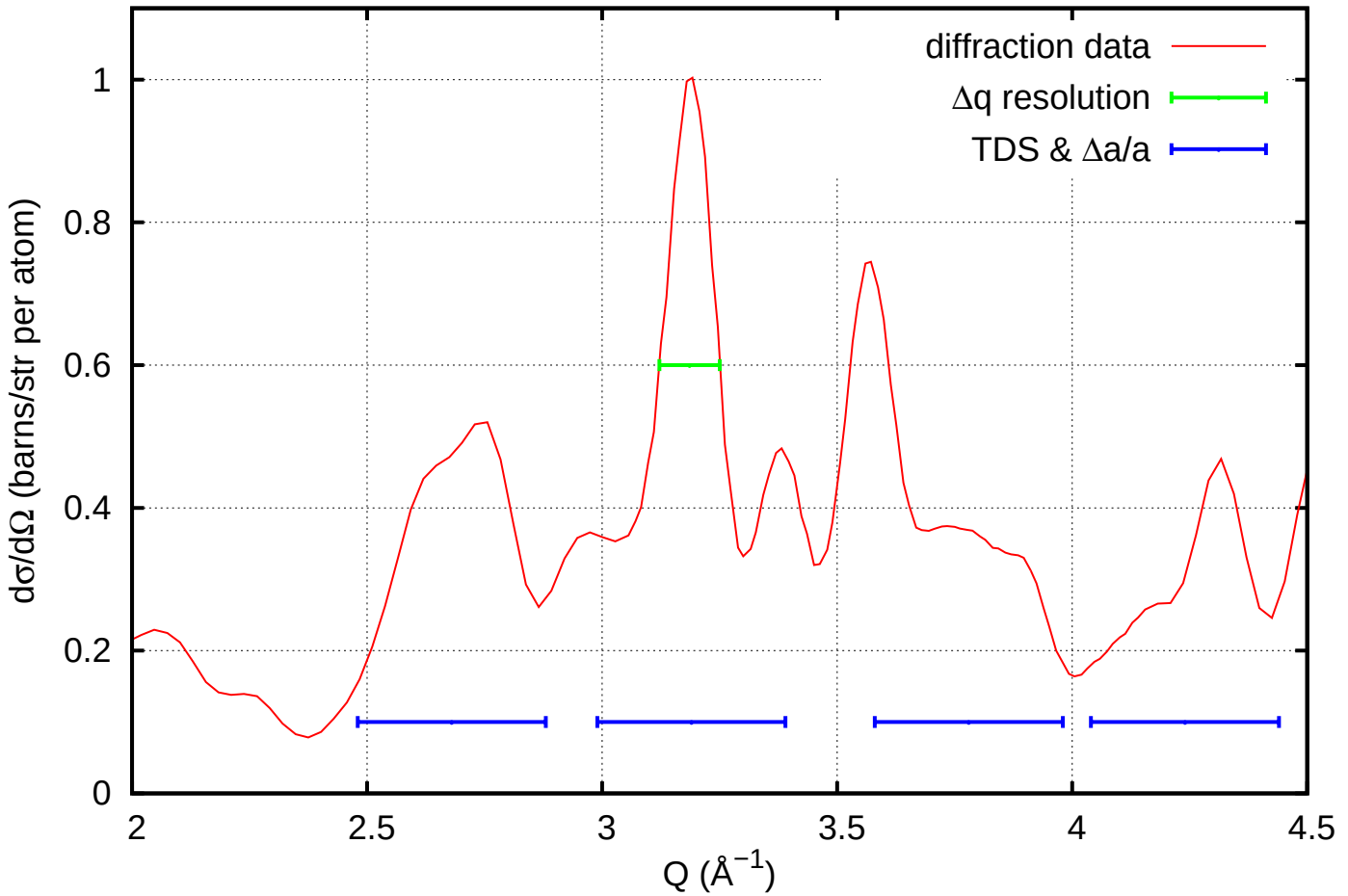

# *q*-space versus *r*-space representations of data

Fourier transform gives the total Pair-Distribution Function $\mathrm{PDF}(r)$ for an average atom at the origin $\Rightarrow$ peaks at all interatomic distances:

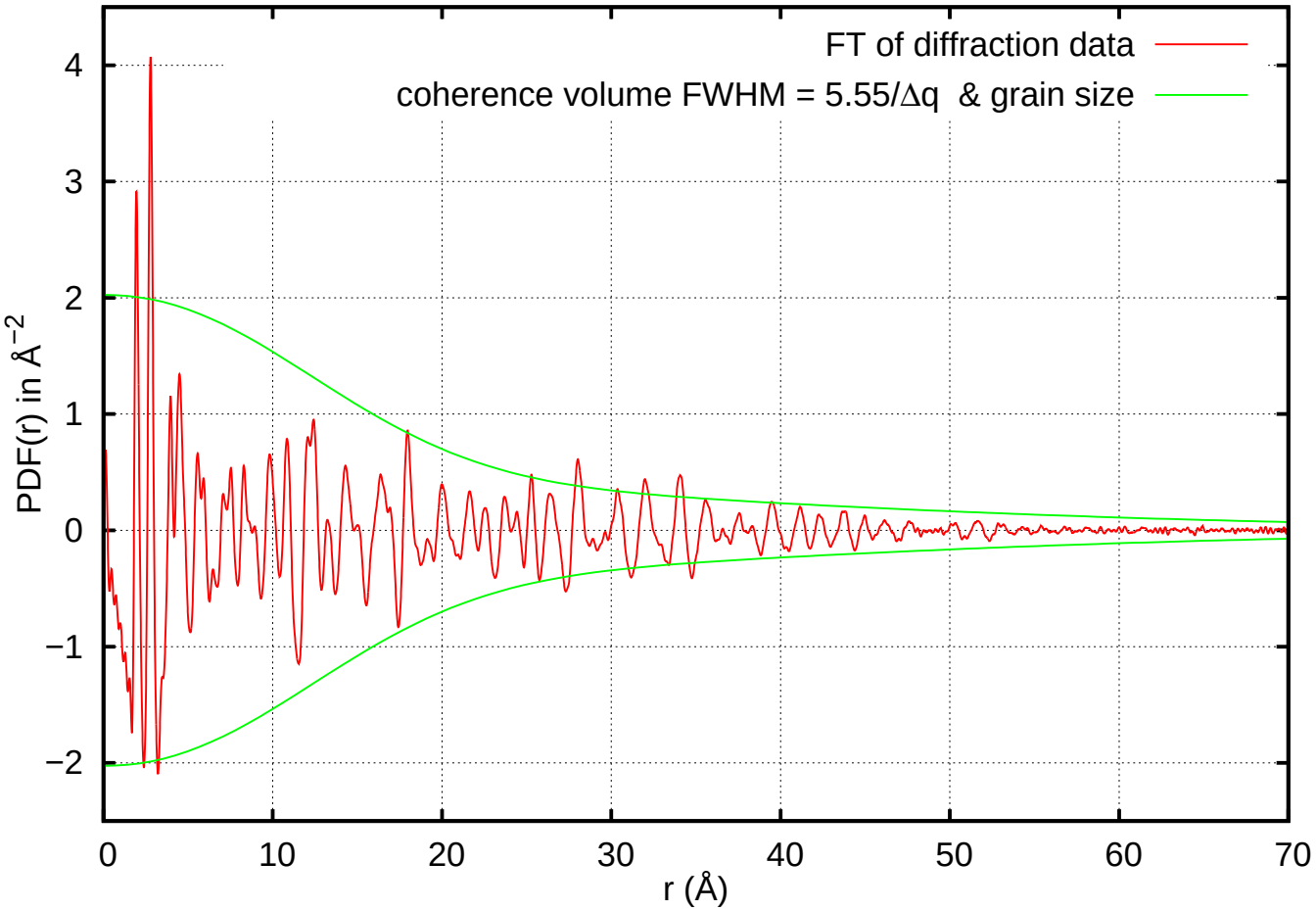


The *r*-range is limited by the grain size (*i.e.* the range of structural correlation) and by the coherence volume of the neutron that depends on the *q*-space resolution $\Delta q$.

# *q*-space versus *r*-space representations of data

The low-*r* slope of a properly normalized $\mathrm{PDF}(r)$ gives $\rho_0$, the peak areas are proportional to coordination number for atomic pairs, whose peak widths scale with their dynamic+static disorder plus the *r*-space resolution function $\Delta r(r) = \mathrm{sinc}(q_{\max} r) = \sin(q_{\max} r)/(q_{\max} r)$ that also leads to non-physical FT ripples or "wiggles" at low-*r*:

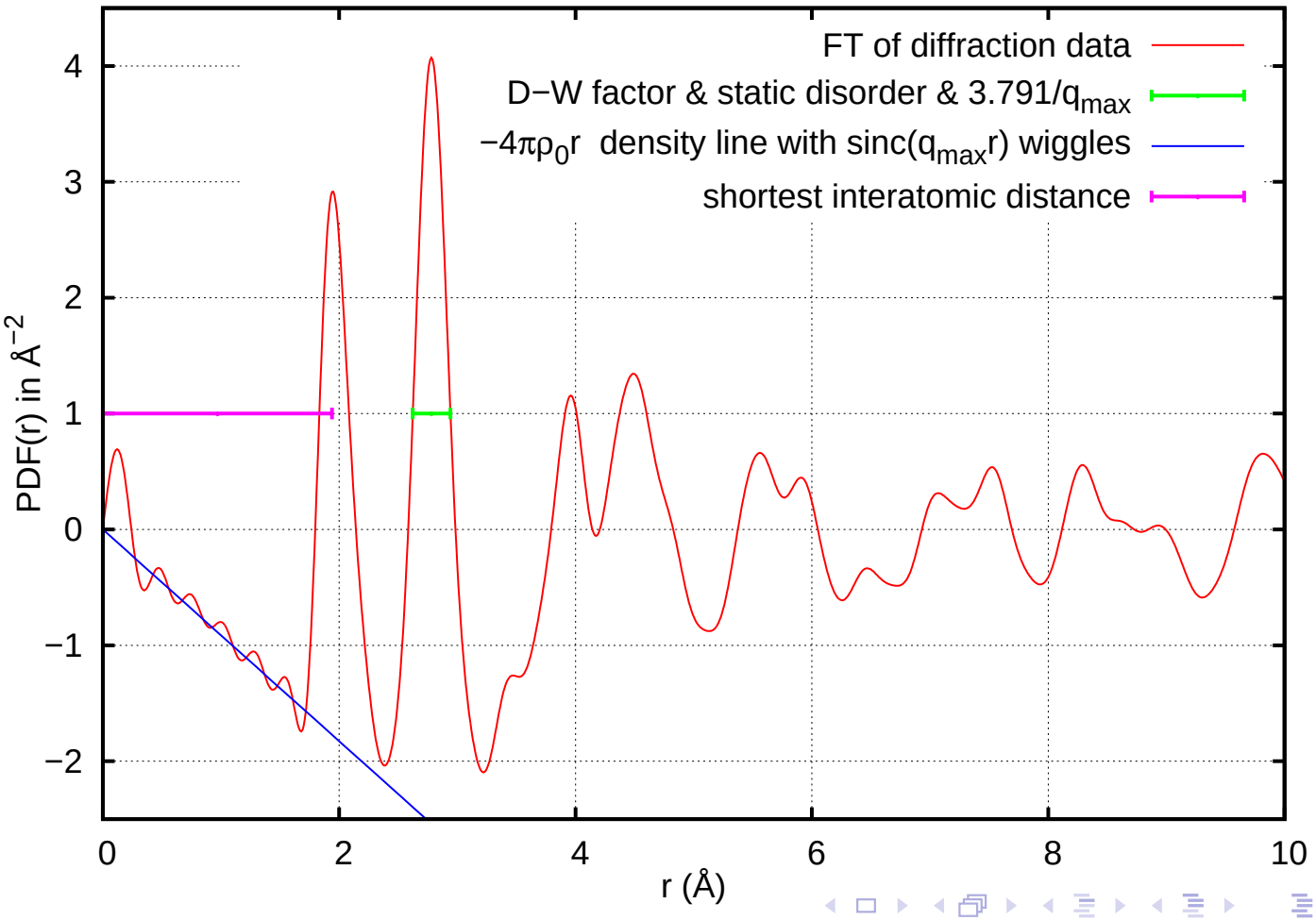

# The Debye-Waller factor revisited in *q*-space

The D-W factor is a (Gaussian-like) modulation of intensity in *q*-space, whose reduction of Bragg peak intensity at higher temperature is particularly noticeable when diffraction data are taken up to high-*q*:

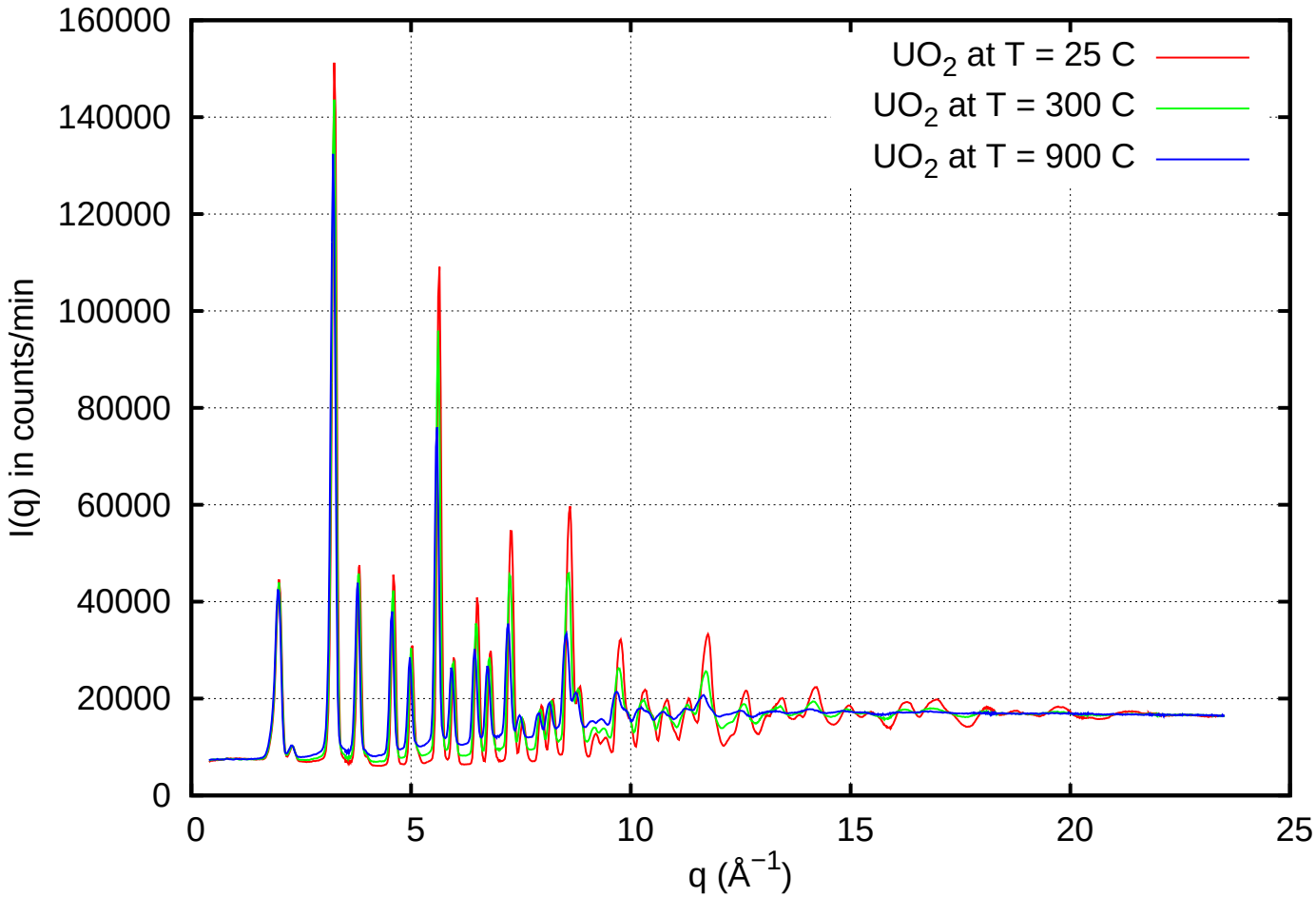


Such reduction in signal at “high harmonics” in *q* should, after Fourier transform, lead to broader features in *r*-space.

# The Debye-Waller factor in *r*-space

The convolution theorem states that a modulation in *q*-space leads to a convolution in *r*-space (and vice-versa), such that the the D-W factor broadens the peaks in $\mathrm{PDF}(r)$ according to the vibration amplitudes of the corresponding atomic pairs, while preserving the peak areas which are proportional to (generally constant) coordination number.

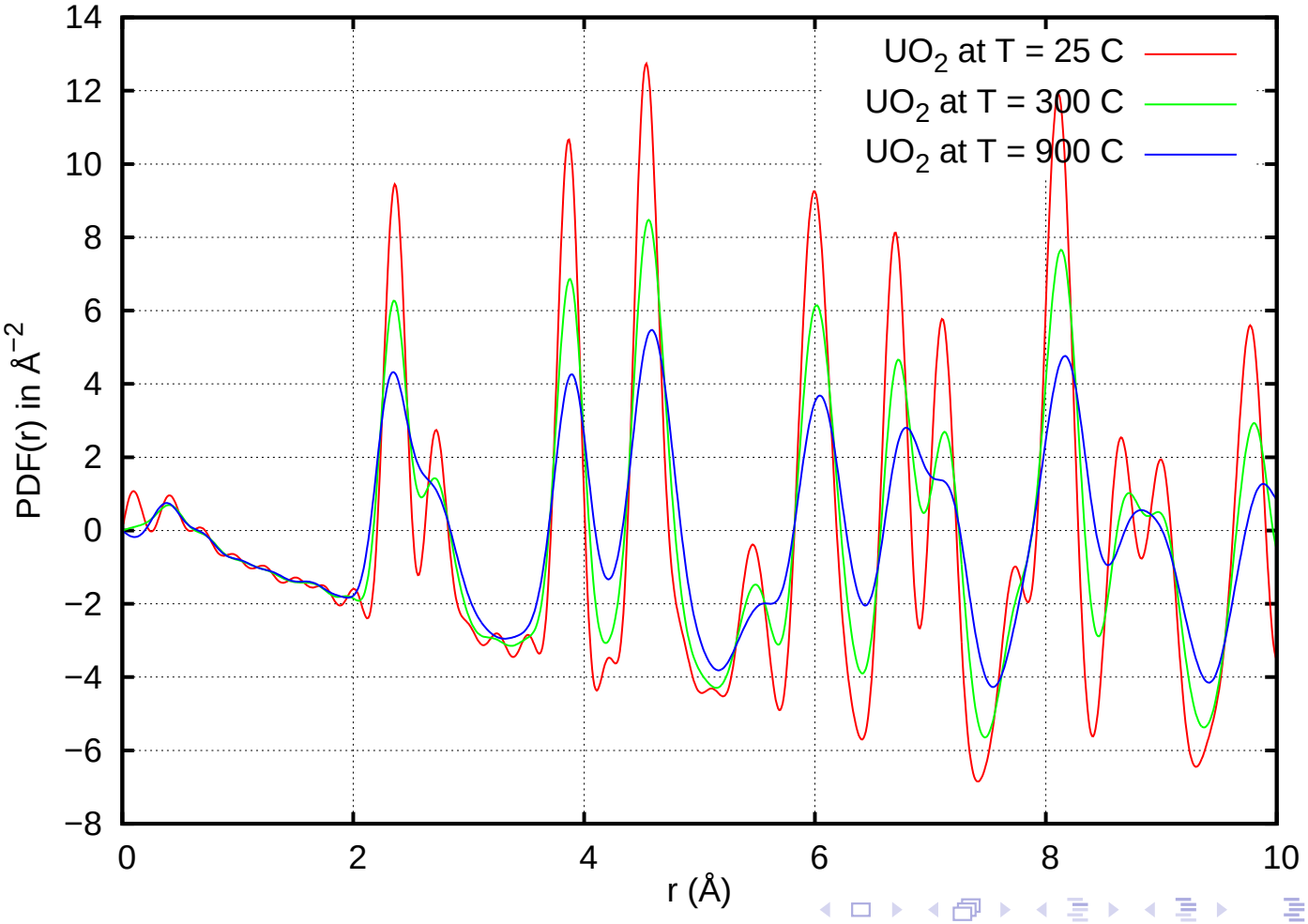

# Total scattering versus Bragg peak refinement

Refinement (*e.g.* Rietveld) of Bragg peak intensities ignores both the elastic ($\omega = 0$) diffuse scattering between peaks due to static disorder as well as the inelastic scattering due to dynamic disorder, and therefore provides only a space+time averaged picture of the sample's structure.

By comparison, making use of all the measured intensity $d\sigma/d\Omega$ in a "total scattering" data analysis provides (ensemble-averaged) information on the local quasi-instantaneous structure in the sample. *Recall that a liquid has no perfectly elastic scattering intensity.*

Neither can however distinguish between static and dynamic disorder, other than by looking at the temperature dependence. For example, the D-W factor amplitude extracted from fits to either Bragg peaks or $\mathrm{PDF}(r)$ should, when extrapolated to $T = 0$ K, be very small and correspond to zero-point motion when there is no static disorder.

One can also measure the elastic scattering intensity $S(q, \omega \sim 0)$ as a function of $T$ to see the onset of atomic motion at the time-scale of the scattered neutron's coherence time $\tau_{\mathrm{coh}} = \hbar/\delta E$, where $\delta E$ is the instrumental energy resolution. The FT of $S(q, \omega \sim 0)$ (*e.g.* measured at IN1-TAS) then produces a pair-distribution function $\mathrm{PDF}(r, t \to \infty)$ of time-averaged local structures, *i.e.* showing only static correlations.

# Combining Rietveld refinement and PDF-analysis

The space+time averaged picture obtained via Rietveld analysis of powder diffraction data is generally the most useful for determining the crystal structure of the sample, when this is not already known.

If the diffractometer has a high enough $q_{\max}$ (say 20 Å$^{-1}$), and all data corrections can be made for instrument background, sample attenuation, multiple scattering and inelasticity effects, then the same data can be used for PDF-analysis in order to probe local deviations (static or dynamic) away from the space+time averaged structure.

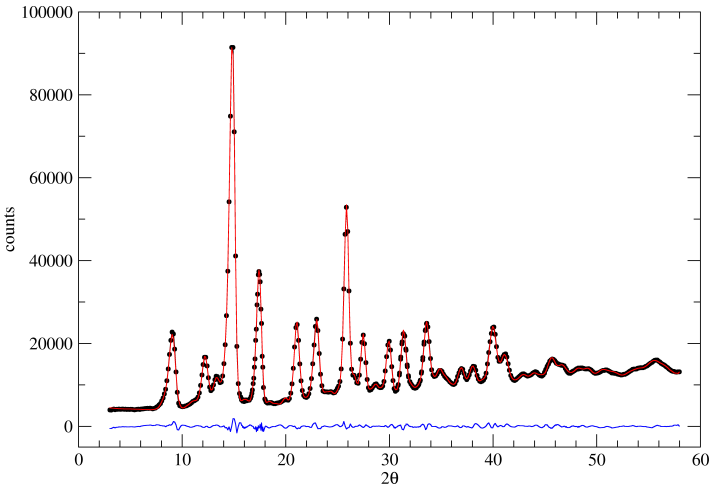


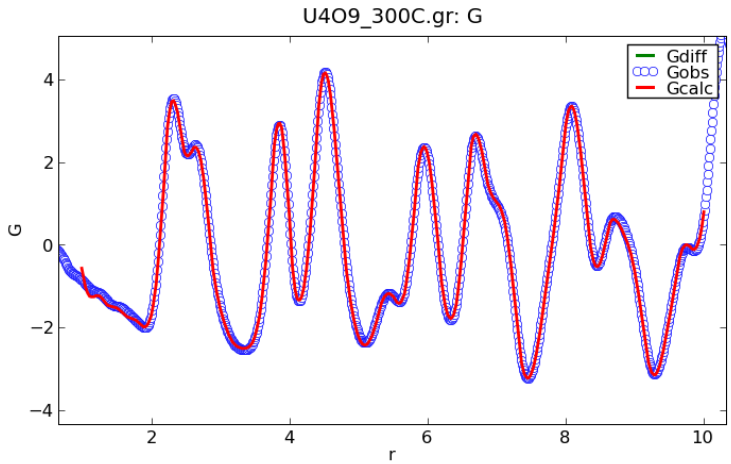


Above are $S(\mathbf{q})$ data acquired on the D4c diffractometer for disordered materials (ILL) using $\lambda = 0.5$ Å $\Rightarrow q_{\max} = 24$ Å$^{-1}$ that have been Rietveld refined in *q*-space (left) and whose $\mathrm{PDF}(r)$ after Fourier transform has been modelled with *PDFgui* software in *r*-space (right).

# Vibration modes seen by Rietveld vs PDF-analysis

Whereas Rietveld refinement gives time-averaged distances between atomic pairs, PDF-analysis sees an ensemble-average of quasi-instantaneous atomic positions and relative distances:

Correlated vibrations

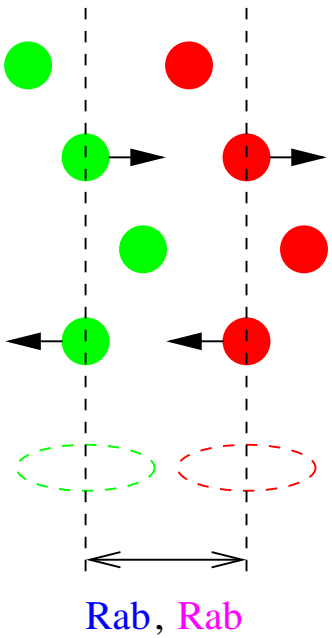


Anti−correlated vibrations

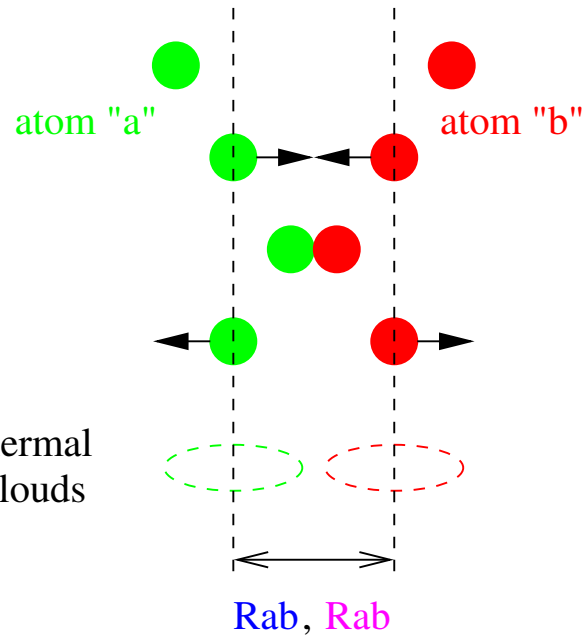


Libration mode

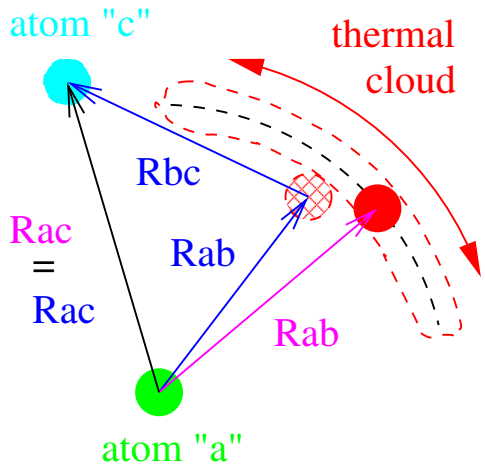


Rietveld−refined Rab = PDF−analysed Rab
for both correlated and anti−correlated vibrations, but Rietveld's time−averaged thermal clouds cannot distinguish between the two cases. PDF(r) will however show a broader peak for the a−b atomic pair in the anti−correlated case.

The time−averaged position of atom b is the barycenter of its banana−shaped thermal cloud, which is closer to atom a than any instantaneous position:

Rab (too short) < Rab (correct)

PDF(r) will show a sharp peak for the a−b and a−c atomic pairs but a very broad peak for b−c.

# Effect of correlated atomic vibrations at low-*r*

At short interatomic distances the peaks in $\mathrm{PDF}(r)$ are sharper and taller (conserving area $\propto$ coordination number) as compared to the neutron coherence volume's $\mathrm{FWHM} \sim 60$ Å for the D4c diffractometer:

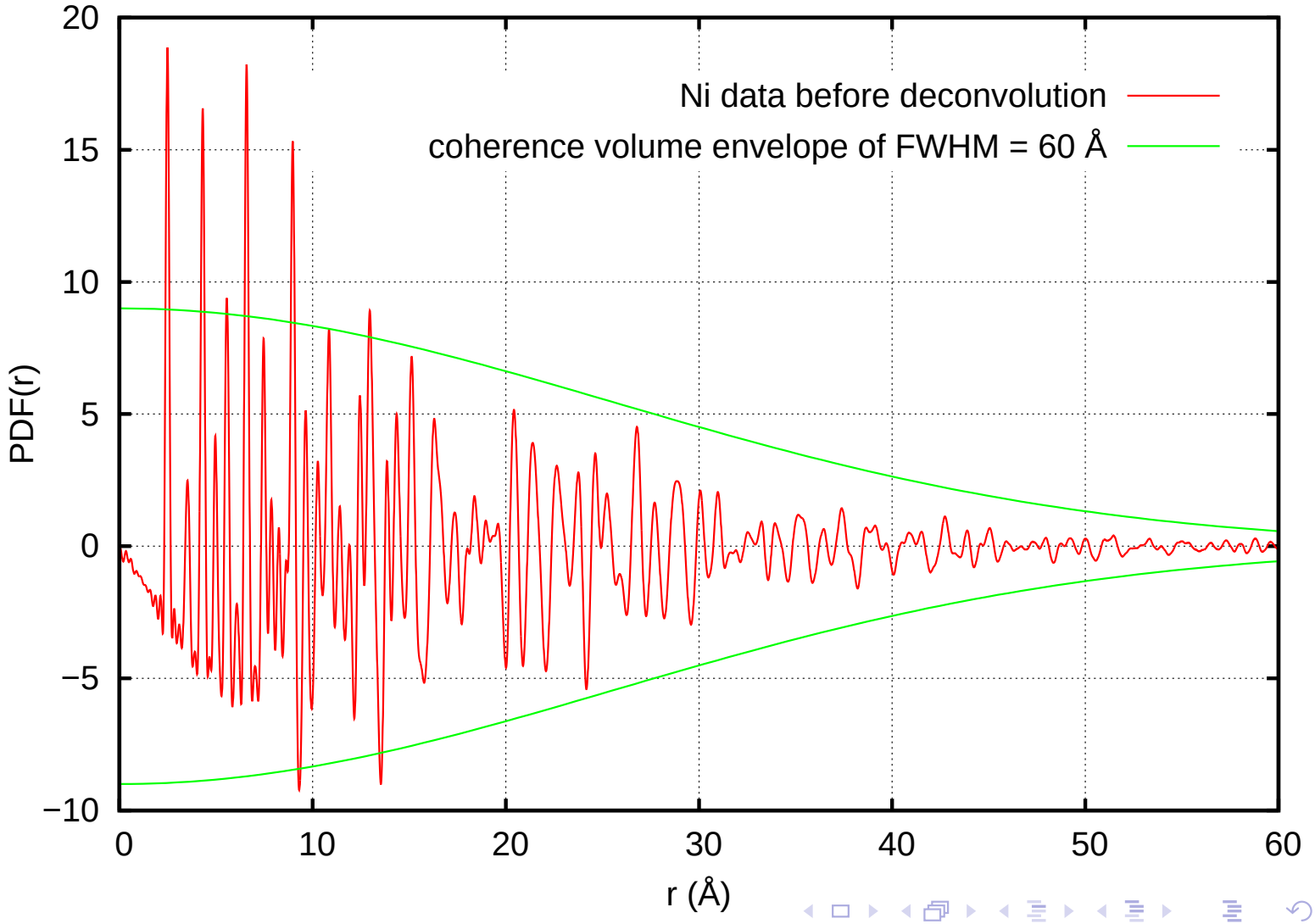

# The myth of "scattering power"

Since neutron scattering lengths $b_i$ are generally independent of $\lambda$, the measured intensity (counts/s) from an isotropic sample:

$$I(q) = \Phi \, \frac{d\sigma}{d\Omega}(q) \, d\Omega \,, \qquad \text{where} \quad q = (4\pi/\lambda) \, \sin(\theta) \,,$$

is a function of $q$ *only* and not of $\lambda$. Increasing $\lambda$ simply extends the same measured "peak" intensity $d\sigma/d\Omega(q)$ over a larger solid angle $\Omega$, leading to an increased *integrated* intensity for Bragg peaks.

For a *constant intrinsic* peak width $\Delta q$ (as determined by the sample's structure), a 1-D detector sees a corresponding intrinsic peak width in $2\theta$ given by simple differentiation: $\Delta(2\theta) = 2 \, (\Delta q/4\pi) \cdot \lambda/\cos(\theta) \,,$ so that the integrated peak intensity increases $\propto \lambda/\cos(\theta)$.

In fact, the (scattering power)·(Lorentz factor) is simply this factor:

$$\lambda^3/[\sin(\theta)\sin(2\theta)/2] = \lambda^3/[\sin^2(\theta)\cos(\theta)] = (4\pi/q)^2 \cdot \, \lambda/\cos(\theta) \,,$$

since $q$ for a Bragg peak remains constant as $\lambda$ is changed.

In powder diffraction however, the measured peak width in $2\theta$ is generally resolution-limited, so that an apparent increase in peak height (the so-called "scattering power") is observed.

# Early application of PDF-analysis: forms of carbon

## q-space:

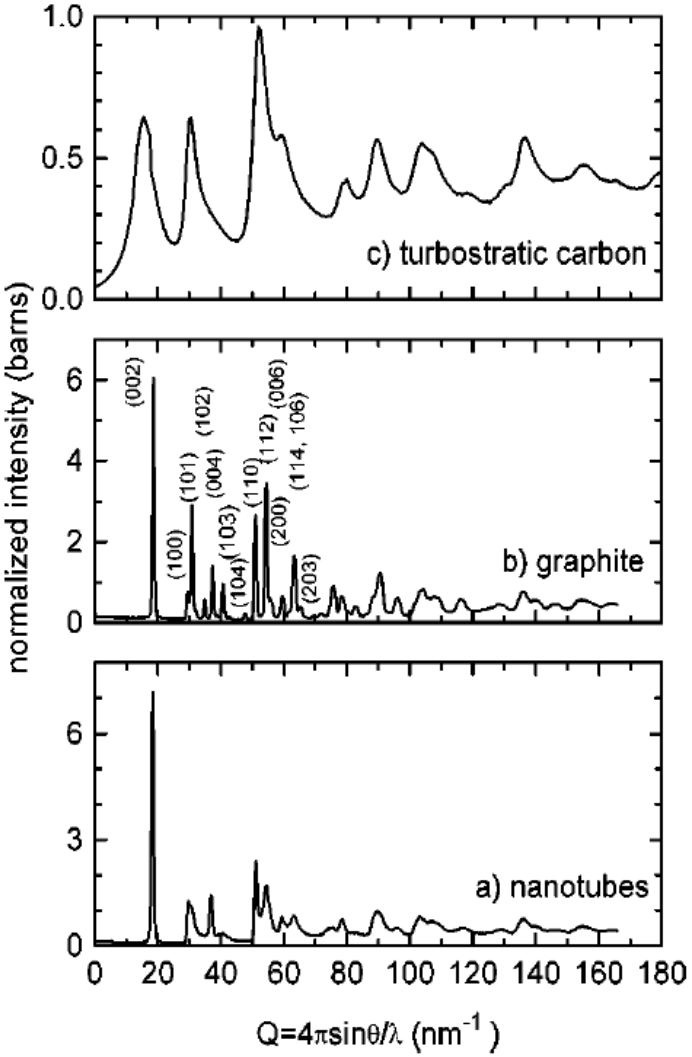


*A. Burian, J.C. Dore, H.E. Fischer and J. Sloan, Phys. Rev. B* **59** *(1999) 1665–8.*

# Early application of PDF-analysis: forms of carbon

**q-space:**

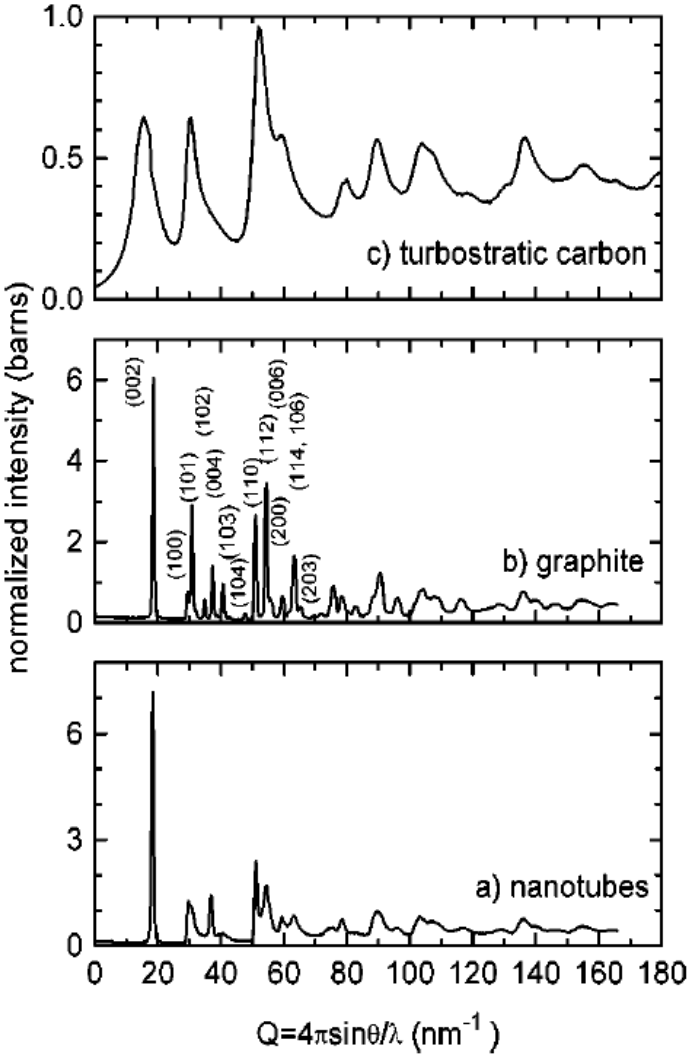


**r-space:**

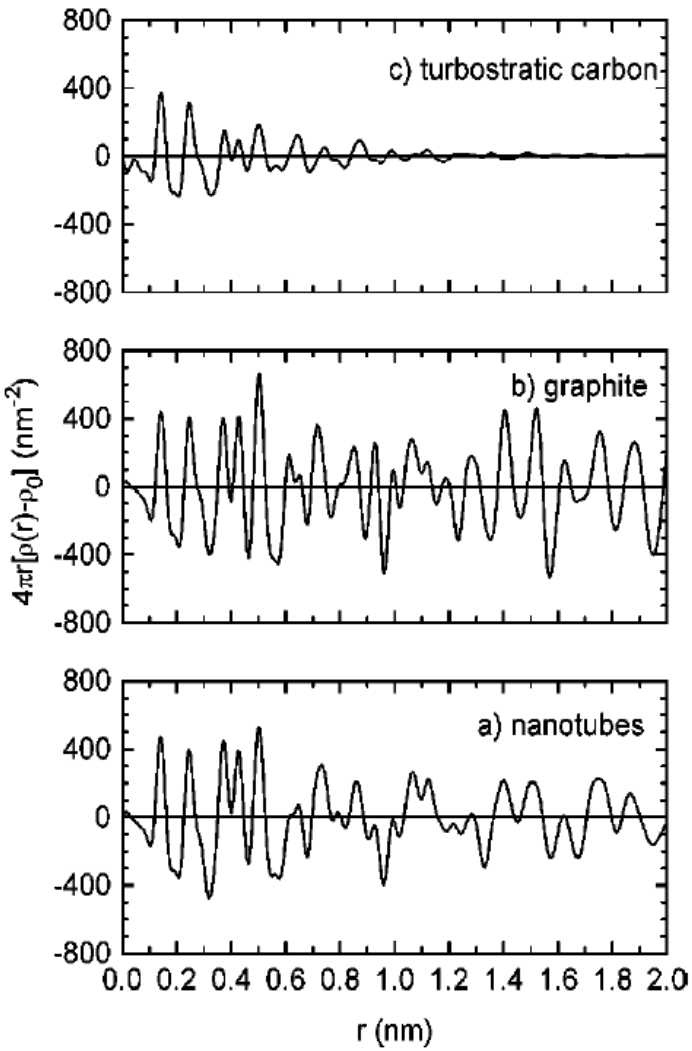


*A. Burian, J.C. Dore, H.E. Fischer and J. Sloan, Phys. Rev. B* **59** *(1999) 1665–8.*

# Local atomic strain in $ZnSe_{1-x}Te_x$

The **q**-space Bragg peak data (left) show no sign of local strain or static interatomic distance fluctuations, but only the expected shift (from top to bottom) in average lattice constant as the smaller Se atom replaces the larger Te. The $\mathrm{PDF}(r)$ data (right) show however that the intermediate stoichiometries have significant local disorder, and that there are two distinct distances for Se-Zn ($\sim$ 2.45 Å) and Te-Zn ($\sim$ 2.63 Å).

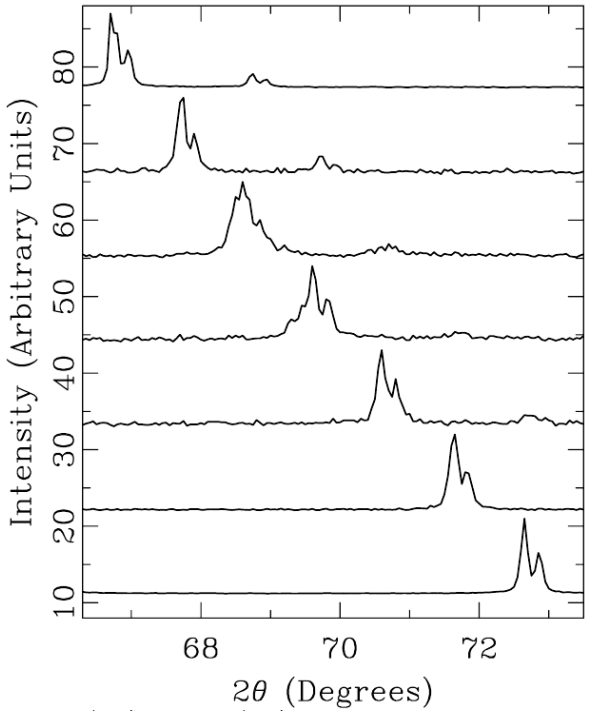


FIG. 1. $\langle 331 \rangle$ and weak $\langle 420 \rangle$ peaks of $ZnSe_{1-x}Te_x$ at (from top to bottom) $x = 1, \frac{5}{6}, \frac{4}{6}, \frac{3}{6}, \frac{2}{6}, \frac{1}{6}, 0$ measured at 300K using Cu rotating anode.

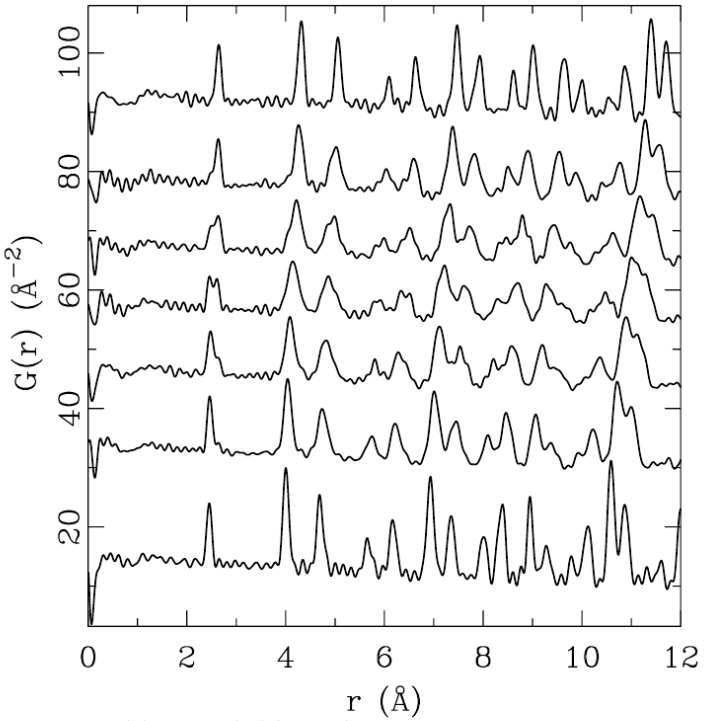


FIG. 3. $G(r) = 4\pi r(\rho(r) - \rho_0)$ for $ZnSe_{1-x}Te_x$ at (from top to bottom) $x = 1, \frac{5}{6}, \frac{4}{6}, \frac{3}{6}, \frac{2}{6}, \frac{1}{6}, 0$ measured at 10K.

*P.F. Peterson,* et al*, Phys. Rev. B* **63** *(2001) 165211.*

# Local structure in $BaTi_{1-x}Zr_xO_3$ relaxors

Bragg peak refinement shows that $BaTi_{1-x}Zr_xO_3$'s crystallographic structure is $ABO_3$ cubic perovskite for $x = 0$ and over the relaxor ferroelectric range ($0.25 \leq x \leq 0.5$) which includes the null-alloy composition $x = 0.32$. As charge disorder is minimized by the isovalent substitution $Ti^{4+}/Zr^{4+}$, it can be hypothesized that the long-range ferroelectric order is impeded by local structural distortions resulting from the large difference in the two cationic radii.

$\Rightarrow$ PDF-analysis using $\lambda = 0.5$ Å gave unambiguous evidence that the Ti and Zr atoms do not occupy equivalent octahedral sites as expected from the crystallographic structure, but rather the Ti atoms are displaced along [111].

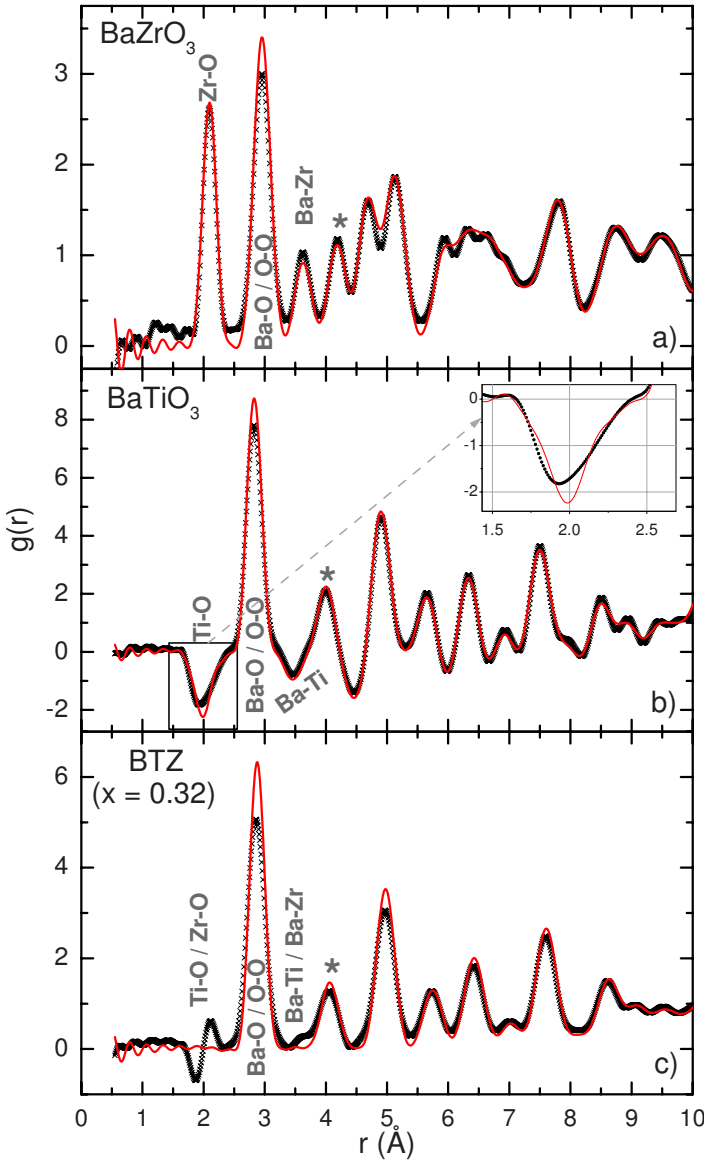


*C. Laulhé,* et al, *Phys. Rev. B* **79** *(2009) 064104.*

# Magnetic PDF-analysis

# Generalities about magnetic PDF-analysis

Recall that for a non-magnetic (monoatomic) system, the ordinary or "atomic" pair-distribution function is obtained by FT of the measured powder- or orientationally-averaged scattered intensity $S(q)$:

$$\mathrm{PDF}(r) \;=\; \frac{2}{\pi}\int_0^\infty q\,[S(q)-1]\,\sin(qr)\,dq \;=\; \frac{1}{N}\sum_{i\neq j}^{N}\frac{1}{r}\delta(r-r_{ij})$$

Similarly, for a system of magnetic spins of identical moments $S$:

$$\mathrm{mPDF}(r) = \mathrm{PDF}_{\mathrm{magn}}(r) \;=\; \frac{2}{\pi}\int_0^\infty q\,[S_{\mathrm{magn}}(q)-1]\,\sin(qr)\,dq$$

$$\approx\; f(r) = \frac{1}{N}\,\frac{3}{2S(S+1)}\sum_{i\neq j}^{N}\left\{\frac{A_{ij}}{r}\delta(r-r_{ij}) + B_{ij}\frac{r}{r_{ij}^3}[1-\Theta(r-r_{ij})]\right\}$$

where $\Theta(x)$ is the Heaviside step function, and $A_{ij}$ and $B_{ij}$ are spin-spin orientational correlation functions for spin components respectively perpendicular or parallel to $\mathbf{r}_{ij}$. Not shown above is that since the measured $S_{\mathrm{magn}}(q)$ is modulated by a magnetic form-factor (assumed isotropic), the peaks in $\mathrm{mPDF}(r)$ are correspondingly broadened to acquire widths greater than those of peaks in the atomic $\mathrm{PDF}(r)$.

# Generalities about magnetic PDF-analysis (cont'd)

For non-polarized neutron diffraction from 1 pair of F or AF magnetic spins, the $f(r) \approx \mathrm{mPDF}(r)$ indicates the "polar angle" between the spins' orientation and the vector $\mathbf{r}_{ij} = \mathbf{r}_i - \mathbf{r}_j$, notably by a slope at small $r$ that goes to zero when averaged isotropically over all such angles.

**ferromagnetic:**

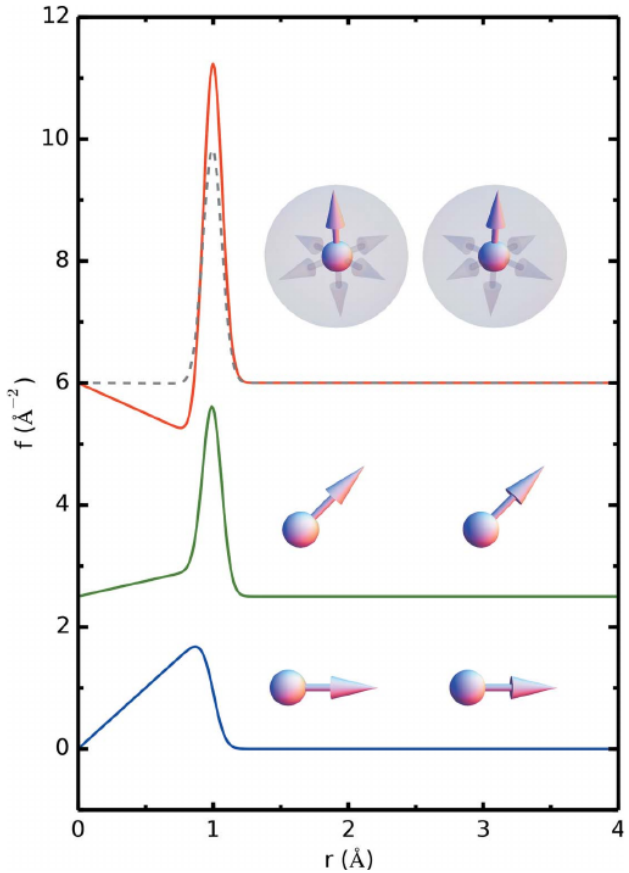


**anti-ferromagnetic:**

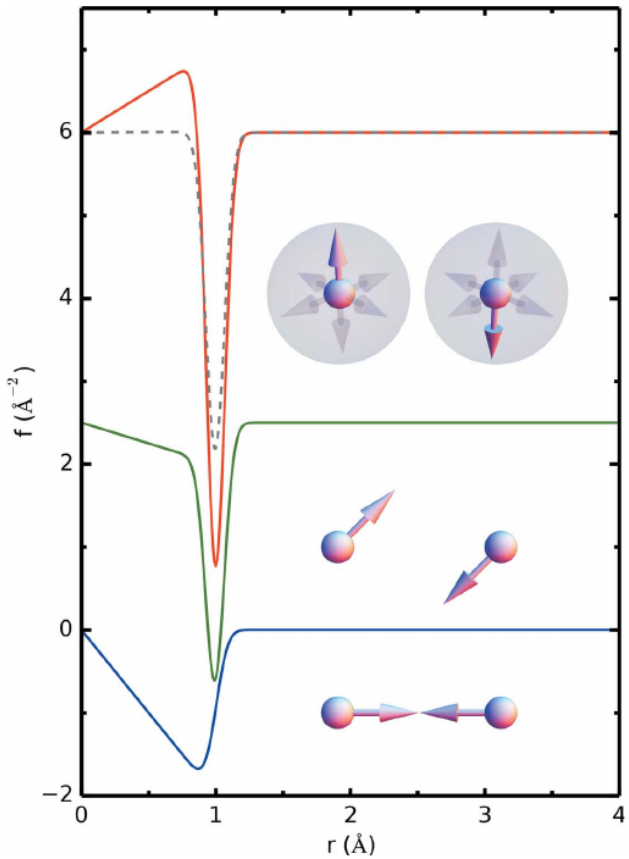


*B.A. Frandsen*, et al, *Acta. Cryst. A* **70** *(2014) 3–12.*

# Generalities about magnetic PDF-analysis (cont'd)

In a 3-D structure, parallel spins produce a positive peak in $\mathrm{mPDF}(r)$ at their relative *r*, and anti-parallel spins a negative peak, regardless of the "polar angle" whose value can generally be determined except in the case of rotational invariance imposed by cubic lattice symmetry.

**AF 1-D chain of spins:**

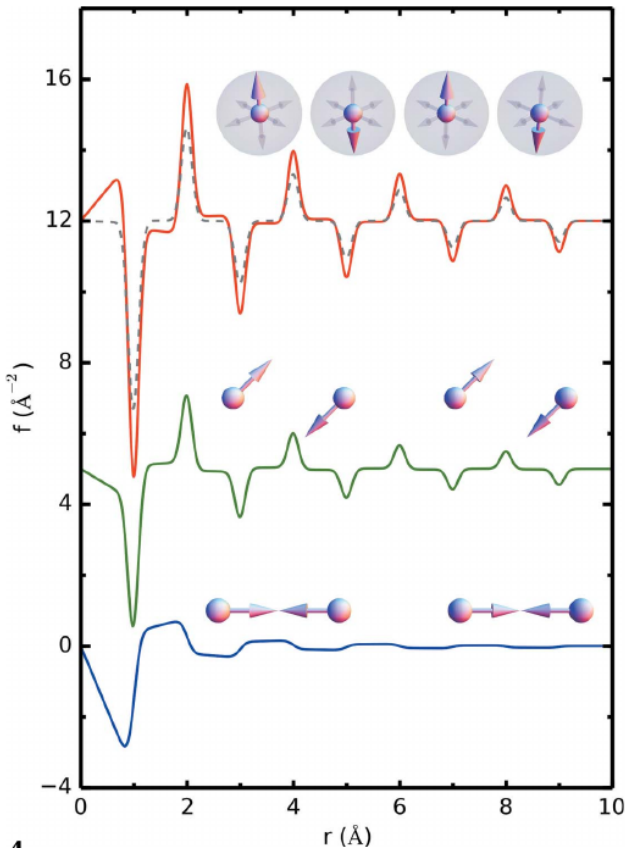


**AF 3-D cubic structure:**

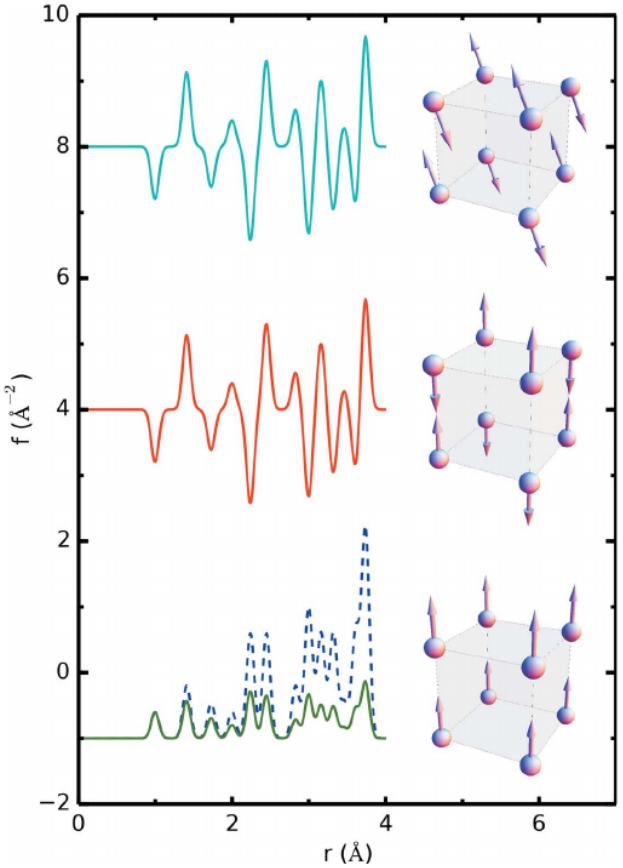


*B.A. Frandsen*, et al, *Acta. Cryst. A* **70** *(2014) 3–12.*

# Generalities about magnetic PDF-analysis (cont'd)

Q: Could magnetic PDF-analysis distinguish single-**k** from multiple-**k** structures, since it probes local (not average) spin configurations?

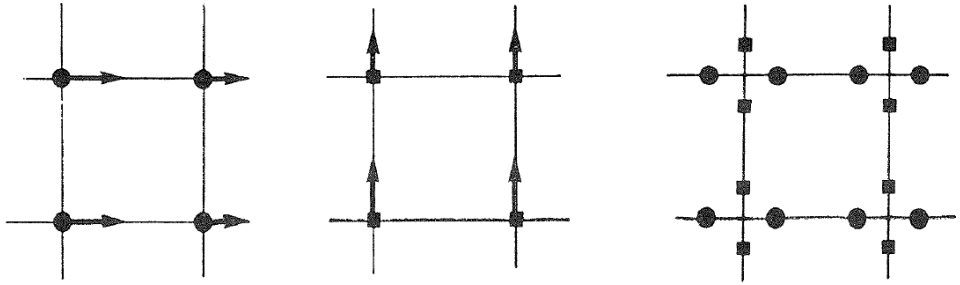


Figure V.8. — Illustration of the scattering due to 2 different single k domains (a) first domain, (b) second domain, (c) magnetic peaks in the reciprocal space.

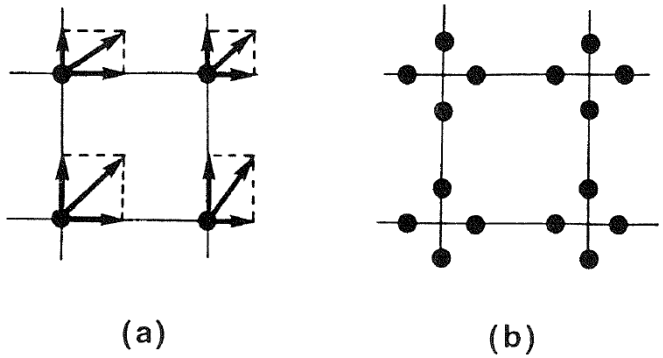


Figure V.9. — Illustration of a double k structure (a) the magnetic structure in the real space (b) the magnetic peaks in reciprocal space.

If converted to atomic displacement vectors, then YES. And Rietveld?

*(figures from J. Schweizer, Hercules book, volume II, chapter V)*

# Examples of magnetic PDF(r) data

## Short-range correlations in RE pyrochlore iridates *(E. Lefrançois,* et al*).*

One expects the frustrated spins of the RE and Ir tetrahedral sublattices to order in the all-in/all-out configuration at low $T$, but $Gd_2Ir_2O_7$ exhibits considerable magnetic diffuse scattering in $q$-space (D4@ILL data):

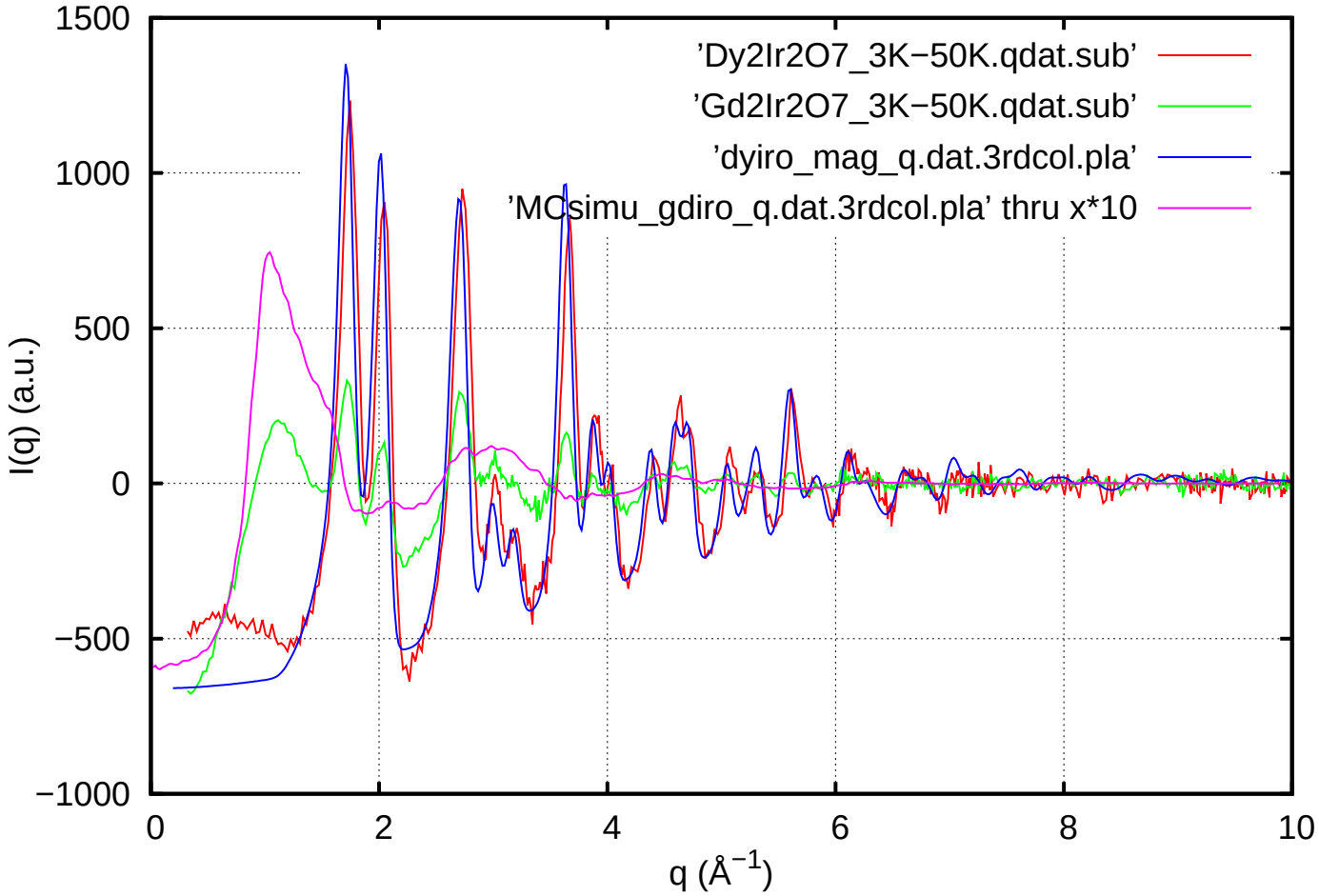

# Examples of magnetic PDF(r) data (cont'd)

## Short-range correlations in RE pyrochlore iridates *(E. Lefrançois,* et al*).*

Fourier transform produces a magnetic PDF($r$) for $Gd_2Ir_2O_7$ having a negative peak at about 3.6 Å, a clear sign of AF correlations between Ir/Gd–Ir/Gd pairs of atoms, which is confirmed by simulations:

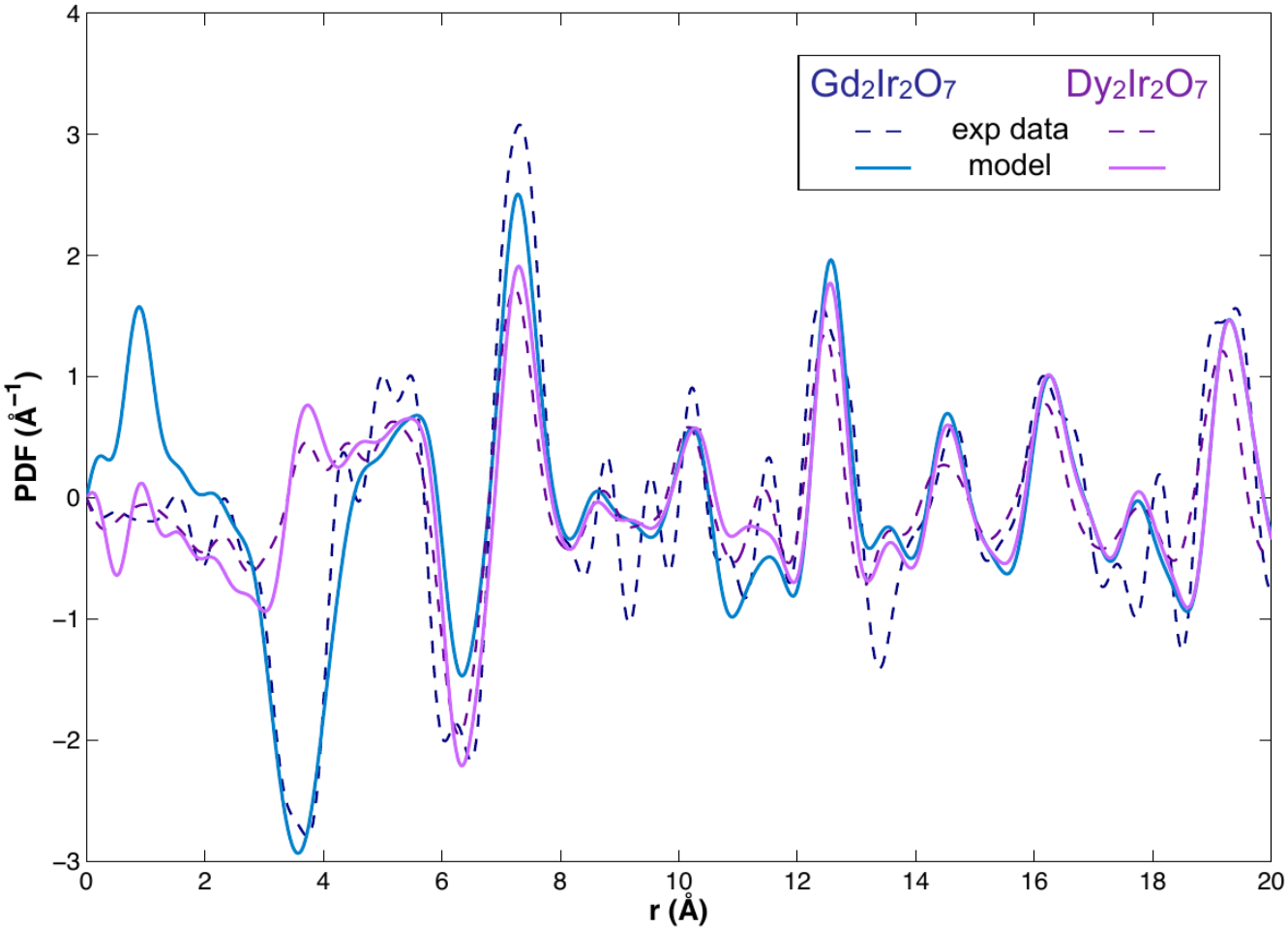

# Examples of magnetic PDF(r) data

## Paramagnetism in $UO_{2+x}$ at room temperature *(L. Desgranges,* et al*).*

The diffraction intensity from uncorrelated spins (*i.e.* paramagnetic) is roughly a Gaussian centered at $q = 0$ and, if not subtracted before FT, appears as a low-$r$ bump in the otherwise atomic/nuclear PDF($r$):

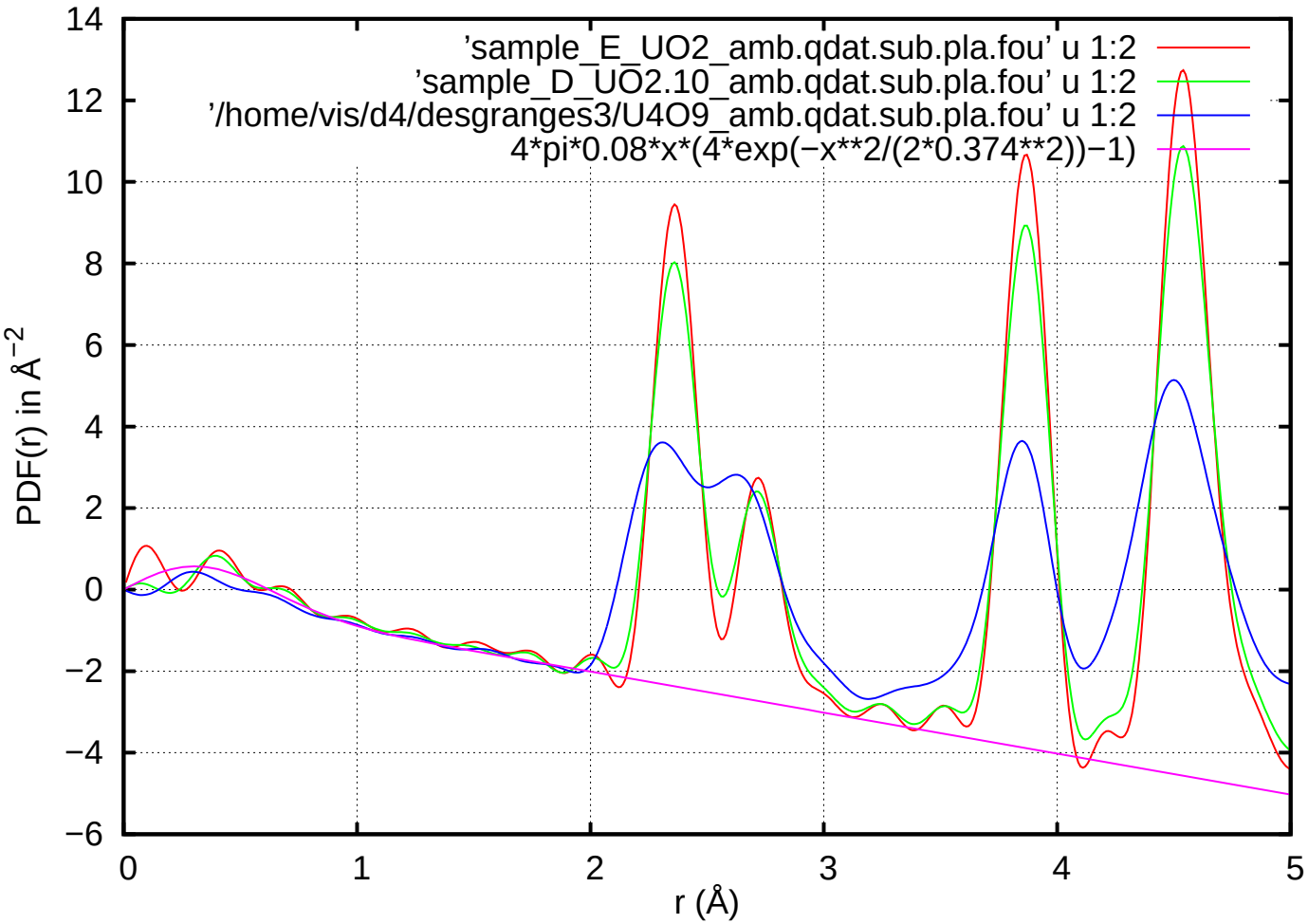

# Examples of magnetic PDF(r) data (cont'd)

## Paramagnetism in $UO_{2+x}$ at room temperature *(L. Desgranges,* et al*).*

Upon oxidizing from $U^{4+}$ in $UO_2$ to a mixture of $U^{4+}$ and $U^{5+}$ in $U_4O_9$ ($UO_{2.25}$), the U atom's average magnetic moment should decrease, thus reducing the paramagnetic bump amplitude in the PDF($r$):

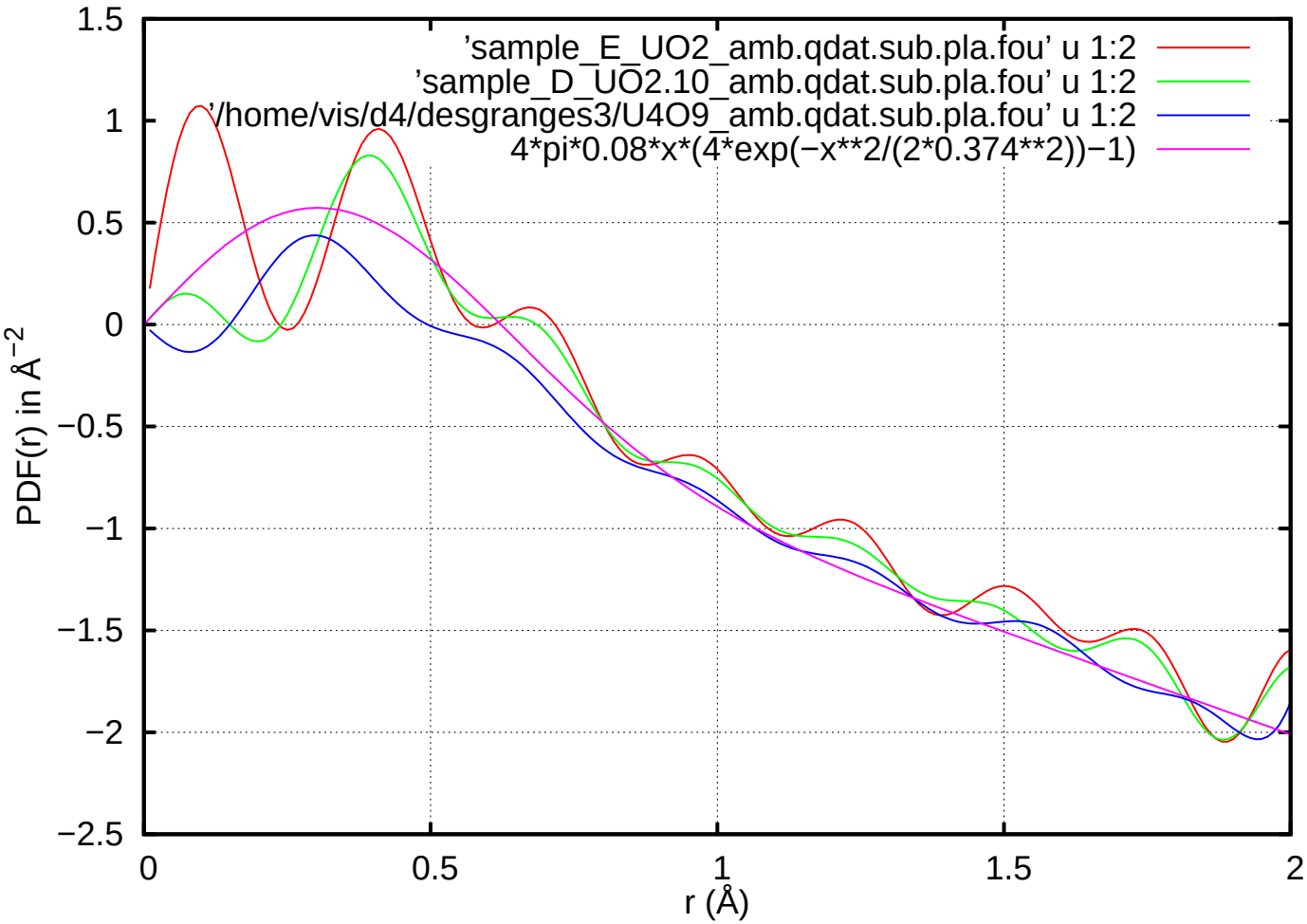

# Local atomic & magnetic structure in MnO

At 300K, MnO has the cubic rock-salt structure. An anti-ferromagnetic transition at $T_N = 118$ K is accompanied by a rhombohedral compression of the lattice along [111], resulting in R-3m symmetry:

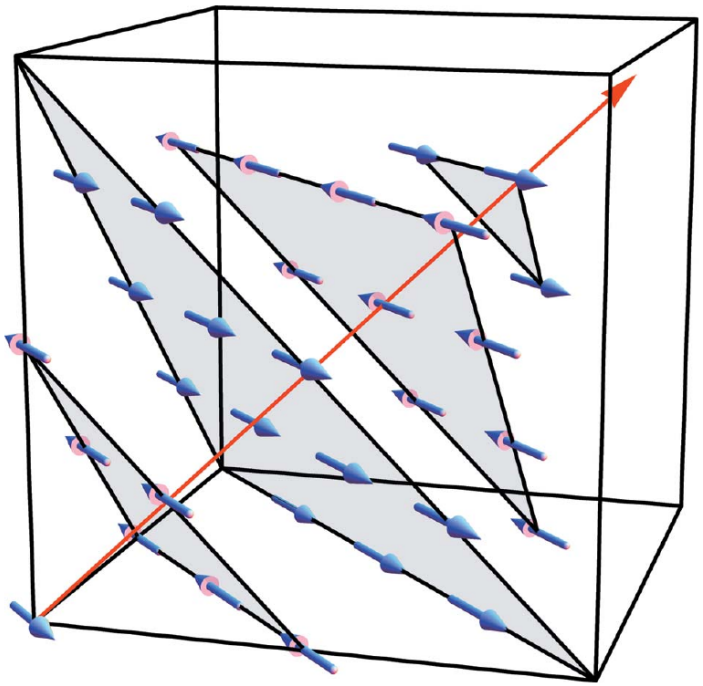

The spins of the $Mn^{2+}$ ions lying within common (111) planes align ferro-magnetically, with antiferromagnetic alignment between adjacent sheets along the [111] stacking direction, *i.e.* $\mathbf{k} = (1/2, 1/2, 1/2)$, resulting in the so-called type-II anti-ferromagnetic structure, but in principle such a spin arrangement is compatible only with monoclinic or lower symmetry!

High-resolution neutron powder diffraction found no deviation of the average (*i.e.* Rietveld-refined) structure from R-3m, in which case it cannot determine the absolute spin orientation within the (111) planes.

Large-box RMC fits to total-scattering (powder) data in *q*-space gave evidence for monoclinic C2 local symmetry in the atomic structure.

# Local atomic & magnetic structure in MnO (cont'd)

PDF-analysis of powder diffraction data (D20@ILL, NDPF@LANL) can reveal local deviations in atomic/nuclear and magnetic structures from the average structures as determined by Rietveld refinement:

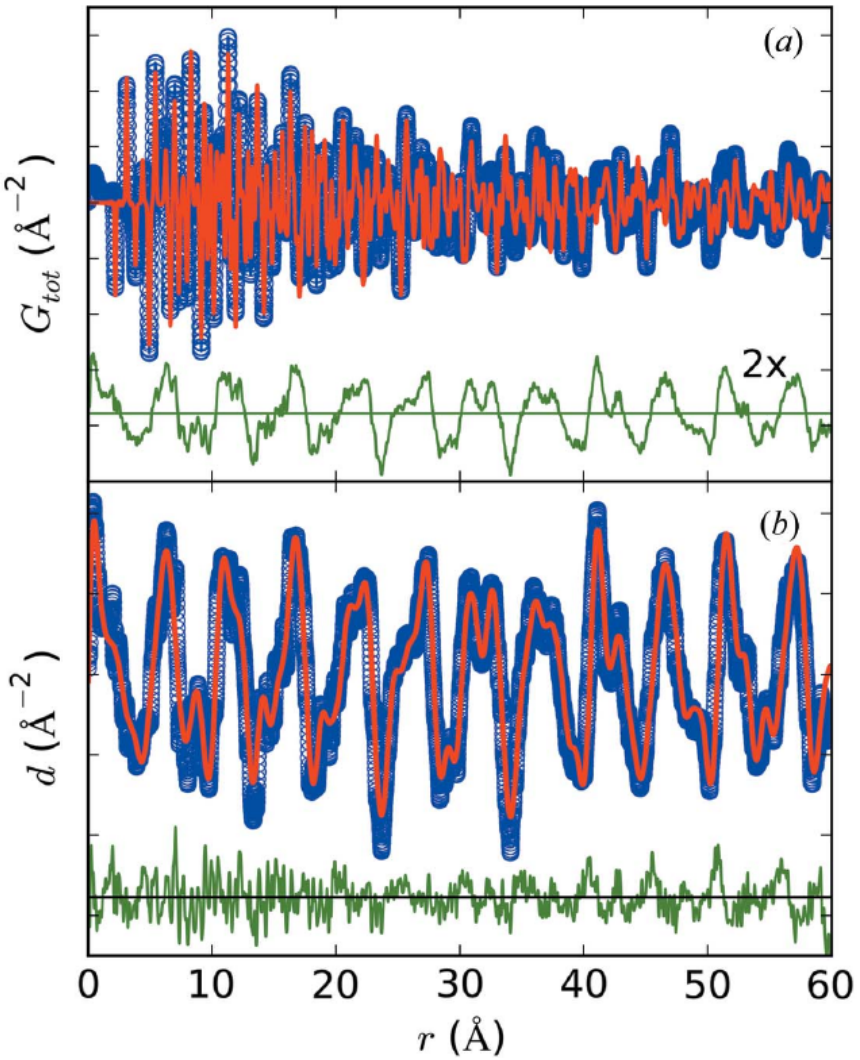


(a) The atomic PDF($r$) of a refined rhombohedral model (red) is subtracted from the total experimental PDF($r$) (blue) to reveal the magnetic PDF($r$) contribution (green). (b) Refinement of the resulting mPDF($r$) shows however some remaining discrepancies.

*B.A. Frandsen and S.J.L. Billinge, Acta. Cryst. A* **71** *(2015) 325–334.*

# Local atomic & magnetic structure in MnO (cont'd)

Fits to a monoclinic model of C2/m symmetry work better, also for the magnetic contribution, and indicate a preferred spin axis alignment along the pseudo-cubic $[10\bar{1}]$ direction (within the $(111)$ planes):

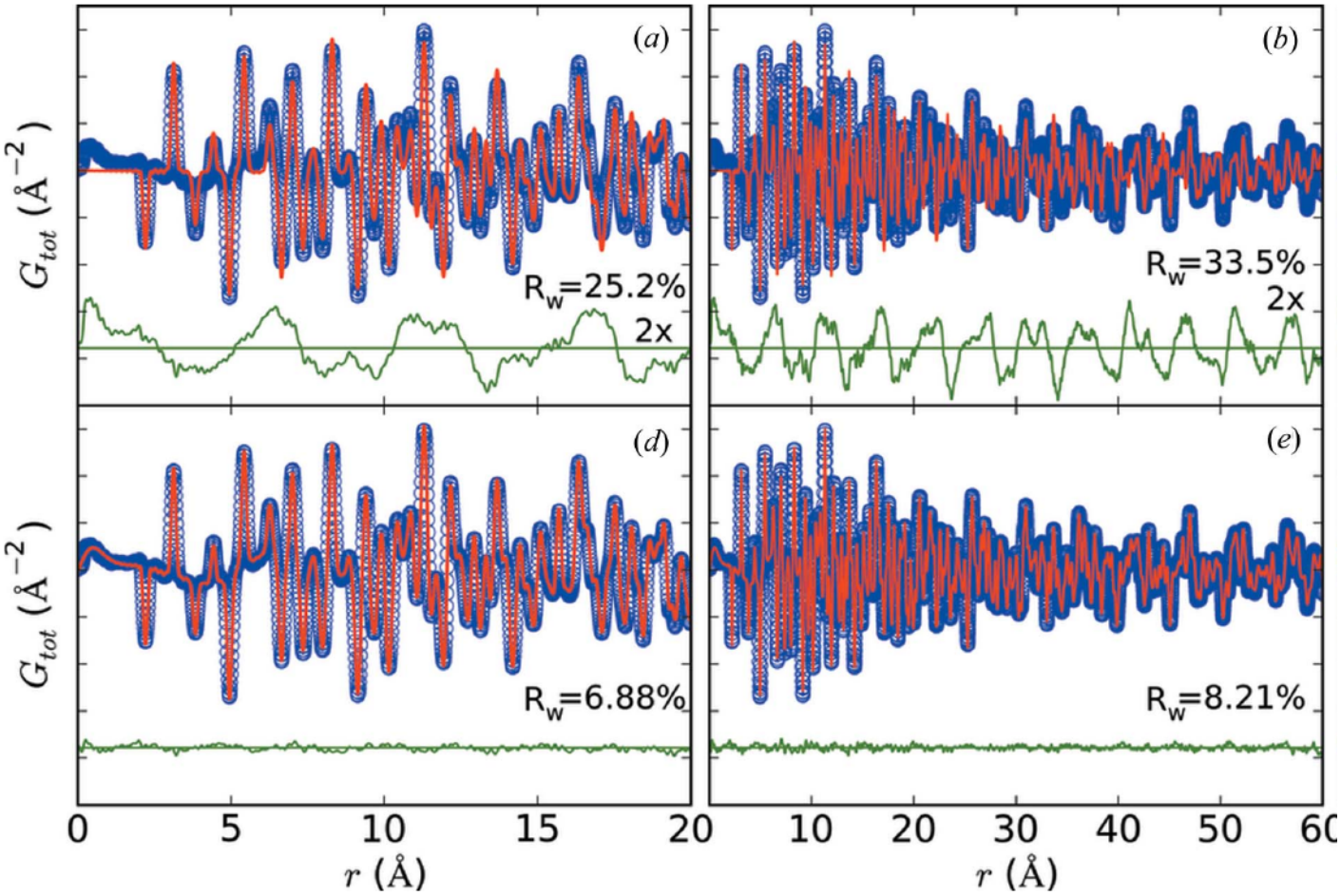


*B.A. Frandsen and S.J.L. Billinge, Acta. Cryst. A* **71** *(2015) 325–334.*

# Local atomic & magnetic structure in MnO (cont'd)

At low *r*, the monoclinic C2/m fit to nuclear and magnetic contributions is clearly better (*i.e.* lower $R_w$ factor) than the rhomohedral Rm-3 fit, confirming that the local structure has C2/m symmetry:

Refined parameters of combined atomic and magnetic PDF fits.

| Fitting range | 0–20 Å | 0–60 Å | 0–100 Å |
|---|---|---|---|
| $R\bar{3}m$ | | | |
| $R_w$ (%) | 7.20 | 8.30 | 10.55 |
| $a$ (Å) | 3.15025 (5) | 3.14948 (2) | 3.14922 (2) |
| $c$ (Å) | 7.5921 (3) | 7.5915 (1) | 7.5914 (1) |
| $C2/m$ | | | |
| $R_w$ (%) | 6.88 | 8.21 | 10.51 |
| $a$ (Å) | 5.4708 (9) | 5.4609 (4) | 5.4588 (6) |
| $b$ (Å) | 3.1429 (5) | 3.1460 (4) | 3.1466 (4) |
| $c$ (Å) | 15.1808 (1) | 15.1825 (2) | 15.1827 (1) |
| $\beta$ (°) | 89.895 (2) | 89.989 (3) | 90.004 (5) |

As the fitting range widens to higher *r*, the angle β and $a/b$ ratio of the monoclinic model approach the rhombohedral values of 90° and $\sqrt{3}$ respectively, and their $R_w$ values converge, implying that the local C2/m structure averages out to Rm-3 at a distance of about 100 Å.

*B.A. Frandsen and S.J.L. Billinge, Acta. Cryst. A* **71** *(2015) 325–334.*

# Local atomic & magnetic structure in $UO_2$

Currently the primary nuclear fuel, $UO_2$ is susceptible to further oxidation, generating a rich phase diagram for $UO_{2+x}$ at high $T$:

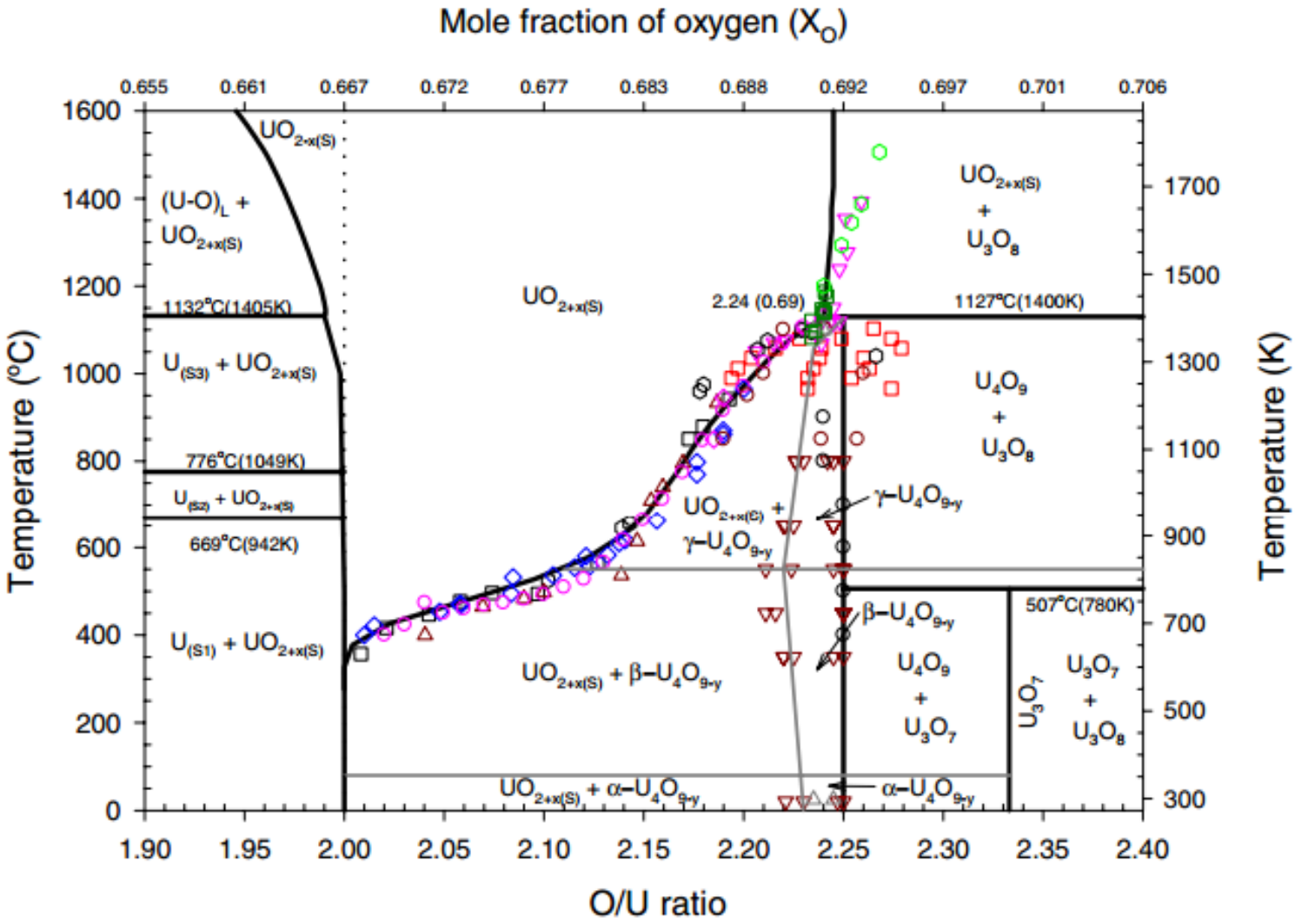

# Local atomic & magnetic structure in $UO_2$ (cont'd)

At 300 K, $UO_2$ has the cubic $CaF_2$ structure (space group Fm-3m). There are four U atoms per non-primitive cubic unit cell ($a = 5.47$ Å), and each U atom is surrounded by a cube of eight O atoms.

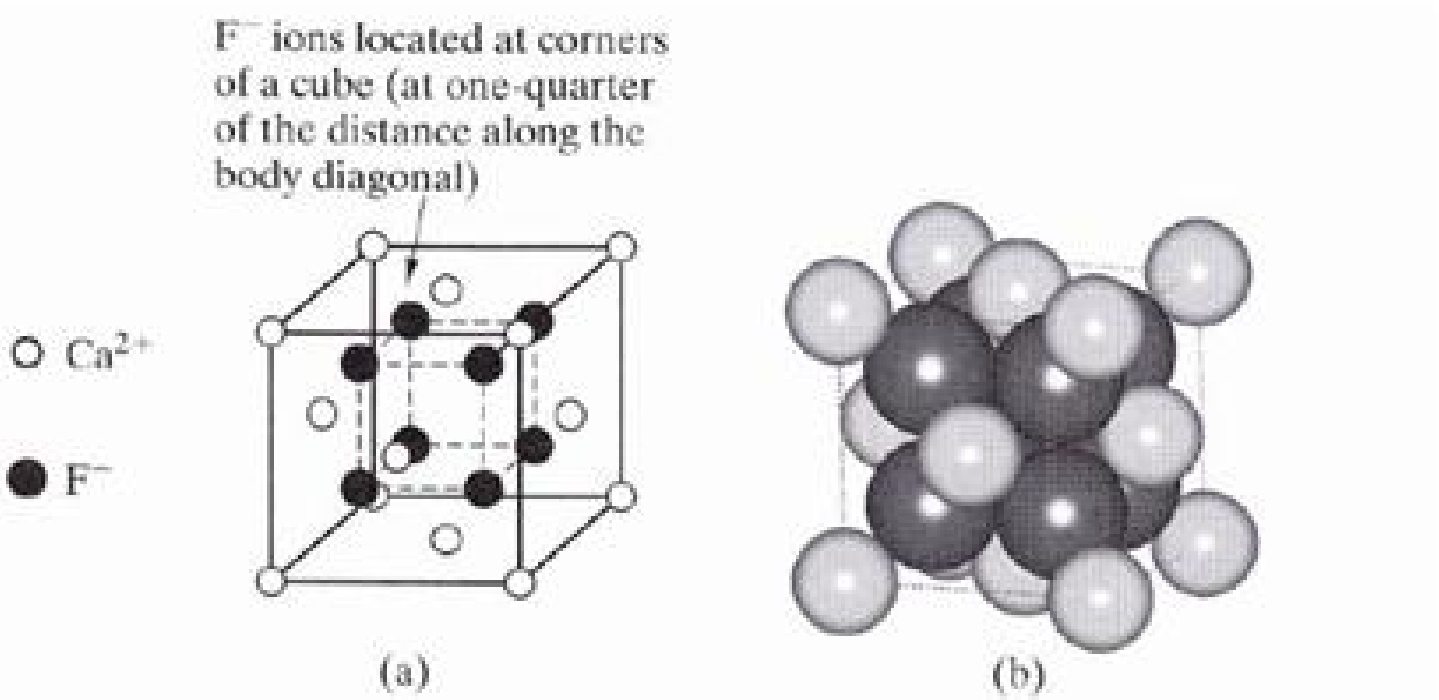


*Fluorite ($CaF_2$) unit cell showing (a) ion positions and (b) full-size ions.*

# Local atomic & magnetic structure in $UO_2$ (cont'd)

## Fm-3m space group: centrosymmetric, Patterson symmetry Fm-3m.

$Fm\bar{3}m$ $F\ 4/m\ \bar{3}\ 2/m$ $m\bar{3}m$ No. 225

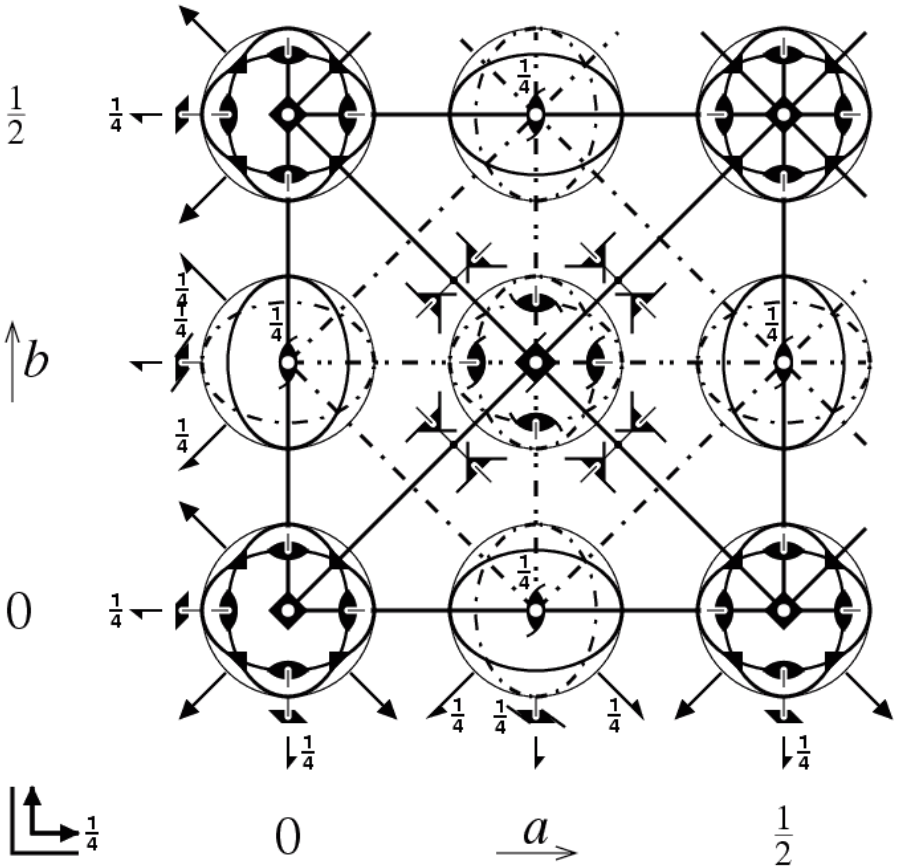


| | |
|---|---|
| 1 $x, y, z$ | 25 $\bar{x}, \bar{y}, \bar{z}$ |
| 2 $x, \bar{y}, \bar{z}$ | 26 $\bar{x}, y, z$ |
| 3 $\bar{x}, y, \bar{z}$ | 27 $x, \bar{y}, z$ |
| 4 $\bar{x}, \bar{y}, z$ | 28 $x, y, \bar{z}$ |
| 5 $z, x, y$ | 29 $\bar{z}, \bar{x}, \bar{y}$ |
| 6 $\bar{z}, \bar{x}, y$ | 30 $z, x, \bar{y}$ |
| 7 $z, \bar{x}, \bar{y}$ | 31 $\bar{z}, x, y$ |
| 8 $\bar{z}, x, \bar{y}$ | 32 $z, \bar{x}, y$ |
| 9 $y, z, x$ | 33 $\bar{y}, \bar{z}, \bar{x}$ |
| 10 $\bar{y}, z, \bar{x}$ | 34 $y, \bar{z}, x$ |
| 11 $\bar{y}, \bar{z}, x$ | 35 $y, z, \bar{x}$ |
| 12 $y, \bar{z}, \bar{x}$ | 36 $\bar{y}, z, x$ |
| 13 $x, \bar{z}, y$ | 37 $\bar{x}, z, \bar{y}$ |
| 14 $x, z, \bar{y}$ | 38 $\bar{x}, \bar{z}, y$ |
| 15 $\bar{x}, \bar{z}, \bar{y}$ | 39 $x, z, y$ |
| 16 $\bar{x}, z, y$ | 40 $x, \bar{z}, \bar{y}$ |
| 17 $z, y, \bar{x}$ | 41 $\bar{z}, \bar{y}, x$ |
| 18 $\bar{z}, y, x$ | 42 $z, \bar{y}, \bar{x}$ |
| 19 $\bar{z}, \bar{y}, \bar{x}$ | 43 $z, y, x$ |
| 20 $z, \bar{y}, x$ | 44 $\bar{z}, y, \bar{x}$ |
| 21 $\bar{y}, x, z$ | 45 $y, \bar{x}, \bar{z}$ |
| 22 $y, \bar{x}, z$ | 46 $\bar{y}, x, \bar{z}$ |
| 23 $\bar{y}, \bar{x}, \bar{z}$ | 47 $y, x, z$ |
| 24 $y, x, \bar{z}$ | 48 $\bar{y}, \bar{x}, z$ |

$+ (0,\frac{1}{2},\frac{1}{2}), (\frac{1}{2},0,\frac{1}{2}), (\frac{1}{2},\frac{1}{2},0)$

# Local atomic & magnetic structure in $UO_2$ (cont'd)

Upon cooling, $UO_2$ exhibits a first-order magnetic phase transition at $T_N = 30.8$ K which is accompanied by a static Jahn-Teller distortion that displaces the O atoms along $< 111 >$ directions. Both the magnetic structure and the structural distortions are 3**k** and have Pa-3 symmetry. The Pa-3 atomic structure for $UO_2$ is primitive cubic ($a = 5.47$ Å) with a center of symmetry at each U atom:

| | | | | |
|---|---|---|---|---|
| U Fm-3m | (0,0,0) | (1/2,0,0) | (0,1/2,0) | (0,0,1/2) |
| U Pa-3 | (0,0,0) | (1/2,0,0) | (0,1/2,0) | (0,0,1/2) |
| | | | | |
| O Fm-3m | (¼ ,¼ ,¼) | (¼, ¾, ¾) | (¾, ¾, ¼) | (¾, ¼ , ¾) |
| O Pa-3 | (¼+δ,¼+δ,¼+δ) | (¼-δ,¾-δ,¾+δ) | (¾-δ, ¾+δ,¼-δ) | (¾+δ,¼-δ, ¾-δ) |
| | | | | |
| O Fm-3m | (¾ , ¾ , ¾) | (¾, ¼ ,¼) | (¼ ,¼ ,¾) | (¼, ¾, ¼) |
| O Pa-3 | (¾-δ,¾-δ,¾-δ) | (¾+δ,¼+δ,¼-δ) | (¼+δ,¼-δ,¾+δ) | (¼-δ,¾+δ, ¼+δ) |

Table 1: atomic positions in $UO_2$ cell with Fm-3m symmetry compared to Pa-3 symmetry.

*L. Desgranges,* et al, *submitted to Inorganic Chemistry*.

# Local atomic & magnetic structure in $UO_2$ (cont'd)

## Pa-3 space group: centrosymmetric, Patterson symmetry Pm-3.

$Pa\bar{3}$ $P\,2_1/a\,\bar{3}$ $m\bar{3}$ No. 205

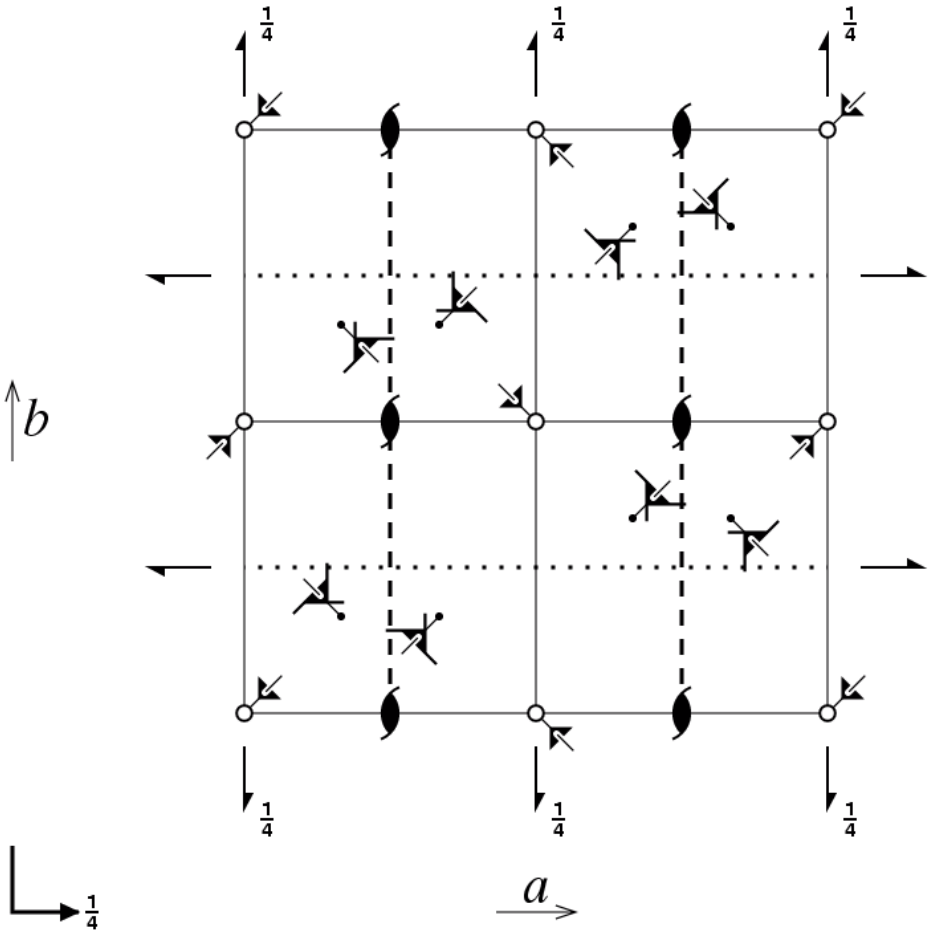


1 $x, y, z$
2 $\frac{1}{2}+x, \frac{1}{2}-y, \bar{z}$
3 $\bar{x}, \frac{1}{2}+y, \frac{1}{2}-z$
4 $\frac{1}{2}-x, \bar{y}, \frac{1}{2}+z$
5 $z, x, y$
6 $\frac{1}{2}-z, \bar{x}, \frac{1}{2}+y$
7 $\frac{1}{2}+z, \frac{1}{2}-x, \bar{y}$
8 $\bar{z}, \frac{1}{2}+x, \frac{1}{2}-y$
9 $y, z, x$
10 $\bar{y}, \frac{1}{2}+z, \frac{1}{2}-x$
11 $\frac{1}{2}-y, \bar{z}, \frac{1}{2}+x$
12 $\frac{1}{2}+y, \frac{1}{2}-z, \bar{x}$
13 $\bar{x}, \bar{y}, \bar{z}$
14 $\frac{1}{2}-x, \frac{1}{2}+y, z$
15 $x, \frac{1}{2}-y, \frac{1}{2}+z$
16 $\frac{1}{2}+x, y, \frac{1}{2}-z$
17 $\bar{z}, \bar{x}, \bar{y}$
18 $\frac{1}{2}+z, x, \frac{1}{2}-y$
19 $\frac{1}{2}-z, \frac{1}{2}+x, y$
20 $z, \frac{1}{2}-x, \frac{1}{2}+y$
21 $\bar{y}, \bar{z}, \bar{x}$
22 $y, \frac{1}{2}-z, \frac{1}{2}+x$
23 $\frac{1}{2}+y, z, \frac{1}{2}-x$
24 $\frac{1}{2}-y, \frac{1}{2}+z, x$

# Local atomic & magnetic structure in $UO_2$ (cont'd)

Correct magnetic structure proposed by Burlet et al. in 1986:

Type I, 3-k transverse structure
<001> propagation vector,
$\mu_0 = 1.74\ \mu_B$

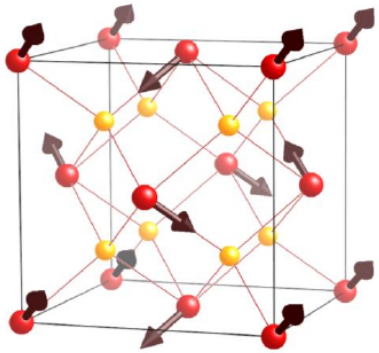

$$\vec{\mu}_n \propto \sum_{j=1}^{j=3} \vec{m}_{k_j} \exp(i\,\vec{k}_j.\vec{R}_n)$$

$\vec{k}_1 = (1, 0, 0)$ etc.

A: $\vec{m}_{100} = (0, 1, 0)$ etc.

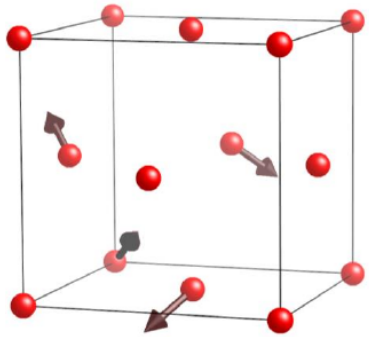

B: $\vec{m}_{100} = (0, 0, 1)$ etc.

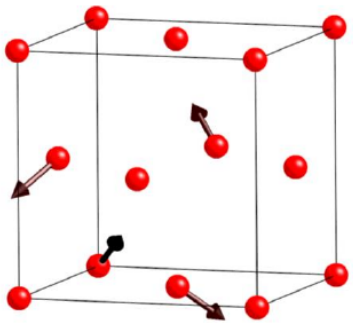

Joint Research Centre

*(slide courtesy of R. Caciuffo)*

# Local atomic & magnetic structure in $UO_2$ (cont'd)

What could otherwise have been a 1**k** type-I anti-ferromagnetic structure of transverse polarization, *i.e.* $\mathbf{k} =< 0\ 0\ 1 >$, was shown by Faber and Lander (1976) to be at least 2**k** (and therefore non-collinear) in order to couple via the order parameter to O atom displacements evidenced by single-crystal neutron diffraction. Burlet (1986) then showed from the $T$-dependence of magnetic intensities in an applied field that both the atomic and magnetic structures were 3**k** below $T_N = 30.8$ K.

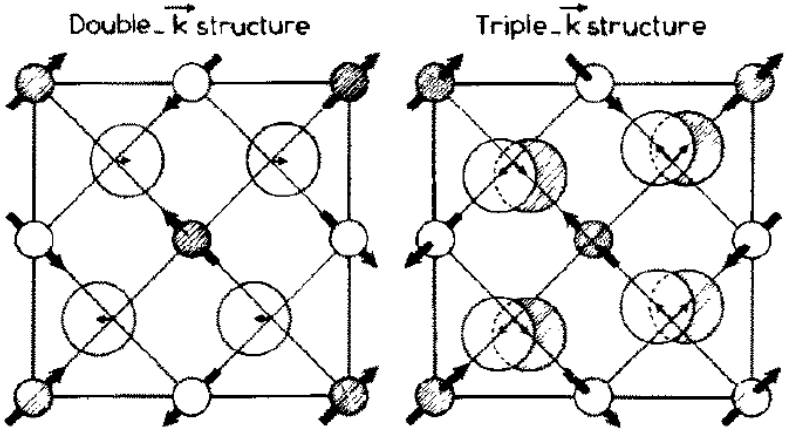


**Fig. 11. The (001) projection of the fluorite structure to display the double-*k* and the triple-*k* structures which are possible in $UO_2$. The hatched and open small circles represent uranium atoms at $z = 0$ and $z = 1/2$, respectively. The hatched and open large circles represent oxygen atoms at $z = -\frac{1}{4}$ and $z = \frac{1}{4}$ displaced from the ideal fluorite lattice. In the double-*k* structure the displacements are along ⟨100⟩, whereas in the triple-*k* structure they occur along ⟨111⟩; broken and full arrows represent down and up displacements. In a double-*k* structure the magnetic moments lie along ⟨110⟩ whereas in a triple-*k* structure they are along ⟨111⟩.**

# Local atomic & magnetic structure in $UO_2$ (cont'd)

PDF($r$) data (D4@ILL) for $UO_2$ at 1273 K were fitted to Fm-3m (top) and Pa-3 (bottom) models. The black lines indicate the J-T distortion along $< 111 >$ directions, *i.e.* for a 3**k** propagation vector:

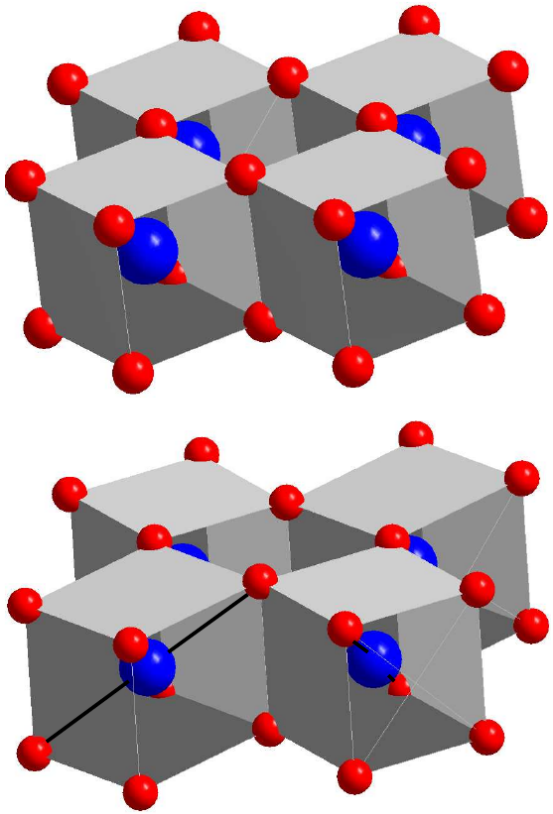

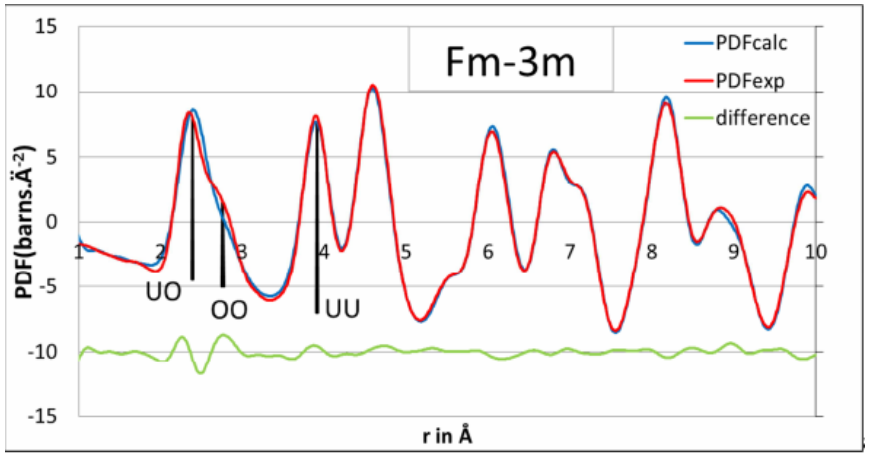


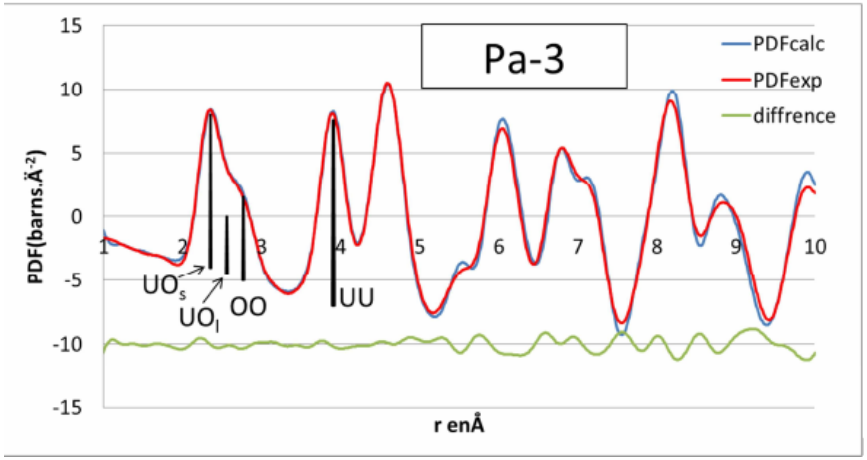


$\Rightarrow$ Local structure is Pa-3, averaging out to Fm-3m after $\sim$ 2 unit cells.

*L. Desgranges,* et al*, submitted to Inorganic Chemistry*.

# Local atomic & magnetic structure in $UO_2$ (cont'd)

$\Rightarrow$ Minimum Pa-3 domain sizes of about $2 \times 2 \times 2$ unit cells or $\phi \sim 15$ Å (note that there are 4 possible orientations for a Pa-3 cubic unit cell).

NB: applying Fm-3m symmetry operators to a Pa-3 unit cell of $UO_2$ indeed produces a $4 \times 4 \times 4$ supercell having Fm-3m symmetry.

A linear extrapolation of the PDF-fitted *T*-dependence of the long and short UO distances (red and black curves) suggests that the Jahn-Teller distortion persists down to 0 K and would thus include a static component. The blue curve shows the single time+space averaged UO distance from Fm-3m Rietveld refinement of the same diffraction data:

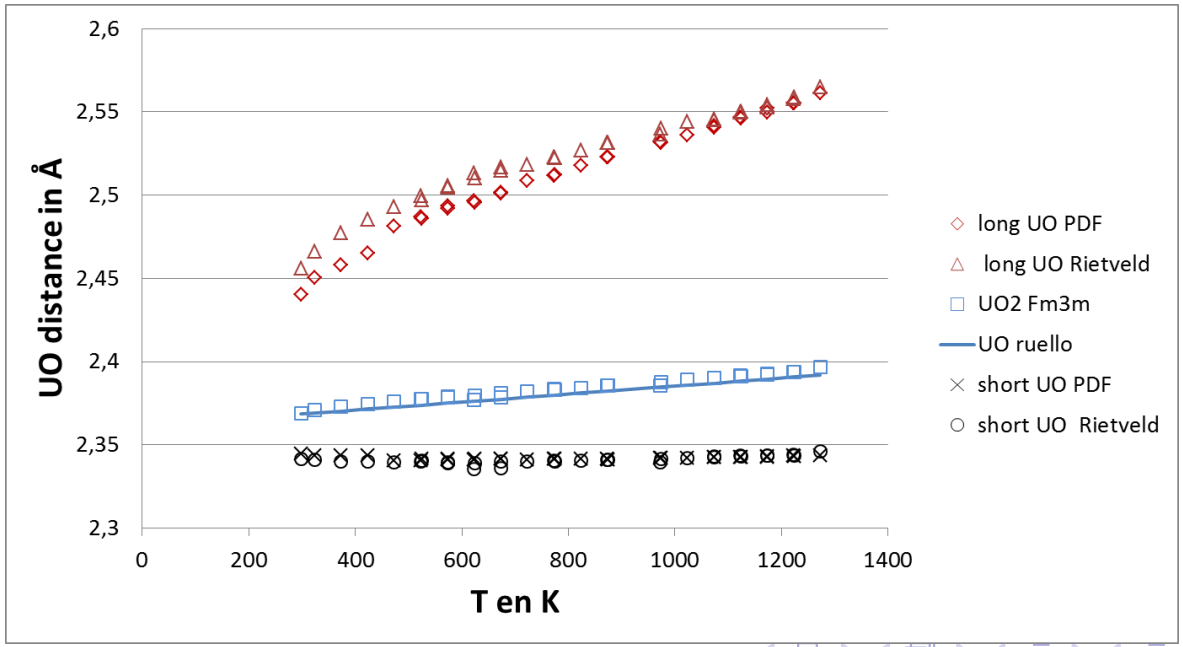

# Local atomic & magnetic structure in $UO_2$ (cont'd)

The problem is that for $T > T_N$ there is evidence from TAS-INS with polarization analysis (IN20@ILL) for uncorrelated dynamical Jahn-Teller distortions of 1**k** along $< 100 >$, rather than "our" 3**k** along $< 111 >$:

dependence of the energy-integrated dynamic susceptibility. Above $T_N$, a magnetic inelastic response consisting of two dispersive peaks was observed between 3 and 10 meV. This signal was easily measurable even at 200 K, more than six times the Néel temperature, where spatial correlations between the uranium spins are essentially zero. We assume this result as evidence that in the time scale of our experiment the uranium triplet ground state is split into three singlets, due to a dynamical Jahn-Teller (JT) distortion of the oxygen cage which reduces the point symmetry at the uranium site. Since the position of the peaks and their dispersion are compatible to a 1-**k** distortion along the $\langle 100 \rangle$ direction, a picture emerges in which local, uncorrelated 1-**k** dynamical JT distortions occur above $T_N$ along the three directions of the $\langle 100 \rangle$ star; as $T_N$ is approached, a correlation builds up between the phases of the corresponding vibrations until, eventually, a static 3-**k** structure is obtained below $T_N$. [S0163-1829(99)09621-6]

*R. Caciuffo,* et al*, Phys. Rev. B* **59** *(1999) 13892.*

The *relative phases* of dynamical superposed orthogonal 1**k** displacements of O atoms determines the total displacement direction and thus affects the *widths* of O-O and O-U peaks in the PDF($r$). We observe a broad O-U peak and a sharp O-O peak, consistent with Pa-3 phasing.

Could it also be a question of what length scales are probed with what time resolutions by the different measurement techniques? For total scattering at D4 with $\lambda = 0.5$ Å, the length scale is $\mathrm{FWHM}_{\mathrm{Vcoh}} \sim 60$ Å, and the time resolution is $\tau_{\mathrm{snapshot}} \sim \hbar / E_{\mathrm{o}} \sim 10^{-14}$ s.

# Continue if time permits . . .

# THE END

# Case of a polyatomic sample (several $Z$)

In a polyatomic system, the chemical affinities of $n$ different atomic species $Z_\alpha$ necessarily leads to a correlation at atomic sites $\mathbf{r}_i$ between the structural environment and the average scattering length $\overline{b}_\alpha$. This correlation prevents a proper definition of a dimensionless $S(q)$, but the scattered intensity can still be expressed as the sum of a distinct term (the interference function $F(q)$) and a total self-scattering term:

$$\frac{1}{N}\left[\frac{d\sigma}{d\Omega}(q)\right] = \sum_{\alpha,\beta}^{n} c_\alpha c_\beta \overline{b}_\alpha \overline{b}^*_\beta \left[S_{\alpha\beta}(q) - 1\right] + \sum_{\alpha}^{n} c_\alpha \overline{b^2}_\alpha \ ,$$

where $c_\alpha$ is the fraction or concentration of atomic species $Z_\alpha$, and the *partial* structure factor (PSF) $S_{\alpha\beta}(q)$ is the Fourier transform of the *partial* pair-distribution function (PPDF) $g_{\alpha\beta}(r)$, which is in turn proportional to the probability of finding an atom of type $Z_\beta$ at a distance $r$ from an atom of type $Z_\alpha$ taken as the origin:

$$g_{\alpha\beta}(r) - 1 = \frac{1}{2\pi^2 r \rho_o} \int_0^\infty q \left[S_{\alpha\beta}(q) - 1\right] \sin(qr)\, dq \ .$$

# Neutron Diffraction with Isotope Substitution (NDIS)

The technique of Neutron Diffraction with Isotopic Substitution (NDIS) is a powerful method for determining PSFs. It takes advantage of the distribution in isotopes of one or several elements $Z_\alpha$ in the sample, in order to modify $\overline{b}_\alpha$. One must therefore prepare several samples that are chemically identical but of different isotopic distribution. Each sample will give a different diffractogramme $d\sigma/d\Omega$.

Subtraction of two such diffractogrammes cancels the contributions of certain atomic pairs in the sample, yielding thereby a “first-difference function” whose Fourier transform contains information on the local environment of the isotopically substituted species only.

For a binary system ($n = 2$) there are 3 partial structure factors: $S_{11}$, $S_{22}$ et $S_{12} = S_{21}$, and therefore 3 NDIS samples are sufficient for a complete PSF determination, *e.g.* using a $3 \times 3$ matrix of scattering lengths and concentrations that links the 3 NDIS total diffraction patterns to the 3 PSFs.

For more information on NDIS techniques, see *e.g.* the review paper: *H.E. Fischer,* et al*, Rep. Prog. Phys.* **69** *(2006) 233–299.*

# NDIS example: First-difference function

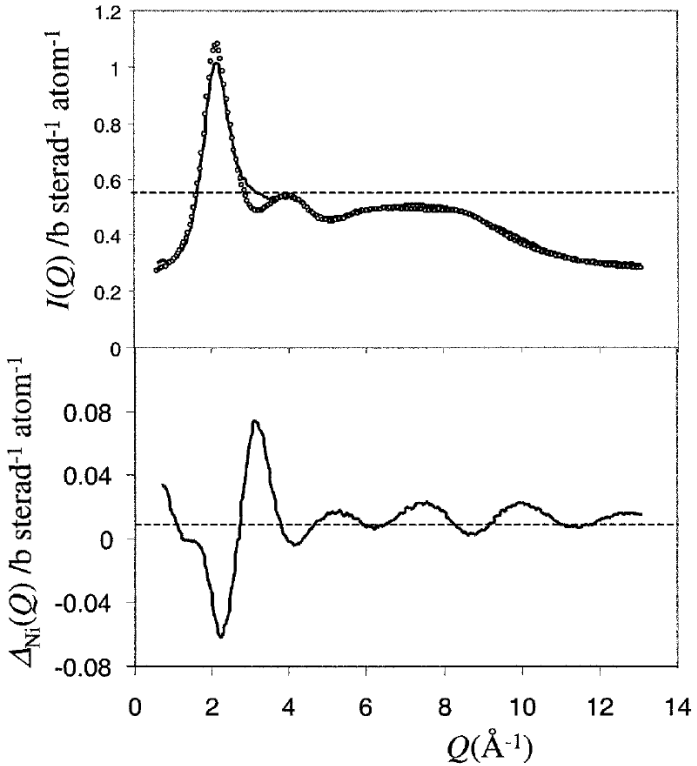


Total structure factors (top) for $D_2O$ solutions of $^{62}NiCl_2$ versus $^{nat}NiCl_2$. Subtraction (bottom) gives a "first-difference" $\Delta_{Ni}(q)$ retaining only those partial structure factors for atomic pairs including a Ni atom.

# NDIS example: First-difference function

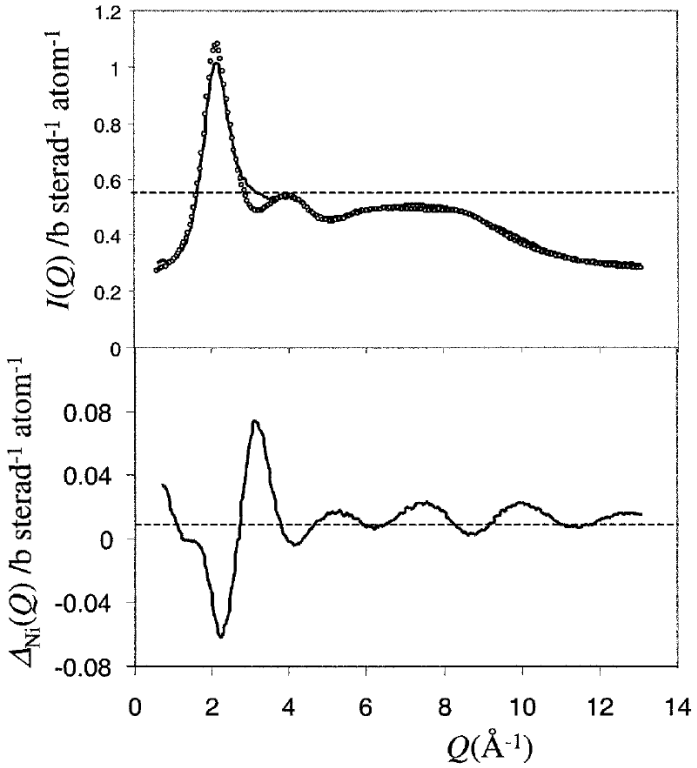


Total structure factors (top) for $D_2O$ solutions of $^{62}NiCl_2$ versus $^{nat}NiCl_2$. Subtraction (bottom) gives a "first-difference" $\Delta_{Ni}(q)$ retaining only those partial structure factors for atomic pairs including a Ni atom.

*(D.H. Powell, JDN11 proceedings)*

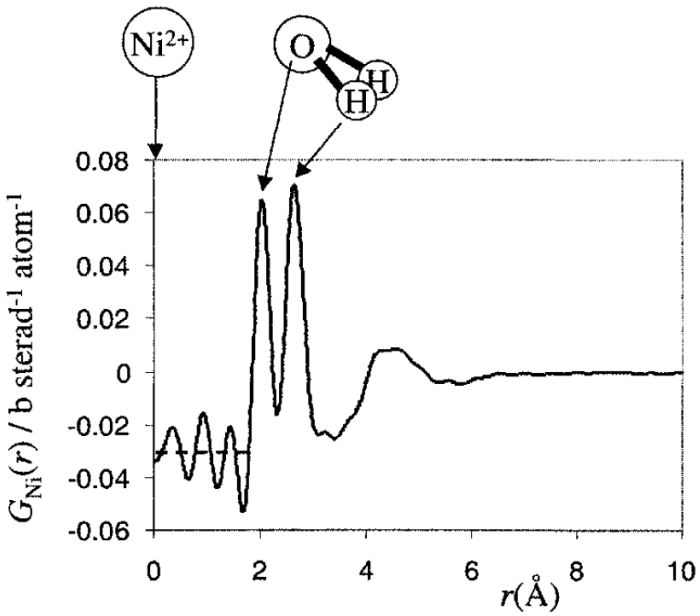


Fourier transformation leads to a first-difference pair-distribution function $G_{Ni}(r)$ showing the distribution of atoms with respect to a Ni atom at the origin. Assuming identical atomic environments for $^{62}Ni$ and $^{nat}Ni$, NDIS thus reveals this local structure.

# NDIS example: Complete PSF determination

molten $Ag_2Se$ (ILL) : < *Barnes et al., J. Phys. Condens. Matter 9 (1997) 6195* >

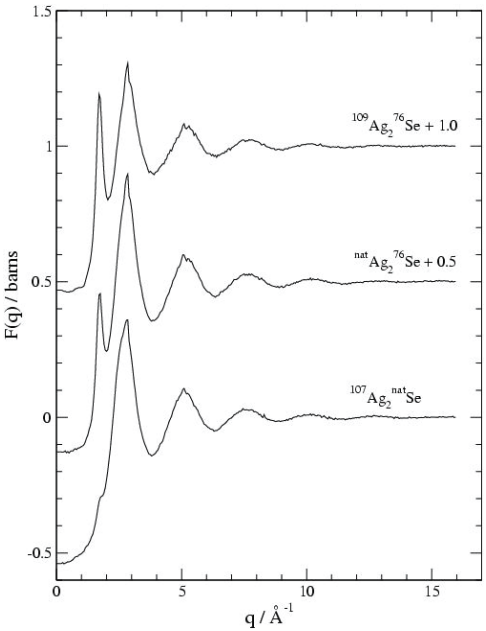


3 dσ/dΩ

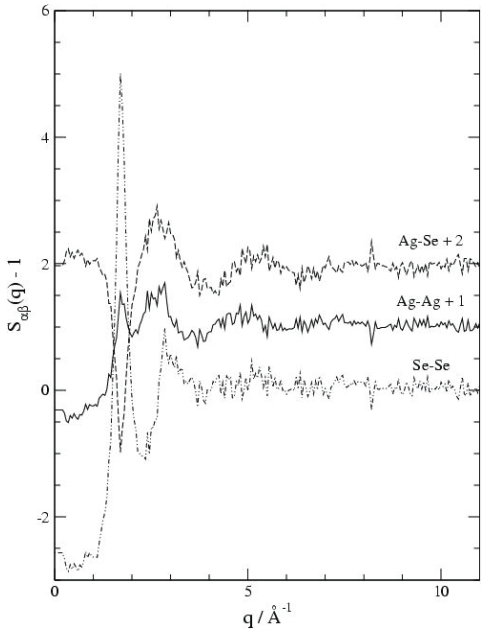


3 partial S(q)'s

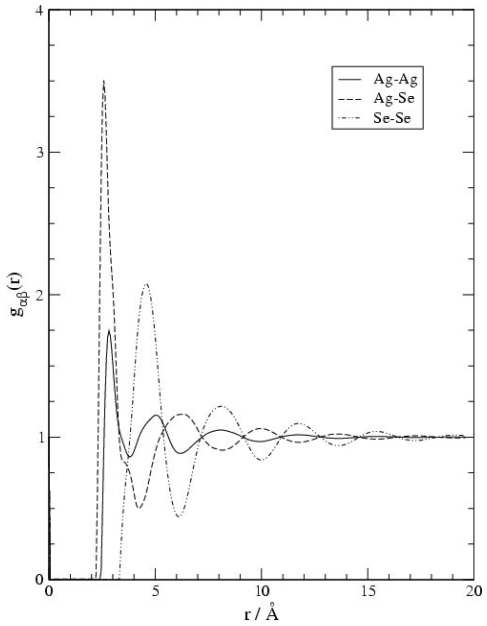


3 partial g(r)'s

The anti-phase correlations in the partial $g_{\alpha\beta}(r)$ extend to large $r$, indicating a relatively strong charge ordering consistent with maintaining electroneutrality in this ionic binary liquid, whose local structure is found to resemble that of the high-temperature crystal phase.

# Scattering lengths for x-rays versus neutrons

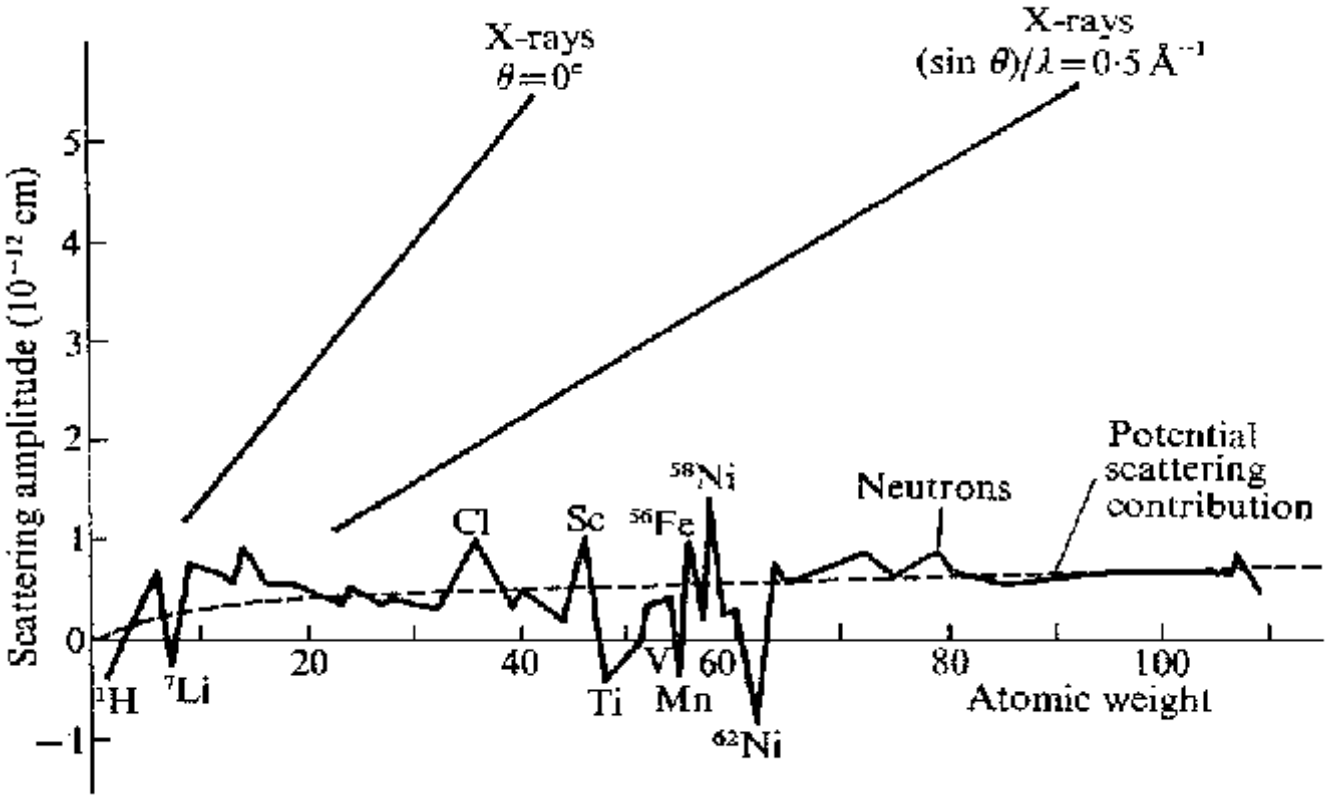


Although coincidentally of comparable magnitude, the scattering lengths (or "amplitudes") for x-rays $b_X$ and neutrons $b_N$ exhibit contrasting dependencies on atomic mass. Whereas $b_X$ increases linearly with the number of electrons (*i.e.* the atomic number), $b_N$ shows much variation not only between elements but also between isotopes of the same element (whence the NDIS technique).

# Scattering length contrast from XRD vs NRD

The difference in scattering lengths between x-rays and neutrons leads naturally to different Bragg peak intensities for a given sample, which can help to index the peaks and refine the crystal structure:

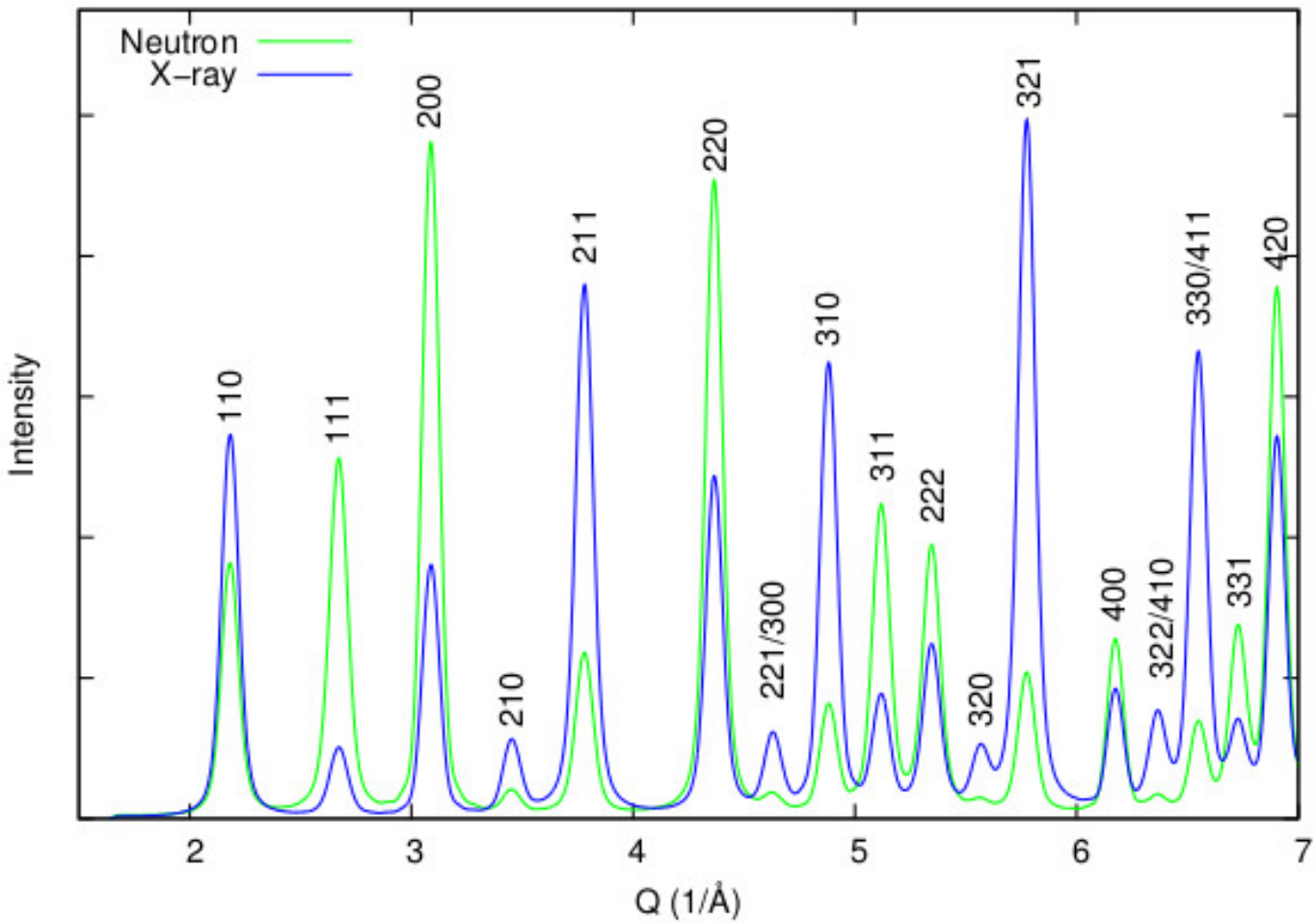

# Anomalous X-ray Diffraction (AXD)

The atomic scattering length for x-ray diffraction is independent of isotope but dependent on $q$ and on the incident energy $E_o$ :

$$b_X(q, E_o) = r_e f(q, E_o) = r_e \left[ Z f_{\text{falloff}}(q) + f'(E_o) + i f''(E_o) \right]$$

where $r_e = 2.818$ fm is the classical radius of the electron, and $f_{\text{falloff}}(q)$ is the modulation of the atomic form factor $f(q, E_o)$. The technique of Anomalous X-ray Diffraction (AXD) varies $E_o$ (*e.g.* at a synchrotron) and thereby adjusts the real ($f'$, left) and imaginary ($f''$, right) parts of the scattering length, especially near an absorption edge (here for Se):

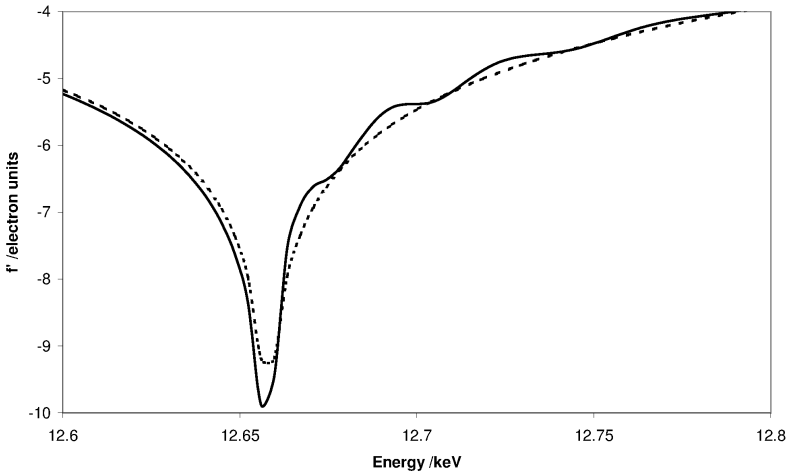


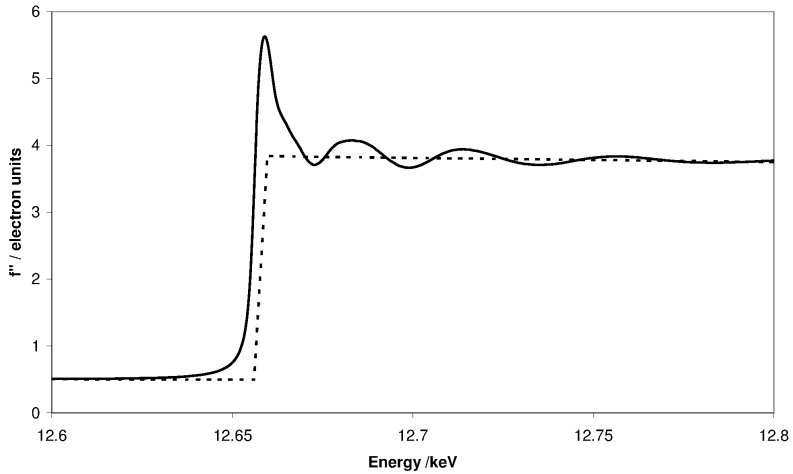


AXD is therefore analogous to NDIS.

# Advantages and Disadvantages of XRD versus ND

Neutrons scatter from the point-like nuclei rather than electron clouds, so that $b_N$ is essentially $q$-independent and thus the $r$-space resolution for ND can be better than for XRD. On the other hand, synchrotron x-ray beams are much more collimated than neutron beams, so that $q$-space resolution and thus $r$-range is generally better for XRD than for ND.

The static approximation is easily satisfied for XRD since x-ray incident energies are tens of keV rather than $< 1$ eV for ND, making inelastic scattering corrections necessary for the latter. By contrast, Compton scattering and fluorescence background must be subtracted for XRD.

The generally higher scattering lengths and higher absorptions for x-rays make difficult the use of complex sample environments, but can be useful if only the near-surface structure of a sample is to be probed.

AXD requires no expensive isotopes, and all the diffractogrammes are obtained on one sample in one environment in contrast to NDIS, but AXD is subject to uncertainties in the value of $f'(E_o)$ as well as to Resonant-Raman background when very close to an absorption edge.

Neutrons also scatter well from atomic magnetic moments and are more sensitive to low-$Z$ materials in the sample, as compared to x-rays.

# Schematic of the D4c neutron diffractometer (ILL)

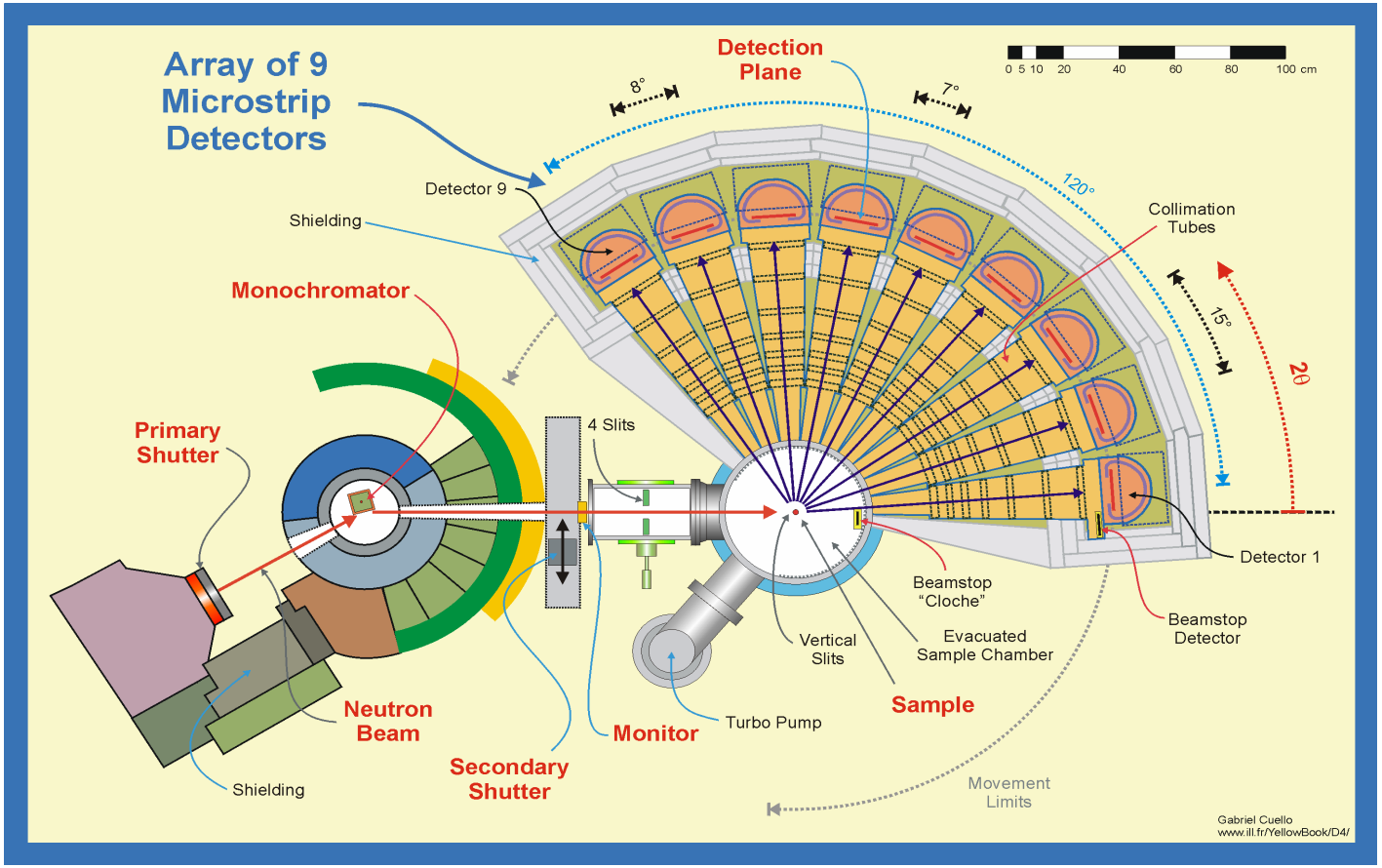


Hot source: $0.3 < \lambda/\text{Å} < 1.05$, standard $\lambda = 0.5$ Å for $q_{\max} = 23.5$ Å$^{-1}$

Counting rate: 1,000,000 (*i.e.* 0.1 % stats) per 0.125° in 3 hours.

Overall detector stability: $\sigma = \pm 1 \times 10^{-4}$ over 3 days.

Low background sans parasitic peaks for all $\lambda$ (0.5, 0.7 and 0.35 Å).

$\Rightarrow$ Champion of low-contrast ($\Delta b < 0.5$ fm) isotopic substitution expts.

# D4c commissioning in May/June 2000

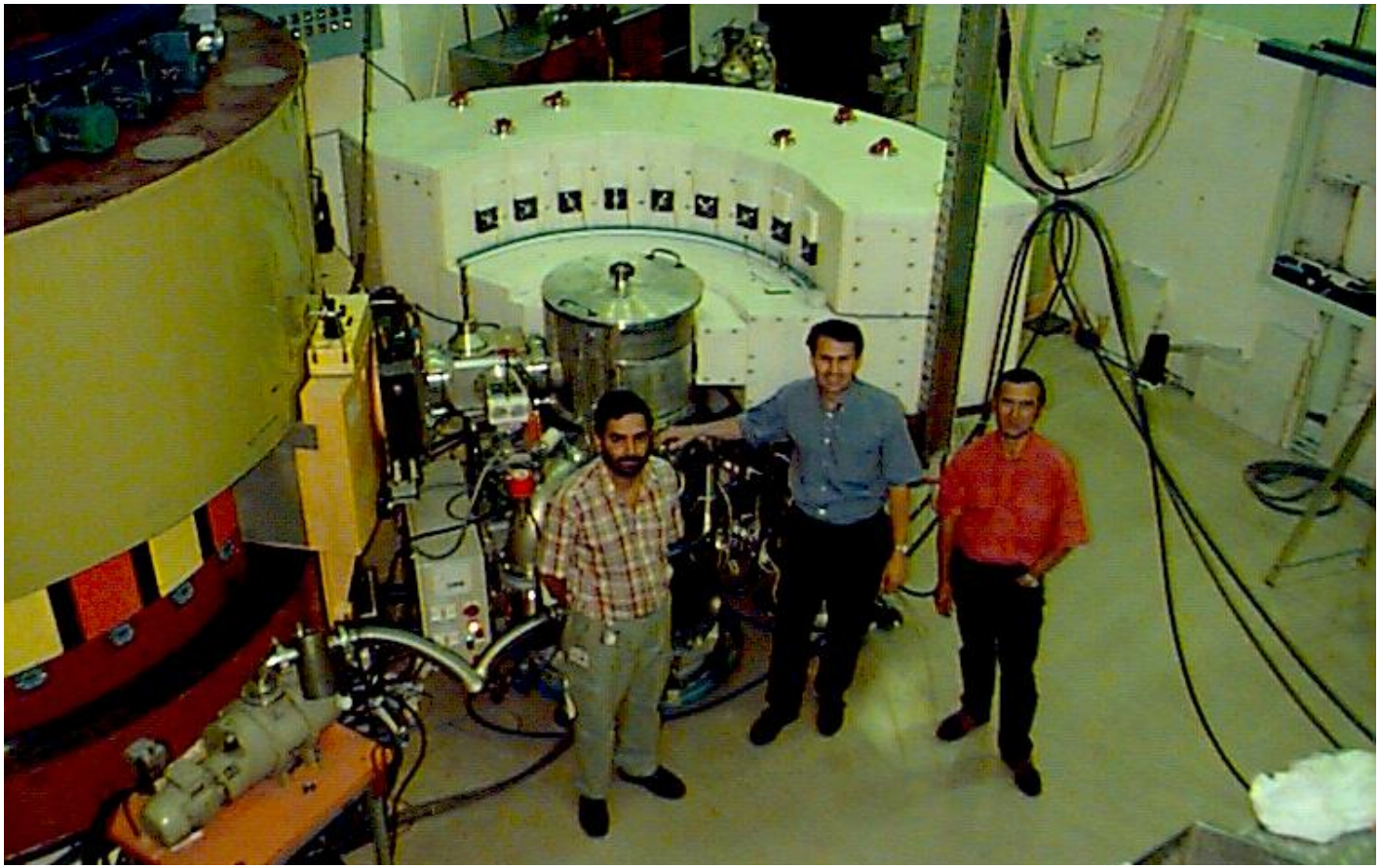

Big belljar for all sample environments (cryostat, furnace, special).

q-resolution: $\Delta q/q \lesssim 0.025$ for $2\theta > 15^\circ \Rightarrow \mathrm{FWHM}_r \approx 60$ Å.

r-resolution: for $\lambda = 0.5$ Å, $\Delta r = 3.79/(q_{\max} = 23.5\ \text{Å}^{-1}) = 0.16$ Å.

$\Rightarrow$ Increasing use for PDF-analysis (FT of powder diffraction pattern).

*H.E. Fischer,* et al*, Appl. Phys. A* **74** *(2002) S160–S162.*

# Two problems for deconvolving diffraction data

Now take another look at the formula for convolution:

$$f(q) \otimes g(q) = (f \otimes g)(q) = \int_{-\infty}^{\infty} f(q')\, g(q - q')\, dq'$$

$\Rightarrow$ there are two problems in applying the convolution theorem

$$g(q) = \mathrm{FT}[\, \mathrm{FT}(I(q)) \,/\, \mathrm{FT}(f(q))\, ]$$

to real diffraction data:

*First problem:* We need data of infinite $q$-range for $g(q)$ and hence for the measured $I(q)$, as well as an infinite $q$-range for perfect knowledge of the resolution function $f(q)$. None of this is possible in practice.

*Second problem:* The resolution function shape or profile $f(q')$ must be independent of the argument $q$ of $g(q - q')$. In other words, the resolution function should have the same shape at all $q = (4\pi/\lambda)\, \sin(\theta)$, where $2\theta$ is the diffraction angle. We will see from Caglioti that the resolution function FWHM depends strongly on $2\theta$.

# General case for deconvolution of diffraction data

Although a detector of 2-D sensitivity permits following or "straightening" of the Debye-Scherrer rings, this only corrects (partially) for the umbrella effect, and not for other resolution effects coming from sample size, incident beam dispersion and detector resolution.

In addition, diffraction data for liquids and glasses cannot be Rietveld-refined since there is no spatial periodicity, and also since the diffraction peaks are of intrinsic width and hence not resolution-limited.

Finally, no FT deconvolution tricks (*e.g.* convolution theorem) are possible because the resolution depends on the diffraction angle $2\theta$.

In the general case then, the measured (1D) intensity $I(2\theta)$ for a neutron or x-ray diffractometer can be written as the convolution of the true intensity $S(2\theta)$ with the instrumental resolution function $\mathcal{R}$:

$$I(2\theta) = \int \mathcal{R}(\rho, 2\theta)\, S(2\theta - \rho)\, d\rho$$

where $\rho$ is the (dummy) integration variable and the $2\theta$-dependence of $\mathcal{R}$ has been indicated explicitly.

# The Moments Method for general deconvolution

*Astuce*: When the measured diffraction intensity is relatively slowly varying over the width of the resolution function (generally the case for liquids/glasses diffraction), one can try making a Taylor's expansion of $S(2\theta - \rho)$ in $\rho$ around $2\theta$, and then to integrate separately each term of the series, which leads to calculation of the *moments of* $\mathcal{R}(\rho, 2\theta)$:

$$\mathrm{M}_n(2\theta) = \frac{1}{n!} \int_{-180^\circ}^{180^\circ} (-\rho)^n \, \mathcal{R}(\rho, 2\theta) \, \mathrm{d}\rho$$

that can be normalised as (in principle $\mathrm{M}_0 = const$):

$$\mathrm{A}_n \stackrel{\mathrm{def}}{=} \mathrm{M}_n / \mathrm{M}_0 \qquad \text{and} \qquad J(2\theta) \stackrel{\mathrm{def}}{=} I(2\theta) / \mathrm{M}_0$$

where the notation emphasizes the $2\theta$ dependence of the data $I(2\theta)$ which should be stronger than that of the moments $\mathrm{M}_n$.

$\Rightarrow$ The moments of the resolution function are in fact sufficient for deconvolving the data within the range of convergence of the Taylor's expansion, leading to the "Moments Method" for general deconvolution: *W.S. Howells, Nucl. Instrum. Meth. Phys. Res.* **219** *(1984) 543–552*.

# Calculating and applying the correction coefficients

As compared to diffraction data, the normalised moments $A_n$ are slowly varying functions of $2\theta$ except at very low $2\theta$ where the umbrella effect becomes severe. Ignoring thus the derivatives of $A_n(2\theta)$ w.r.t. $2\theta$ and considering only the first 4 derivatives of $J(2\theta) = I(2\theta)/M_n$ w.r.t. $2\theta$, we can derive for the true (*i.e.* deconvolved) diffraction intensity:

$$S(2\theta) = J + c_1 J' + c_2 J'' + c_3 J''' + c_4 J''''$$

where the correction coefficients $c_n(2\theta)$ are given by:

$$c_1 = -A_1 \qquad c_2 = -A_2 + A_1^2 \qquad c_3 = -A_3 + 2A_1A_2 - A_1^3$$

$$c_4 = -A_4 + 2A_1A_3 + A_2^2 - 3A_1^2A_2 + A_1^4$$

and for brevity the $2\theta$-dependences are not shown explicity.

$\Rightarrow$ Thanks to a fruitful collaboration with Spencer Howells (ISIS) and Phil Salmon (Univ. Bath), the **Decon** program has been developed and used to deconvolve diffraction data from the D4c instrument, *e.g.* for liquid Li (Salmon, *et al*, JPCM **16** (2004) 195) and for liquid and glassy $ZnCl_2$ (Zeidler, *et al*, PRB **82** (2010) 104208).

# Extension of D4c's coherence volume

$\Rightarrow$ Effect on *r*-range: $r_{max} = (5.55/2)/\Delta q$

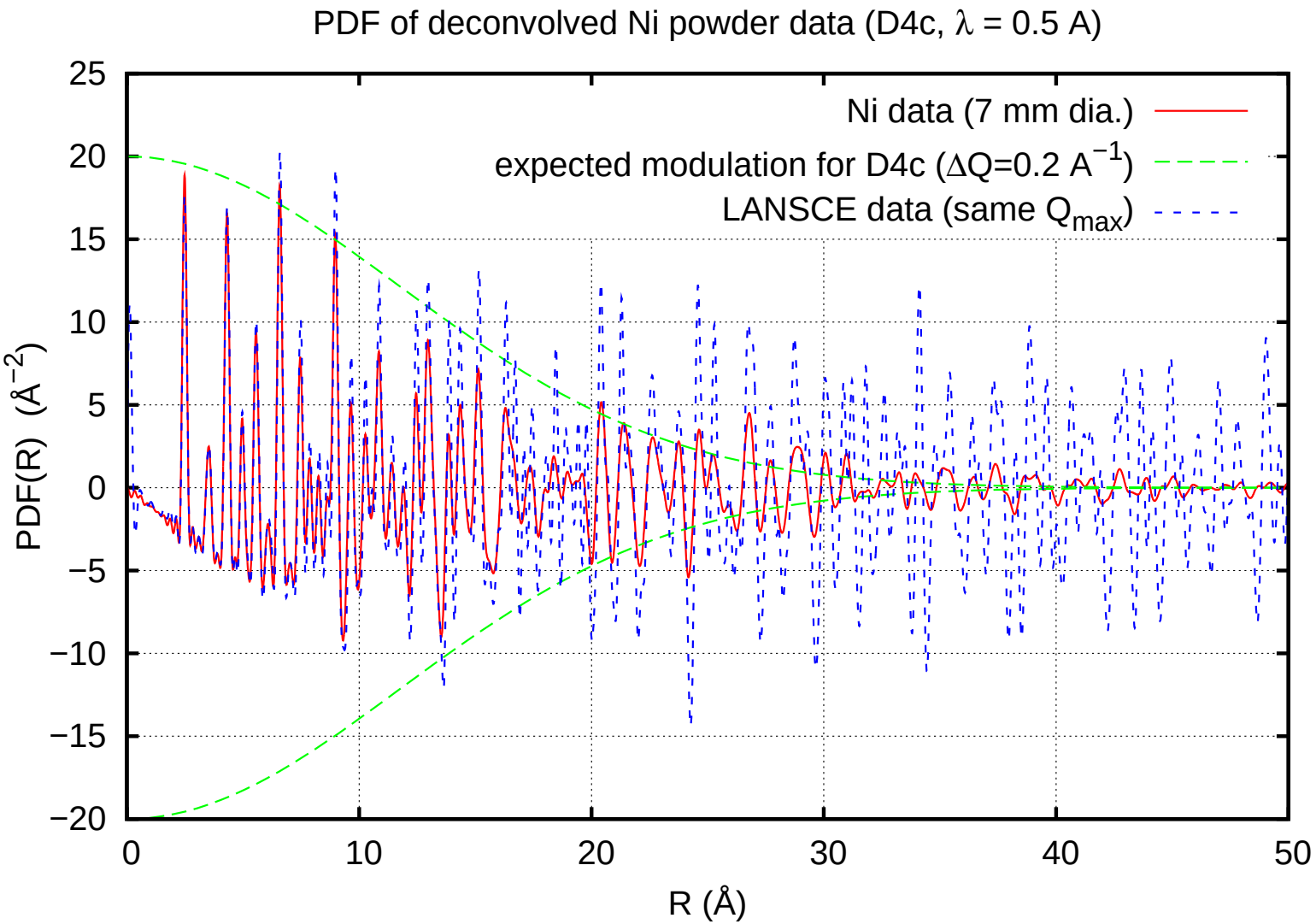

# Extension of D4c's coherence volume

$\Rightarrow$ Effect on *r*-range: $r_{max} = (5.55/2)/\Delta q$

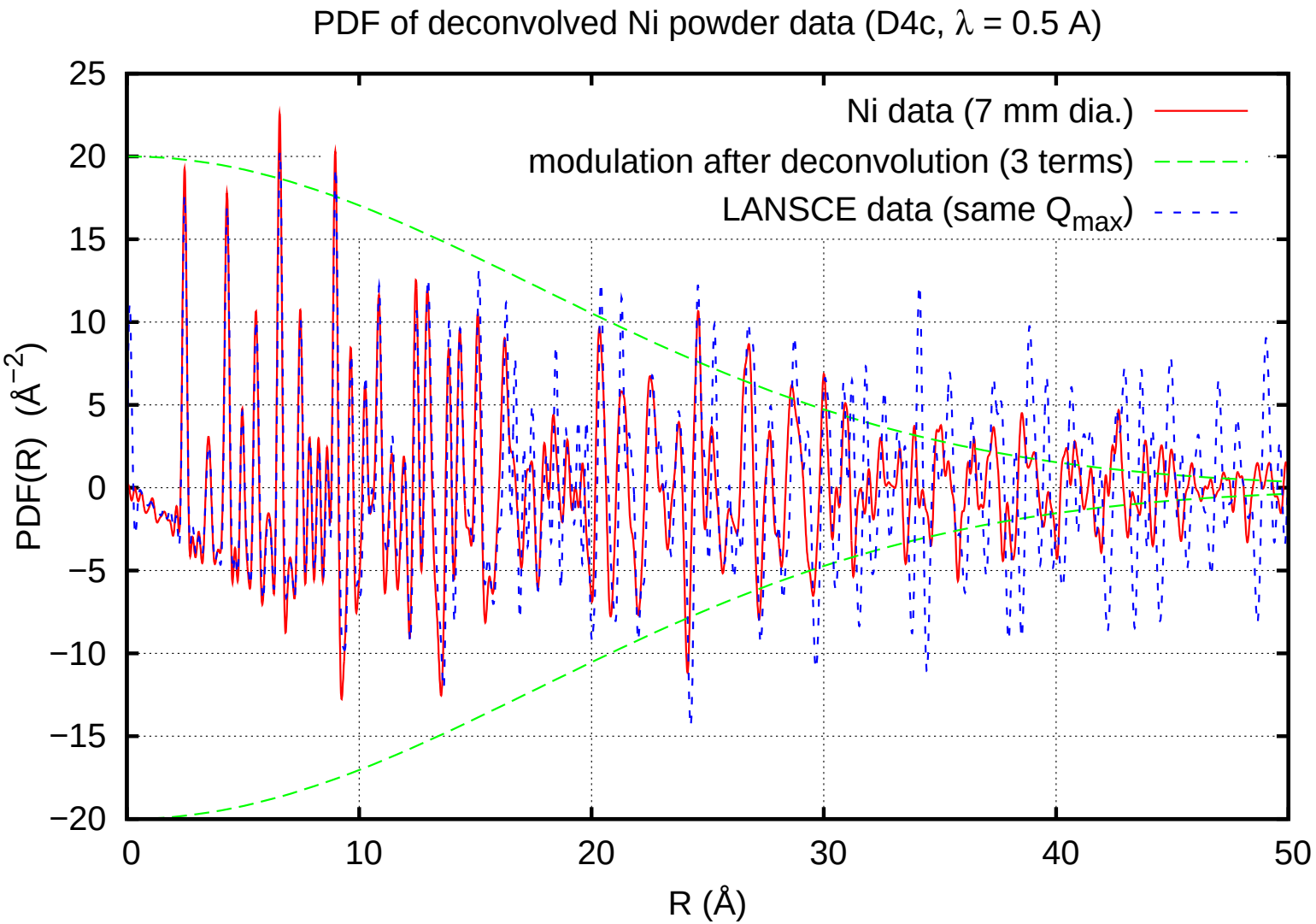

# Table of Contents